Dissertation zur Erlangung des Doktorgrades der Mathematisch-Naturwissenschaftlichen Fakultät, Universität Augsburg, Germany

Electronic correlations in $SrFe_{2-x}Co_xAs_2$ pnictides and EuB_6 probed by infrared spectroscopy under high–pressure and low–temperatures

Vorgelegt von Abid Karim

März, 2014

Erstgutachter: Prof. Dr. C. A. Kuntscher

Zweitgutachter: Prof. Dr. A. Loidl

Tag der mündlichen Prüfung: 17. Juli 2014

TABLE OF CONTENTS

1. Introduction

The discovery of the zero–resistance state (superconductivity) in mercury at 4.7 K in 1911 was one of the most fascinating phenomena of 20th century [18] which preceded the discovery of zero–friction (superfluidity of the helium) in 1937 by Pyotr Kapitsa and John F. Allen [15].

In fact, the zero–resistance state was limited to very low temperatures until the discovery of superconductivity in La–Ba–Cu–O compound at 30 K in 1986 [184], which opened up an area for new class of materials called high–temperature superconductors (HTSC). Later on, various compounds were synthesized with CuO–planes as a major constituent and they were classified as cuprates. The superconducting temperature T_c was successfully raised up to 135 K in mercury based cuprates (Hg–Ba_2–Ca_2–Cu_3–O_8), where T_c can be further increased up to 164 K by application of high pressure [14 - 16].

These high–temperature superconductors belong to the field of so called strongly correlated materials, which show unusual properties: metal–to–insulator transitions, half metallicity, high–temperature superconductivity, spin and charge density waves (SDW and CDW). Density function theory alone cannot explain the behaviour of these materials due to the effects of electronic interactions or correlations which were not taken into account during formulation of the band theory [17]. These unusual effects can be observed in many transition–metal oxides due to the peculiarities related to *d* or *f* orbital character of electrons. For example, NiO and CuO are expected to be good metals but they appear as wide band gap insulators due to the large onsite coulomb repulsion which dominates over the kinetic energy of electrons and creates an insulating gap. Thus, the behaviour of a given electron in these materials cannot be described independently of other electrons [13 - 15].

The recent discovery of high–temperature superconductivity in iron pnictides surprised the scientific community and offered a new class of superconducting materials, which had a magnetic element (iron) as a major constituent. Even though their superconducting temperatures are low, they are considered an important material in order to understand the problem of the mechanism of high–temperature superconductivity [22, 23, 26]

The word “Pnictogen” (or Pnicogen) is derived from the Greek word, “pnigein”, which means, to smother, block or restrain. The elements of the Group 15 are called Nitrogen or Pnictogen group. The name was given because of the inherit property of nitrogen. Each element of the group contains five electrons in their valance shell, and can form stable compounds, with double and triple bonds. The binary compounds containing this group can be referred as Pnictides [22, 23, 25].

There are three most famous phases, which are classified on the basis of their empirical formula, i.e. (1111), (122) and (111). The parent compound of the (1111) class is L_nFeAsO where L_n is lanthanide element. The AFe$_2$As$_2$ systems form the (122)–family of compound where A can be Ca, Sr or Ba, while LiFeAs or NaFeAs are example of (111)–phase [23, 25, 26].

In the first part of this research project, the (122)–phase SrFe$_{2-x}$Co$_x$As$_2$ pnictides at the doping concentration x = 0 and 0.1 were investigated by infrared spectroscopy under high–pressure and low–temperatures. It will enable us to observe closely and investigate effectively the electronic properties of SrFe$_{2-x}$Co$_x$As$_2$ pnictides under extreme conditions. Particularly, interesting are the effects caused by the temperature which leads to the substantial changes in the electrodynamics of the system. This is obviously manifested in the transition to the low–temperature spin density wave state which can be cleared by the evolution of infrared spectral weight as a function of pressure and temperatures [29, 30, 89, 93].

At room temperature, the undoped SrFe$_2$As$_2$ is paramagnetic with a tetragonal crystal symmetry and transforms to an antiferromagnetic spin density wave state with an orthorhombic symmetry below 200 K [136, 137]. The parent compound is not superconducting but the application of high–pressure or chemical doping suppresses the SDW state which leads to the emergence of a superconducting state. Both electron and hole doping suppress the phase transitions in a similar way and induce a superconducting state [89, 93].

The effect of these phase transitions are observed as a drastic increase in electrical conductivity in the transport measurements [29, 30]. In optical measurements, the spin density wave state appears as a strong suppression of reflectivity in the far and mid infrared frequency range, while the superconducting gap lies below the frequency limit of the pressure setup. Therefore, one of the main goal of this research project is to study the infrared properties of the parent SrFe$_2$As$_2$ and cobalt doped SrCo$_{1.9}$Fe$_{0.1}$As$_2$ pnictides in the spin

density wave state under high–pressure (0–6 GPa) and various temperatures from 300 K down to 10 K [135].

Metal hexaborides:

Metal hexaborides (MB_6) have gained the interest of scientific and technical communities because of the simple chemical structure but it shows exotic physical properties due to strong correlation among the conduction electrons. MB_6, where M stands for a metal, are synthesized with various alkaline earth (*AE*) and rare earth (*RE*) metals and their physical properties change when synthesized with different metals [46, 47, 55, 56].

For example, LaB_6 shows superconductivity at low temperatures while it is a simple metal at room temperature. In addition, it has a low work function which is considered a technological advantage for designing coherent electron sources [41]. On the other hand, at low temperature SmB_6 shows an energy gap in the electronic excitation which appears as a substantial drop in the electrical conductivity in transport measurements [42, 55, 56].

In rare earth hexaborides, the *f o*rbital character of the electrons has a major importance in their electronic and magnetic properties. However, the discovery of ferromagnetism in the lightly doped SmB_6 and CaB_6 surprised the scientific community, where the ferromagnetism occurred for a very low doping concentration of La, and with high Curie temperatures. This can be one of the major technological applications of the semiconducting hexaborides: to manipulate their magnetic properties for designing the future room temperature spintronic devices [46 - 48].

Synthesis of hexaborides with Eu gives an exciting magnetic and electronics properties which are challenging for the scientific community in order to explain the underlying physics. For example, the classification of EuB_6 as a semiconductor or a semimetal is problematic and has not yet been resolved. In addition, it shows a negative giant magnetoresistance (GMR) at liquid nitrogen temperatures [45, 55, 56].

In the second part of this research project, the infrared properties of EuB_6 were investigated under high–pressure and low–temperatures. The material shows transition from the paramagnetic to the ferromagnetic phase via two consecutive phases at 15.2 K and 12.2 K which is observed as a huge shift in the plasma edge towards higher frequencies in the mid infrared range [52, 55, 56, 80].

The physical properties can be tuned by doping or application of high pressure. For instance, carbon doping shifts the plasma edge towards higher frequencies with increasing metallicity. On the contrary, calcium doping shifts the plasma edge towards lower frequencies with decreasing metallicity. Theoretical calculations [81, 79] predicted a large shift of plasma edge towards higher frequencies with application of high pressure, both in paramagnetic and ferromagnetic states. Therefore, the second goal of this research project is to study the infrared properties of EuB_6 under high–pressure (0–8 GPa) at eight sets of temperature cycles from 300 K down to 5 K [52, 55, 56, 80].

The thesis is presented in several sections: a brief review of the experimental techniques is given in Chapter 2. The literature survey relating to $SrFe_{2-x}Co_xAs_2$ pnictides is presented in Chapter 3, along with results and discussion of $SrFe_2As_2$ and $SrCo_{1.9}Fe_{0.1}As_2$. In chapter 4, a brief literature survey about EuB_6 along with results and discussion is presented. The summary, conclusions and future perspectives are given in Chapter 5. In the appendix, a brief overview of the experimental details at ANKA synchrotron source is presented along with the graphs of EuB_6.

2. Experimental techniques

This chapter gives a brief overview of the experimental techniques which were used to obtain the optical data as a function of pressure and temperature.

2.1. Grating and Fourier transform spectrometers

The spectrometers are used to project and focus the light on the material's surface and the response (Reflectance or Transmittance) of the material is measured as a function of the constituent frequencies. Since the radiation comes out from different sources with certain spectral widths, they need to be separated or filtered. Dispersive elements like grating or prism are used to separate the light into its spectral constituents [10, 11].

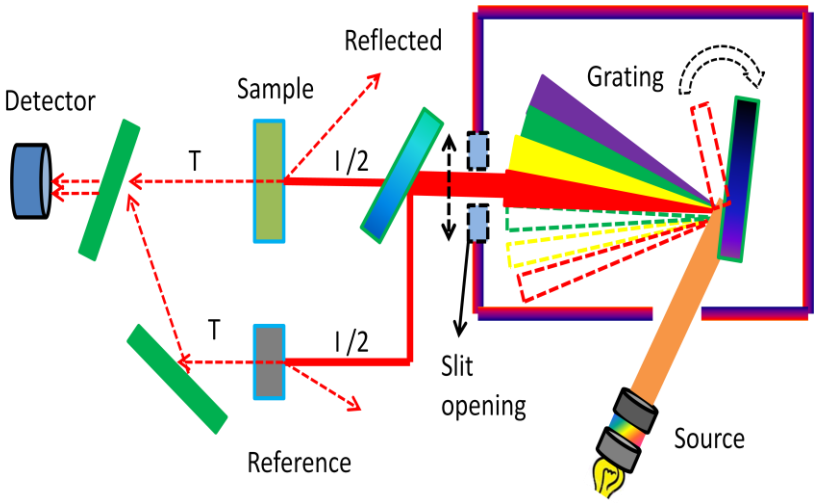

Figure 2.1. Schematic representation of grating type spectrometers. Redrawn from the concept of [9 - 12].

A typical grating type spectrometer is shown in Figure 2.1, where the radiation from the source is first dispersed into its spectral constituent by grating and then passed through the opening slit. The resulting intensity of the reflected or transmitted light is measured by a detector as a function of frequency.

The reference and sample can be interchanged for a single beam, or the beam can be split into two parts. The reference needs to be changed only if another type or family of material will be measured [7 - 10].

On the other hand, FTIR (Fourier Transform Infrared) spectrometer uses a Michelson interferometer instead of grating or prism as illustrated in Figure 2.2. The light from the source is divided into two beams with equal intensity ($I/2$) by a beam splitter. These beams are reflected back from a fixed and a movable mirror. They recombine and produce an interference pattern (bottom right of Figure 2.2) as a function of the position of the movable mirror. Thus, the Electric field E_D (x, t) reaching the detector can be written as follows [9, 10]:

$$\mathrm{E_0(x,t)} = \frac{1}{2}\left[\,\mathrm{E_0(k_0 - \omega t) + E_0\{k_0(x\ +\ 2\Delta x) -\ \omega t\}}\,\right] \qquad (2.1)$$

where, k_0 is a wave vector, x is the distance of a fixed mirror, Δx is a distance move by the movable mirror which creates a path difference of $2\Delta x$, ω is an angular frequency and t is the time.

By solving Eq. (2.1) for an intensity as a function of the Δx and substituting $k_0 = 4\pi v_0$, the following expression can be obtained [9, 10]:

$$\mathrm{I(x)} = \frac{\mathrm{I\,(\nu)}}{2}\left[\,1 + \cos(4\pi\nu_0 x)\,\right] \qquad (2.2)$$

where, $\mathrm{I\,(\nu)} = c_0 \varepsilon_0 E_0^2 / 2$, and it represents the intensity of an electric field at the detector as a function of the distance moved by the movable mirror.

When the movable mirror moves (Δx) by a quarter of wavelength ($\lambda/4$), it will create a path difference of $\lambda/2$ which will produce destructive interference. Another increment of Δx by $\lambda/4$ in will produce a phase difference of λ, which will cause constructive interference as shown in Figure 2.2. Destructive interference occurs when the path difference is an odd multiple (n) of the wavelength ($n + \lambda/2$). Constructive interference occurs when the path difference is an integral multiple of the wavelength ($n\lambda$) [9, 10].

If the spectrum contains a broad range of frequencies which are coherent in phase, Eq. (2.2) can be modified as follows:

$$I(x) = \int_0^{\infty} \frac{I(\nu)}{2} [\, 1 + \cos(4\pi\nu_0 x) \,] d\nu \qquad (2.3)$$

Further manipulations can yield the iterative form of the equation as follows:

$$I(x) = \frac{1}{2} \int_0^{\infty} I(\nu) d\nu + I'(x) \qquad (2.4)$$

where, *I´(x)* is an analogue signal which shows the integral sum of all intensities for the entire wavelength present in the spectrum as a function of a distance (*x*). This makes the equation simple and the values of an interferogram can be computed successively by applying numerical methods. *I(x)* represents an interferogram based on the previous values of the interferogram, i.e. *I´(x)* which is plotted as a function of the optical path length and shown in Figure 2.3 (a) [9, 10].

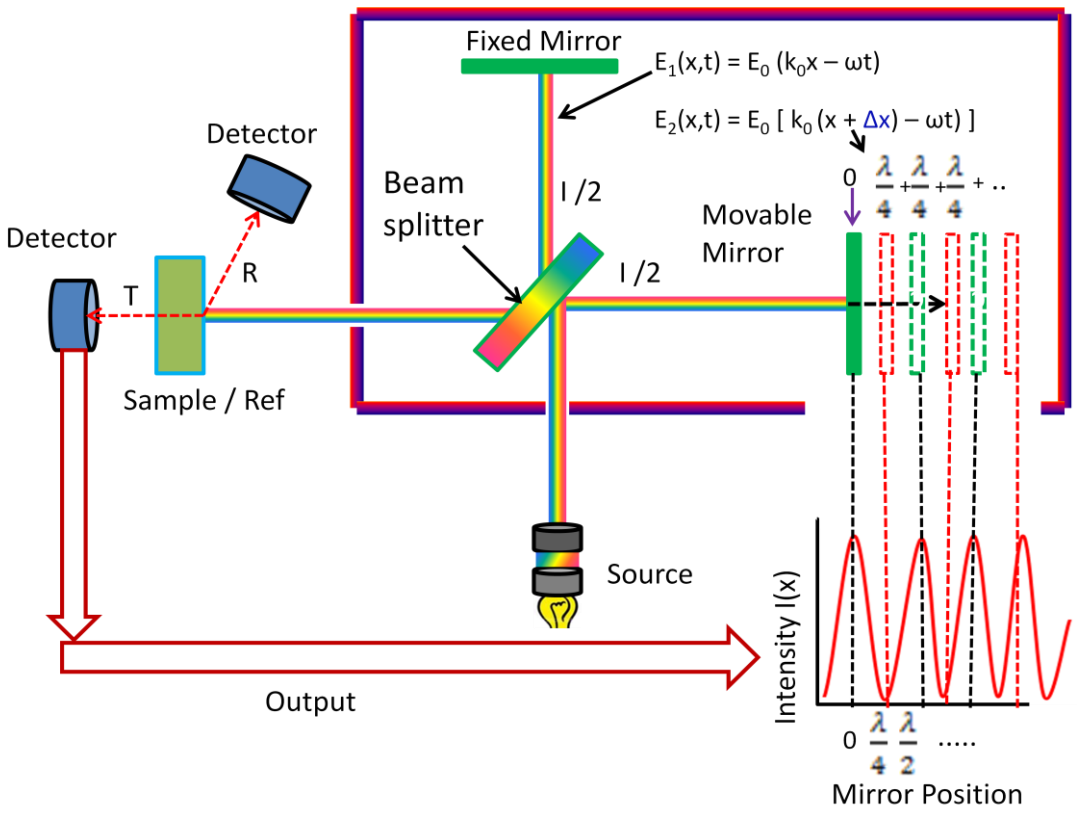

Figure 2.2. A schematic drawing of the FTIR spectrometer based on a Michelson's interferometer. Redrawn from the concept of [9 - 12].

In order to see the intensity of the corresponding wavelength in an interferogram *I(x)*, Fourier transformation of the interference pattern is required to obtain the frequency–domain spectra given as follows [9, 10]:

$$I(\nu) = \frac{1}{2}\int_0^{\infty} I(\nu)d\nu + I'(\nu) \qquad (2.5)$$

The graphical representation of the Fourier transformed signal is shown in Figure 2.3 (b) which shows a plot of the intensities as a function of constituent frequencies [9 - 11].

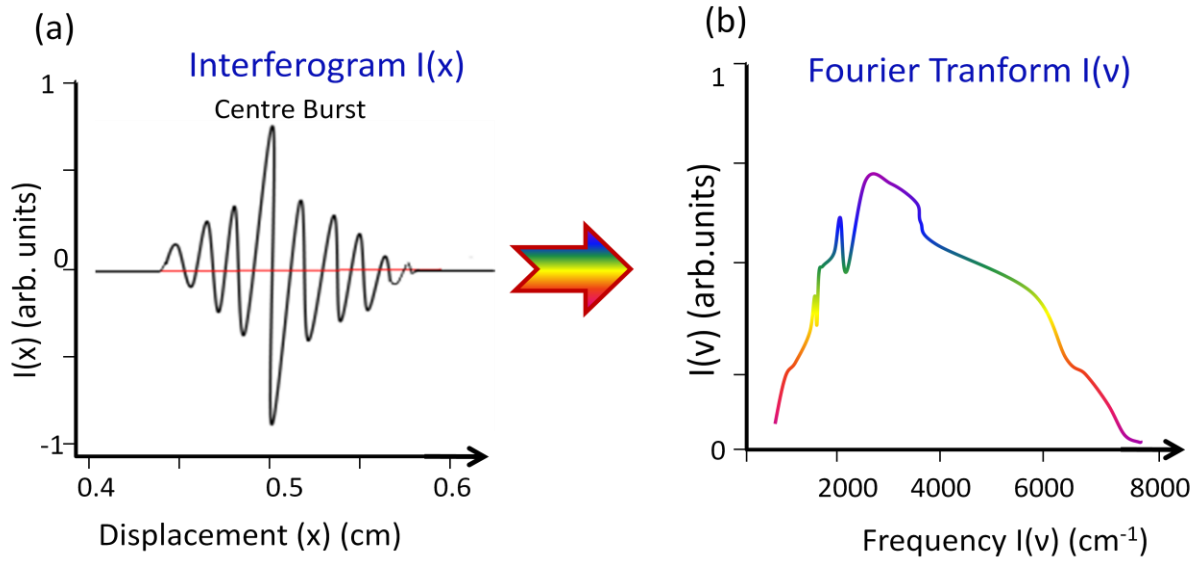

Figure 2.3. (a) Interferogram for polychromatic light shows the intensity plot as a function optical path length (x). (b) Fourier transformed spectrum showing the intensity (I) as a function of frequency (ν) [9 - 12].

Apodization:

The resolution ($\Delta\nu = 1 / \Delta x$) of FTIR spectrometer is the reciprocal of the maximum achievable path difference (Δx) of the movable mirror, i.e. for a scan distance of 4 cm, the resolution of an interferometer will be 1/4 = 0.25 cm^{-1}. A maximum resolution can be obtained for the infinitely large scan distances. Practically, the movable mirror can only move to the limiting distance which results in false side lobes in the transformed spectra [9 - 12].

The effect of these false side lobes can be minimized by multiplying the interferogram by a mathematical function called Apodization, which results in a decreased resolution and the

spectral features get broadened. Various kinds of the apodization function are in use, for example, triangle, Beer Norton or boxcar etc [9 - 12].

2.1.1. Advantages of FTIR spectrometer

The FTIR spectrometer has several advantages over the dispersive spectrometers; some of them will be discussed below [9 - 12].

Multiplex (Fellgett's advantage):

The technique is very fast and saves more experimental time compared to the dispersive spectrometers. For example, to measure a range from 800–8000 cm^{-1} with resolution two will need: [(8000 – 800) * 3600] / 2 = 60 minutes. If each step takes one second, i.e. moving grating (see Figure 2.1) then measuring the intensity will need at least thirty minutes for one complete scan. In contrast, FTIR spectrometer will take only one second for the same measurement range [9 - 12].

Throughput and resolution:

Normally, the slit size defines the resolution of the dispersive spectrometers (see Figure 2.1) which means narrowing the slit size will increase the resolution but the signal throughput will be decreased. Thus, the resolution will vary throughout the spectral range but with constant signal–to–noise ratio. On the other hand, FTIR spectrometers have higher throughput but with varying signal–to–noise ratio, while the resolution stays constant throughout the spectral range [9 - 12].

Precision and calibration:

In FTIR spectrometers, a laser beam is used to control the velocity and to measure an instantaneous position of the movable mirror. The laser beam is also used for the internal calibration due to its constant and stable wavelength, which gives the x–axis points with a highest degree of accuracy and precision [9 - 12].

2.2. Low temperature and high pressure instrumentation

2.2.1. The High Pressure instrumentation

Diamond anvil cells (DAC) are widely used in laboratory scale instrumentation, especially for the characterization of materials. A schematic drawing of a typical DAC is shown in Figure 2.4. The diamonds are cut to create flat or bevelled culets (10–15 degree) depending on the aimed pressure range. The two diamonds are mounted on the seats which transfer the pressure to the sample, enclosed in the gasket [6, 20].

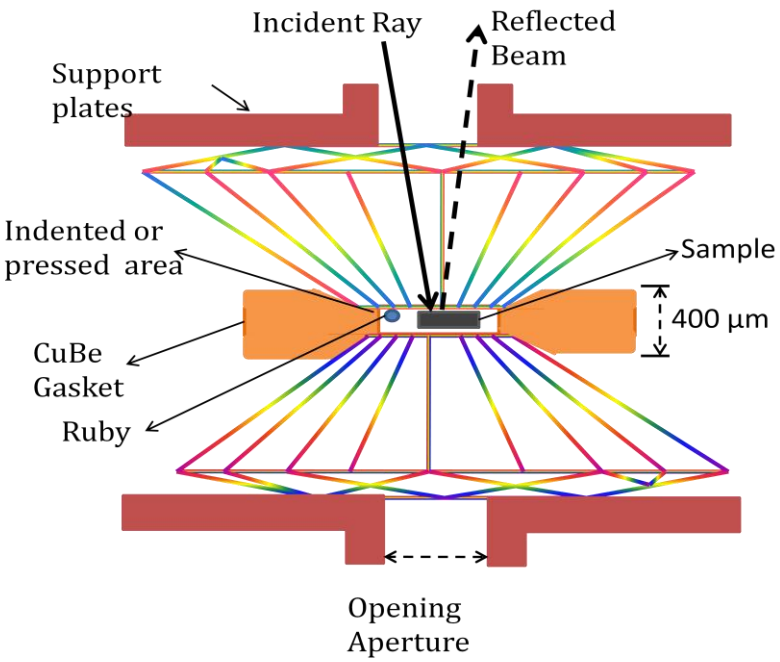

Figure 2.4. An illustration drawing of a typical Diamond Anvil Cell (DAC) adopted from the concept of reference - [6, 20].

The gaskets are the circular plates of CuBe alloy which are used to seal the mating surface between two diamonds as shown in Figure 2.4. The gasket needs to be indented by the DAC, and drilled with the hole of desired diameter [6, 20].

The hole is used as a sample compartment. The ruby is placed inside the sample compartment, for in–situ pressure measurements. The sample compartment is filled with a pressure transmitting medium for generating high–pressures as shown in Figure 2.4. Different kinds of pressure transmitting media are in use depending on the measurement conditions [6, 20].

Normally, the culet of the diamonds determines the maximum achievable pressure for the DAC. In general, the hole diameter needs to be around 1/3 of the culet size, which would prevent the breaking of diamonds. But exceptions can be made by adjusting the parameters, i.e. the thickness of the pressed area or the hole's diameter [6, 10, 69].

In low frequency measurements, such as far infrared, diamonds of larger size are required to avoid the diffraction limit. This ultimately increases the cost of the pressure equipment [6, 10, 69,].

Syassen–Holzapfel pressure cell:

The cross sectional view of a Syassen–Holzapfel clamped piston–cylinder cell is shown in Figure 2.5. The cell is made of hardened steel. The force is applied through the thread–knee mechanism, which is coupled with a gear box. The gear box helps to synchronously turn the two threaded rods, which moves the lower end point (knee) of the levers towards each other. This results in an exertion of uniform force at the piston surface. The piston is moved inside a long guided cylindrical assembly in order to keep the faces of the top and bottom diamonds exactly parallel to each other [20].

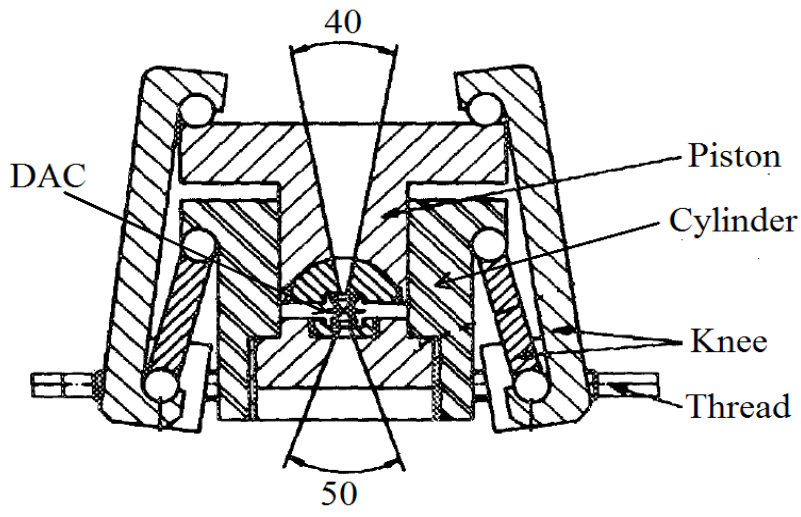

Figure 2.5. Cross–sectional drawing of a Syassen–Holzapfel cell taken from -[20]. The whole cell is built from a single material, i.e. hardened steel. Two threads–knee assemblies are used to apply a uniform force at four sides of the piston.

EasyLab pressure cell:

The schematic drawing of the easyLab pressure cell for the model "CryoDAC Mega" is shown in Figure 2.6. The cell is made of CuBe alloy (non–magnetic) in order to perform the experiments on magnetic materials. The diamonds are fitted with CuBe rings and tungsten–carbide support plates. The piston–cylinder assembly is placed and fixed inside the outer shells [69].

The four threaded–screws are used to apply a loading force on the piston, which generates pressure inside the DAC. The red headed screws need to be tightened in anti–clockwise, while black–headed screws should be tightened in a clockwise direction. The cell was used successfully for high pressure measurements at room temperature, while at low temperature pressure jumps occurred inside the DAC [69].

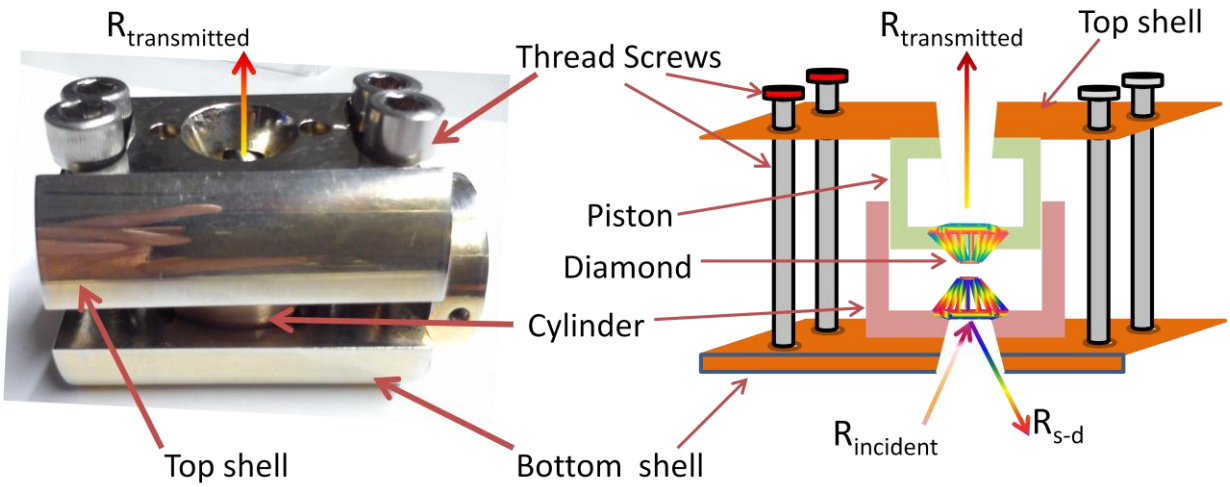

Figure 2.6. Snap shot (left) and an illustration drawing (right) of the model, "CryoDAC Mega" easyLab cell. The pressure generating force is applied through the four threaded screws (grey colour) which are mounted at the corners of the outer shell (orange colour) [69].

2.2.2. The Low Temperature instrumentation

The exchange gas cryostat of model, "CryoVac KONTI–Cryostat Spectro-A" was used in the experiments as illustrated in Figure 2.7. Liquid helium was used to reach low temperatures (~ 5 K) by manually controlling the helium flow rate. The sample holder is mounted at the bottom of the insert [70, 71].

The heat exchange occurred through the body of the pressure cell. Two temperature sensors *A* and *B* are mounted; one at the sample holder and another at the helium transfer line. The helium flow rate is needed to be controlled in a way that the difference in temperatures for sensors *A* and *B* should not exceed from 2 K. The helium valve was opened completely in order to achieve 5 K [70, 71].

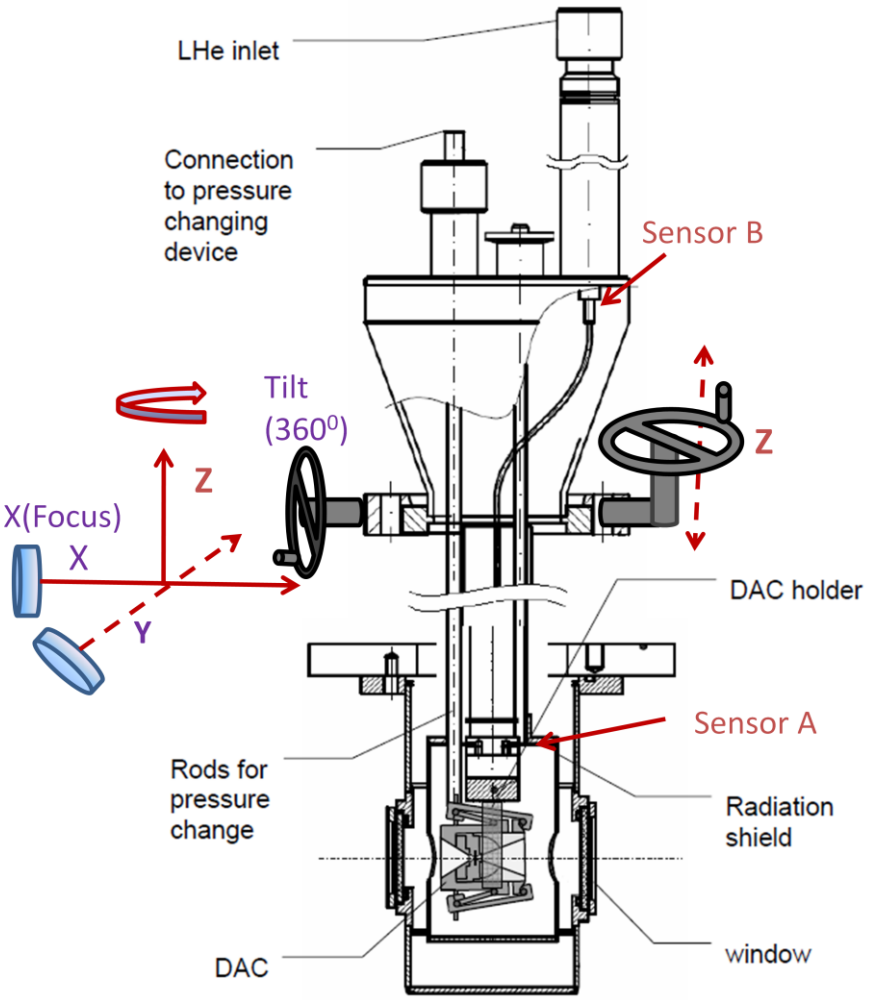

Figure 2.7. Helium exchange–gas cryostat of Model, Cryovac KONTI–cryostat Spectra–A, taken and modified from-[70]. The cryostat has four degrees of freedom, i.e. three axes (x, y, & z) and one tilt (360⁰) control.

The mounted Syassen–Holzapfel cell is shown in Figure 2.7 at the cryostat insert. The pressure can be controlled from outside the cryostat, through the coupling rods connected to the DAC's dial. However, for the easyLab cell, the pressure cannot be controlled from outside. To change the pressure, the cryostat needs to be warmed up to room temperature. The cryostat and the LTHP (low–temperature and high–pressure) setup are required to be at

ambient pressure, in order to change the pressure, which makes these measurements very time consuming [70, 71].

There are four degrees of freedom to move the sample, which is mounted at the cryostat insert. Along the *x*–axis (focus) the sample can be moved into the focal spot of the *IR*–beam, while the *y*–axis moves the DAC perpendicular to the *IR* beam as illustrated in Figure 2.7. Along the *z*–axis, the sample can be moved from 10 mm below to 40 mm above the optical axis. The tilt allows to rotate the sample around the *z*–axis [70, 71].

2.2.3. Low Temperature and High pressure (LTHP) setup

Since the working distance of the commercial spectrometers is not large enough to mount the pressure cell together with low temperature cryostat, an optical system (LTHP setup) was designed and developed with larger working distance by Dr. A. Pashkin under the supervision of Prof. C. A. Kuntscher [71].

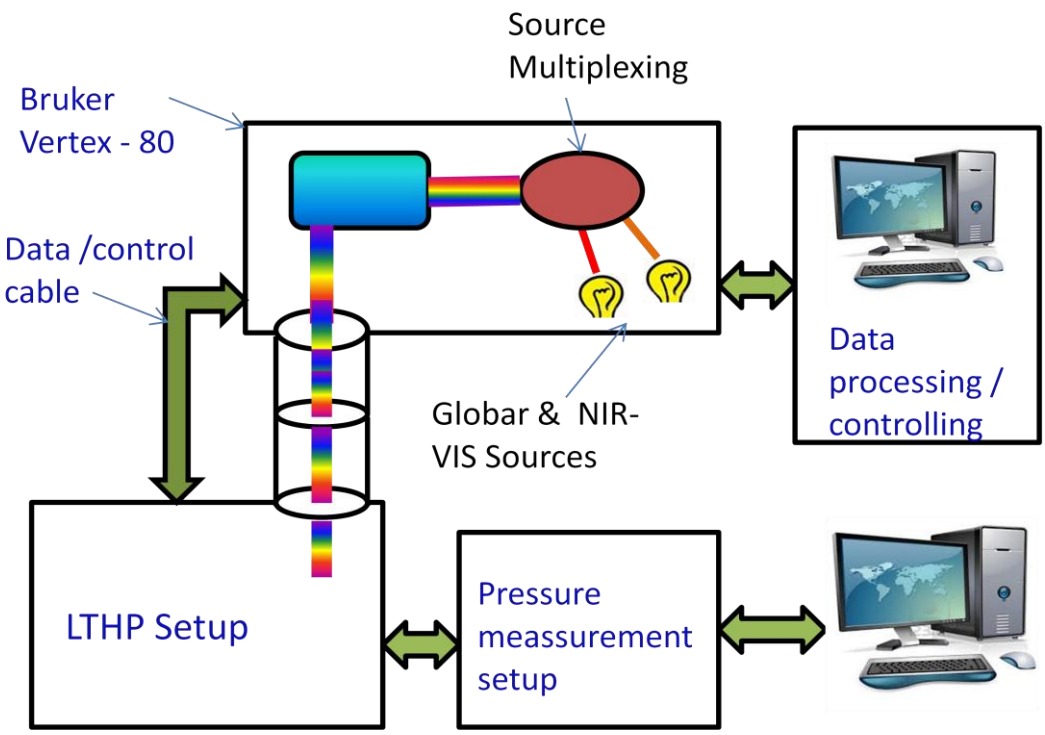

Figure 2.8. A schematic drawing of the instrumental setup for the low–temperature and high–pressure (LTHP) measurements. The double sided arrow shows the bidirectional data or control cables [10, 71 - 74].

The block diagram of the LTHP setup along with other interface machines is shown in Figure 2.8. The infrared beam from the spectrometer (Vertex–80) was directed inside the LTHP setup and focused on the sample via a Schwarzschild objective and condenser. The commercial software of Bruker Vertex–80 was used for data acquisition and aperture wheel controlling. The detectors were interfaced to the spectrometer through the available free I/O (input / output) ports in the electronic panel [7, 71 - 74].

The whole optical system of the LTHP setup was mounted on 20 mm thick aluminium plates with strong angular supports in between. The setup was designed in a way, that it can bear the weight of the cryostat under high vacuum. The H_2O and CO_2 absorption were eliminated by evacuating the setup to ~ 10^{-3} bars [71].

2.2.4. Pressure Measurement

The αAl_2O_3 doped with Cr^{3+} was used as a pressure sensor. Pure Al_2O_3 is colourless while replacing a small friction of Al^{3+} with Cr^{3+} induces a trigonal distortion (see Figure 2.10) in the crystal due to the larger ionic radius of Cr^{3+}. This substitution changes the symmetry of the sixfold coordination of the oxygen and Al^{3+} ions and forms an octahedral coordination of Cr^{3+} with the six O^{2-} ions. These changes in the crystal arrangement influence each Cr^{3+} ion, resulting in absorption of light in the yellow green region as shown in Figure 2.9. The yellow green light is reemitted as a red luminescence from Cr^{3+} which makes the ruby appear red in colour [12, 64, 65].

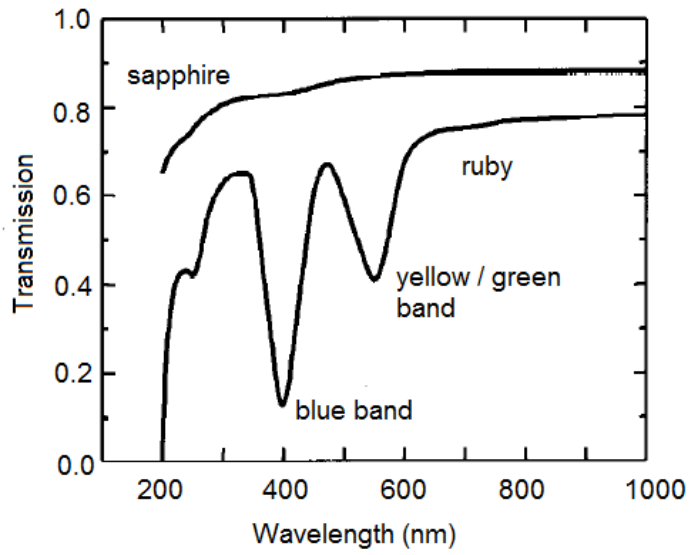

Figure 2.9. Transmission spectra for the pure Al_2O_3 (sapphire) and a doped Al_2O_3 (ruby) with 0.05 % Cr^{3+}. The figure is taken and modified from-[12].

When the Cr^{3+} ion is shined by a green or violent laser, the electrons are excited from $^4A_2$ (ground state) to the $^4T_2$ and $^4T_1$, which results in fast non–radioactive decay to the metastable state ^2E as shown in Figure 2.10. These electrons emit characteristic radiations R_1 and R_2 lines when it relaxes to the lower energy level. The fluorescent R_1 and R_2 lines are sharp and intense which are sensitive to the change in pressure values [12, 64, 65].

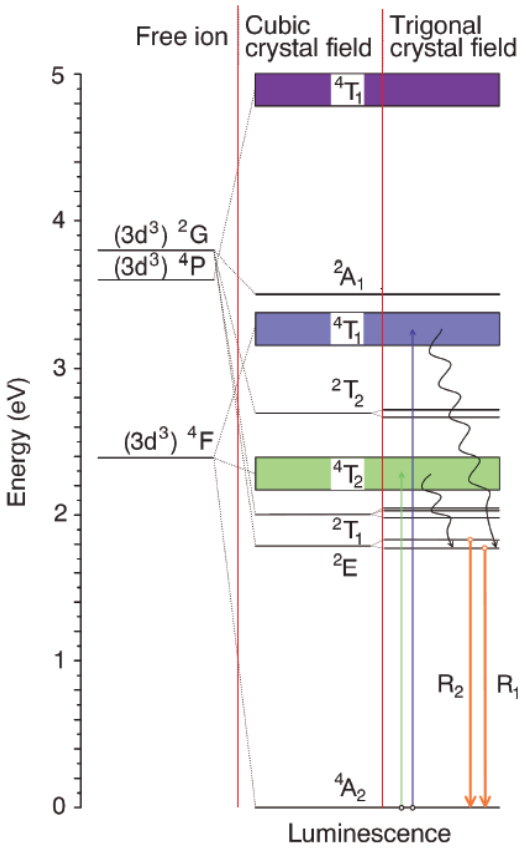

Figure 2.10. An Illustration of the ruby luminescence process due to the crystal field splitting of Cr^{3+}. The characteristic R_1 and R_2 lines are shown. The figure is taken and modified from - [66, 67].

The ruby crystal shows an almost uniform compression under hydrostatic conditions which results in the reduction of distance between Cr and O ions. This causes an increase in crystal field potential at Cr^{3+} ion which decreases the energy gap between the ^2E and $^4A_2$. This shift the R_1 and R_2 lines to the higher wavelength (see Figure 2.11). The shift of the R_1 line is used for the determination of pressure and the following expression was used for calibration at room temperature [64, 65].

$$P(\Delta\lambda) = \frac{A}{B}\left[1 + \frac{\Delta\lambda}{\lambda_0}\right)^B - 1] \qquad (2.6)$$

In Eq. (2.6) $\Delta\lambda$ is a shift in the wavelength of R_1 line for the set pressure and temperature while λ_0 is a wavelength at ambient conditions, A = 1904 GPa and B = 7.665 [64, 65].

The ruby luminescence technique was used for the in–situ pressure measurement. A Ruby ball of around 20 to 50 μm was placed inside the DAC as illustrated in Figure 2.12. The green laser of 10 mW was used to excite the ruby and the luminescent signal was coupled with the CCD spectrometer via fibber optic cable.

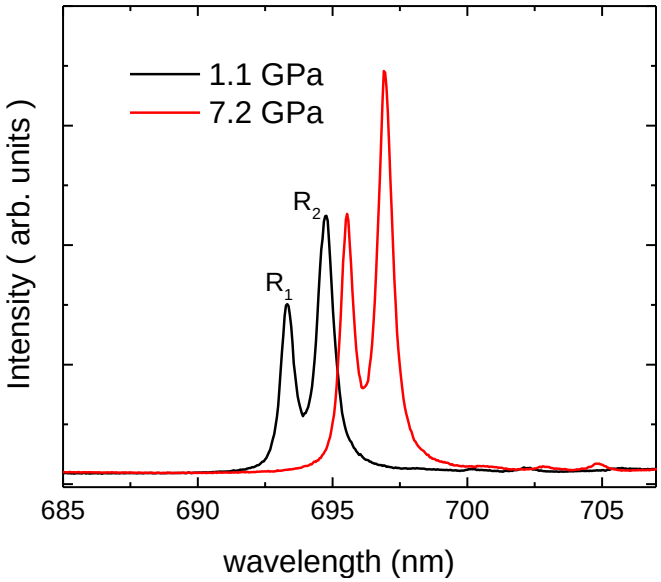

Figure 2.11. Intensity of R_1 and R_2 lines as function of wavelength at 1.1 GPa and 7.2 GPa at ambient temperature.

In this project the CCD spectrometer, Model: MS 260i^{TM} was used. It was a grating type (see Figure 2.1) imaging spectrometer where the detector was a high resolution CCD (charge couple device) camera. The luminescent signal was dispersed by a grating and recoded on the CCD camera. The resulting graph is shown in Figure 2.11, where the wavelength of R_1 and R_2 lines shows a shift in wavelength for the increased pressure.

2.2.5. Measuring with the LTHP setup

The schematic drawing for the reflectivity measurement inside the LTHP setup is shown in Figure 2.12. The in–situ over coating technique [1] cannot be adopted, because the sample needs to be inside the DAC in order to apply high pressure. This makes the measurements much more complicated because of the sample–diamond interface and low temperature cycling. In addition, the small size of the diamonds limits the sample size to few hundred microns.

The diameter of the sample compartment for the easyLab cell is around 300 µm, which is normally filled with samples of ~ 180 x 150 µm surface area. The incident and reflected beams need to pass through the series of refractions from the cryostat optical window and the diamond anvil in order to impinge on the sample's surface.

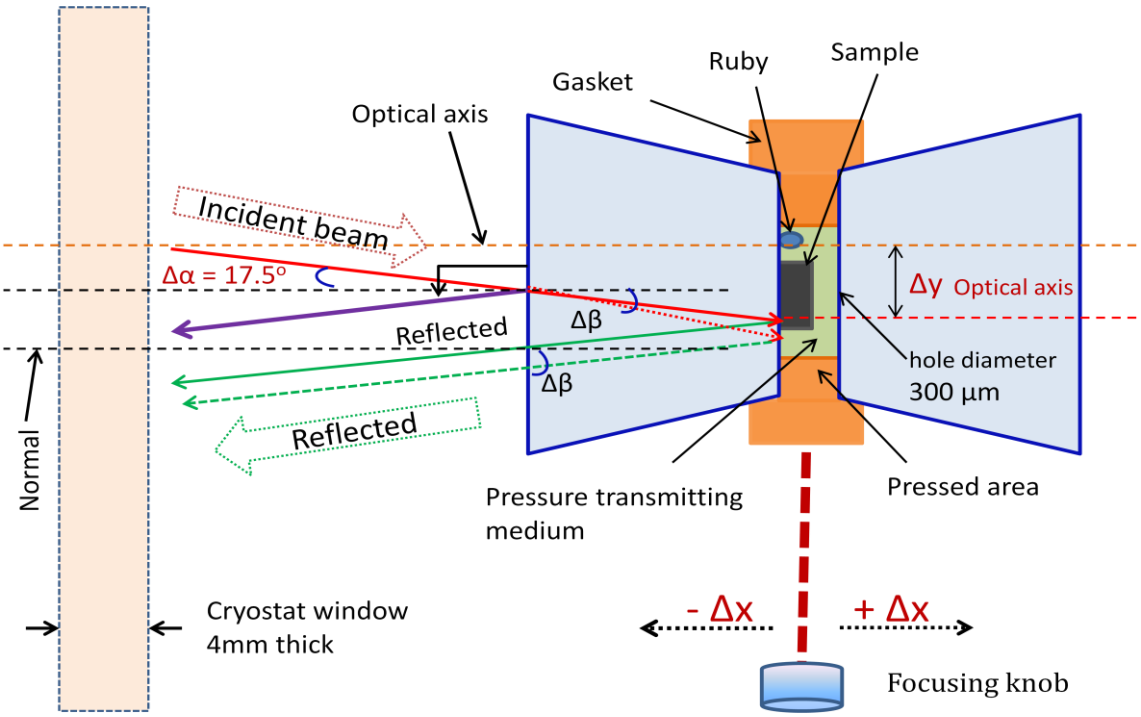

Figure 2.12. Measurement scheme for reflectivity inside the LTHP setup, where the DAC is mounted on the cryostat insert. The diameter of the sample–compartment is around 300 µm. The cryostat optical window at reflection side has a thickness of 4 mm. Δx is the change in focal length by moving the sample in the horizontal plane. The optical–axis is shown at the higher position, to illustrate the refractive processes of the beam. The normal is a perpendicular to the surface of the diamond [7, 71 - 74].

The numerical aperture inside the LTHP setup is *x*, which gives an incident angle $\alpha = 17.5^0$ with respect to the normal (black dashed–lines) as shown in Figure 2.12. The normal is a line which is perpendicular to the diamond's surface. The light beam strikes at the diamond surface making an angle of $\alpha = 17.5^0$, which faces further refraction due to the diamond regime ($n_{diamond} = 2.41$). The deviation of the incident beam in the diamond is represented with dotted–red lines with the deviation angle of $\Delta\beta$ [7, 71 - 74].

In transmission mode the scheme is different because the light beam will pass through the two cryostat optical windows. The light from the lamp will make the different incident angle with respect to the normal. This often creates a positional error at the sample surface, if the focal length is altered.

2.2.6. Behaviour of pressure inside easyLab cell during measurement

The easyLab cell (CryoDAC Mega) was used to carry out the high–pressure measurements, which shows a non linear increase in the pressure with cooling down. Therefore, in the following section a brief description about the behaviour of the cell with respect to the low temperature and high pressure is given.

The pressure (*P*), temperature (*T*) behaviour of easyLab cell at 297 K and 10 K is summarized in Table–2.2, during the mid infrared measurements. The pressure was set at room temperature for the each cycle, which increases to the higher values with cooling down. The difference between 297 K and 10 K is shown as pressure jump in the DAC.

The general trend for all pressure cycles as a function of the measured temperatures is plotted in Figure 2.13. The pressure jumps for the first five cycles were within +/- 0.5 GPa, which was increased more than 1 GPa for the higher pressure cycles. On the other hand, releasing pressure cycles shows a better stability in the pressure values at low temperatures.

In fact, the Syassen–Holzapfel cell does not show any pressure jumps with cooling down. The reason might be the sophisticated force driving assembly (thread–knee mechanism coupled with a geared system), which generates a uniform force at four corners of the DAC as explained in section 2.2.1. However, in the easyLab cell the pressure driving assembly is controlled by the four separated threaded–screws, which were rotated individually to generate the high pressure as illustrated in Figure 2.6.

In addition, the different parts of the easyLab cell, i.e. outer shell, pressure generating assembly and diamonds seats are fabricated by using different materials (Figure 2.5 (b)), which might cause different shrinkage rate with cooling down. Indeed, higher pressure jumps were observed, with the faster cooling rate. Thus, a slower cooling rate (~ 0.44 / minutes) with a small step increment (~ 0.2 GPa) in pressure was adopted in order to minimize the pressure jumps during the measurement.

Table 2.3, shows the maximum (P_{max}) and minimum (P_{min}) pressure measured at each temperature. P_{SDW} was the minimum pressure required to suppress the SDW gap at the corresponding temperature. The graphical representation of the table is shown in Figure 3.38.

Table 2.2: Pressure cycles, where the pressure jumps at 297 K (P_{297K}) and 10 K (P_{10K}) are given. The releasing–1 and 2 represents the pressure cycles which were measured after releasing the high pressure from 5.5 GPa to 2.4 GPa (releasing–1) and 1.3 GPa (releasing–2).

Cycles	P_{297K} (GPa)	P_{10K} (GPa)	Pressure Jump (GPa)
1	0.7	1.3	P_{297K} - P_{10K} = 0.6
2	1.04	1.44	0.4
3	1.34	1.86	0.52
4	1.63	2.24	0.61
5	1.82	2.38	0.56
6	2.27	3.74	1.47
7	2.97	3.85	0.88
8	3.22	4.55	1.33
9	3.9	5.5	1.6
Releasing - 1	2.46	2.94	0.48
Releasing - 2	1.35	1.67	0.32

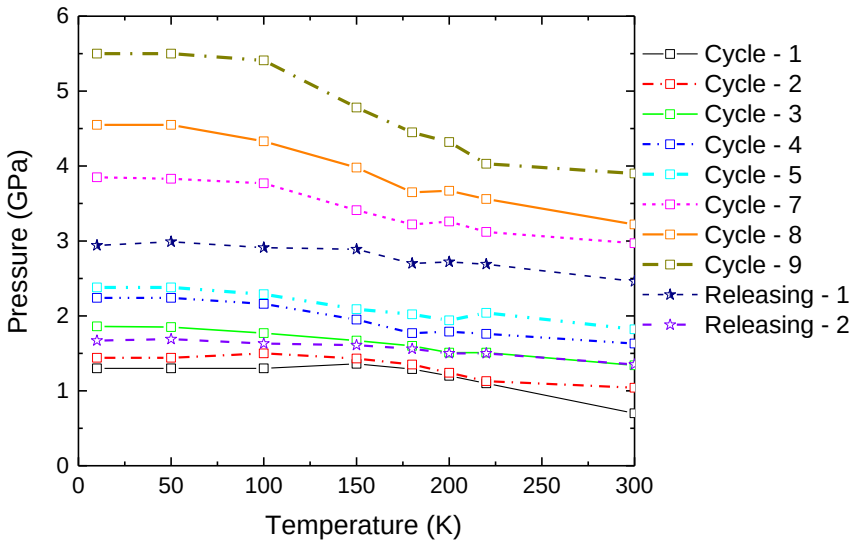

Figure 2.13. Behaviour of pressure inside the easyLab cell as a function of temperature (300–10K) observed in the pressures cycles during the mid infrared measurements. Releasing pressure cycles are represented with the dashed lines.

Table 2.3: Temperature cycles, where P_{min} and P_{max} represent the minimum and maximum pressures measured at each temperature. The P_{SDW} represents the pressure when the SDW gap was suppressed completely at the corresponding temperature. The graphical representation of the table is given in Figure 3.38.

S. No.	T (K)	P_{min} (GPa)	P_{max} (GPa)	P_{SDW} (GPa)
1	300	1.0	3.9	No SDW
2	220	1.1	4.0	No SDW
3	200	1.2	4.3	1.9
4	180	1.3	4.4	2.9
5	150	1.2	4.7	3.2
6	100	1.5	5.4	3.6
7	50	1.4	5.5	3.8
8	10	1.4	5.5	4.5

2.3. Optical parameters and relations

A typical optical process is illustrated in Figure 2.14, which shows the relation between reflection and refraction in combination with material and medium. The transmitted (T) and reflected (R_2) beams characterizes the optical properties of the material. For the perfectly reflecting surface almost 100 % of light will be reflected (R_s), while in case of absorptions the reflectivity will be decrease by certain specific amount depending on the nature of material. For transparent materials, the light will be transmitted through the material which is represented as T [9 - 12].

In this project the frequency dependent near–normal incident reflectivity (R_s) was measured from the surface of material and the absolute reflectivity was calculated by the following equation:

$$R(\omega) = \frac{R_s(\omega)}{R_{ref}(\omega)} \tag{2.7}$$

where, $R_s(\omega)$ is the reflectivity from the sample's surface, and $R_{ref}(\omega)$ is the reflectivity from a reference's material which has almost 100 % reflectance in the measured frequency range. For example, gold or silver mirrors can be used as a reference in the far and mid infrared ranges [9 - 12].

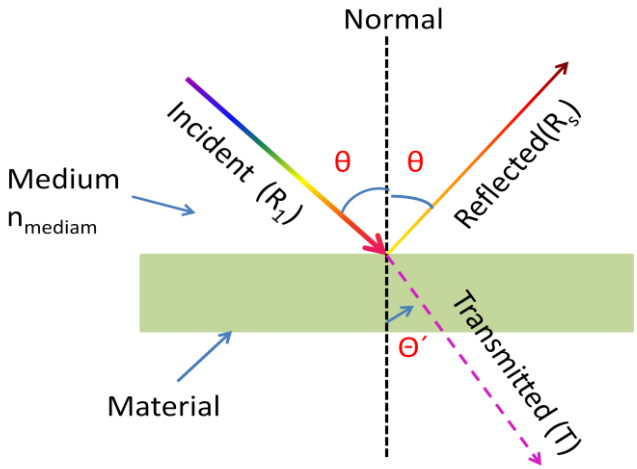

Figure 2.14. Illustrates a typical optical process happening at the material's surface. The normal is a line perpendicular to the surface of the medium. The angles θ and θ´ are measured with respect to the normal and n_{medium} represent the refractive index of the medium.

In the pressure measurements, the material was placed inside the diamond anvil cell (DAC) where the light beam was passed through the diamond in order to impinge on the sample (see Figure 2.15). Therefore, the Eq. (2.7) can be modified as follows [6, 8, 12]:

$$R_{s-d}(\omega) = \frac{R_s(\omega)}{R_g(\omega)} \tag{2.8}$$

where, $R_{s\text{-}d}(\omega)$ is the absolute reflectivity from the sample–diamond interface, $R_s(\omega)$ is the reflectivity of sample and $R_g(\omega)$ is the reflectivity of the pressed area from the CuBe gasket (see Figure 2.15). $R_{s\text{-}d}$ is related to the complex refractive index by the Fresnel relations as given by Eq. (2.9) [6, 8, 12, 173]:

$$R_{s-d} = \left|\frac{\tilde{n} - \tilde{n}_{dia}}{\tilde{n} + \tilde{n}_{dia}}\right| \tag{2.9}$$

where, $\tilde{n}_{dia}$ is 2.4, which is the refractive index of diamond used in the LTHP measurements. The complex refractive index ($\tilde{n}$) is related to the complex dielectric function (ε') by Eq. (2.10).

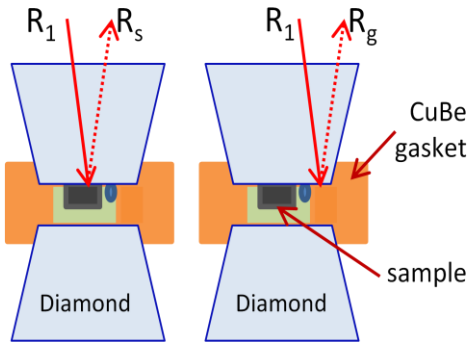

Figure 2.15. Arrangement for the reflectivity measurement inside the Diamond anvil cell (DAC). R_1 is an incident beam, R_s is the reflected beam from sample's surface and R_g is the reflection from the pressed area on the CuBe gasket.

$$\tilde{n}^2 = \varepsilon' \tag{2.10}$$

The complex refractive index and dielectric function can be split into their corresponding real and imaginary parts as follows:

$$(n + ik)^2 = (\varepsilon_1 + i\varepsilon_2) \tag{2.11}$$

Where, *n* is a refractive index and *k* is an extinction coefficient which depends on the dissipation of electromagnetic wave in the medium. $\mathcal{E}_1$ and $\mathcal{E}_2$ are real and imaginary parts of the dielectric function:

$$\varepsilon_1 = n^2 - k^2 \tag{2.12}$$

and the imaginary part of the dielectric function is

$$\varepsilon_2 = 2nk \tag{2.13}$$

Equations (2.12) and (2.13) can be used to calculate the optical conductivity of the material which is a response function of a material to electromagnetic waves. For a dissipative medium the complex optical conductivity consist of the real and imaginary parts as given in Eq.(2.14)) [8, 12, 154].

$$\sigma'(\omega) = \sigma_1(\omega) + i\sigma_2(\omega) \tag{2.14}$$

These quantities are related to the dielectric function as follows:

$$\sigma_1(\omega) = \frac{\omega\, \varepsilon_2(\omega)}{4\pi} \tag{2.15}$$

and

$$\sigma_2(\omega) = \frac{\omega\, (\varepsilon_1 - \varepsilon_2(\omega))}{4\pi} \tag{2.16}$$

For connecting the real and imaginary part of certain complex response function, the Kramer–Kronig relations can be used. It provides the sets of bidirectional mathematical equations for the function which is analytic (converging power series) in the upper half plane. By using these equations, the components of the complex dielectric constant or conductivity can be extracted if only one optical parameter, i.e. reflectivity or absorbance is available. The equation can be express as Eq. (2.17) for the normal incident reflectivity measurement for the broad frequency range ($\omega \rightarrow \infty$) at the surface covered by a transparent window [6, 8, 12, 158].

$$\phi(\omega_0) = -\frac{\omega_0}{4\pi} P \int_0^{\infty} \frac{\ln R_{s-d}(\omega)}{\omega^2 - \omega_0^2} d\omega + [\pi - 2\tan^{-1}\left(\frac{\omega_B}{\omega_0}\right)] \quad (2.17)$$

where, $P\int$ represent the principle value of the integral, $R_{s\text{-}d}$ is the reflectivity for the sample–diamond interface, ω_B is the position of reflectivity at imaginary axis. ω_B will tends to infinity for the sample–air interface and the second term in Eq. (2.17) will be diminished [8, 12, 158].

2.4. The Lorentz–Drude Model

The Lorentz–model is a classical model which describes an atom as a big mass (nucleus) connected to another smaller mass (electron) with the help of a spring and oscillates with a certain natural frequency. The interaction of electromagnetic waves changes the natural frequency of the oscillator, which appear in damping effects inside the medium. Mathematically it can be expressed as Eq. (2.18), where the effect of magnetic field is assumed to be zero [8]:

$$m\frac{d^2r}{dt^2} + m\Gamma\frac{dr}{dt} + m\omega_0^2 r = -eE_{loc} \quad (2.18)$$

Where, r is displacement, m the mass, e the charge of electron, ω_0 the natural frequency and E_{loc} the local electric field acting on the electron. The second term on the left hand side is the viscous damping force where Γ is a scattering rate and the third term defines the restoring force is Hooke's law.

The Drude model considers the valance electrons as freely moving particles, which can be scattered or deflected after collision with other electrons, atoms or defects. This leads to a negligible restoring force and Eq. (2.18) can be modified as follows [8]:

$$m\frac{d^2r}{dt^2} + m\Gamma\frac{dr}{dt} = -eE_{loc} \quad (2.19)$$

Thus, by using equations (2.18) and (2.19), an expression for the real (ε_1) and imaginary (ε_2) parts of the dielectric function can be obtained as follows [8]:

$$\varepsilon_1 = 1 + \frac{4\pi Ne^2}{m} \frac{(\omega_0^2 - \omega^2)}{(\omega_0^2 - \omega^2)^2 + \Gamma^2\omega^2} \quad (2.20)$$

and

$$\varepsilon_2 = \frac{4\pi N e^2}{m} + \frac{\Gamma\omega}{(\omega_0^2 - \omega^2)^2 + \Gamma^2\omega^2} \quad (2.21)$$

For more than one electron bounded with an atom of density N_j resonating with the frequency ω_j, the complex dielectric function ($\mathcal{E}'$) can be defined as follows:

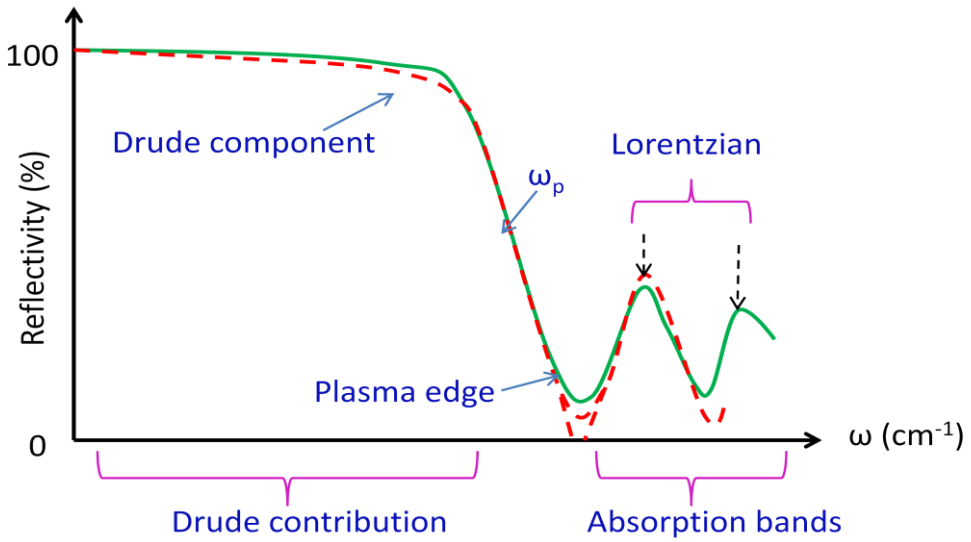

Figure 2.16. An illustration of the Lorentz–Drude fit (red dashed lines) to the reflectivity data (green solid lines). The Drude component represents the free electron behaviour of a metal, where the restoring force is negligible. The Lorentz oscillator shows the absorption bands where the electrons are bonded with the nucleus [8].

$$\varepsilon' = 1 + \frac{4\pi e^2}{m} + \sum_j \left(\frac{N_j}{(\omega_j^2 - \omega^2) + i\Gamma_j\omega}\right) \quad (2.22)$$

and the quantum mechanical form of the above equation can be obtained as follows:

$$\varepsilon' = 1 + \frac{4\pi e^2}{m} + \sum_j \left(\frac{Nf_j}{(\omega_j^2 - \omega^2) + i\Gamma_j\omega}\right) \quad (2.23)$$

In classical mechanics (see Eq. (2.22)) ω_j is the resonant frequency of the bounded electron while in quantum mechanics (see Eq. (2.23)), it is a transition frequency between two atomic states separated by an energy of $\hbar\omega_j$, f_j is an oscillator–strength which defines the probability of the quantum mechanical transition between two atomic states. For $\mathcal{E}_1$ = 0, the

characteristics frequency is called the plasma frequency (ω_p) which can be obtained as follows [8]:

$$\omega_p = \frac{4\pi N e^2}{m} \tag{2.24}$$

Thus, Eq. (2.23) can be modified as follows:

$$\varepsilon'(\omega) = \varepsilon_\infty(\omega) + \frac{\omega_p^2}{\omega^2 + i\Gamma\omega} + \sum_j \left(\frac{\omega_{p,j}^2}{(\omega_j^2 - \omega^2) + i\Gamma_j \omega}\right) \tag{2.25}$$

where, $\mathcal{E}_\infty(\omega)$ is the dielectric constant at high frequencies, the second term is the Drude component and third term is the Lorentz oscillator. The Drude–Lorentz model was used in order to analyze the reflectivity spectra for the measured compounds as illustrated in Figure 2.16. The metal like reflectivity was fitted with a Drude component while the absorption bands were fitted with Lorentz oscillators [8].

The model was extended according to the approach by S. J. Moon et al [142] in order to describe the two different types of charge carriers, i.e. electrons and holes. Thus, Eq. (2.25) was modified as follows [154, 170].

$$\varepsilon'(\omega) = \varepsilon_\infty(\omega) - \frac{\omega_{PN}^2}{\omega^2 - i\omega\Gamma_N} - \frac{\omega_{PB}^2}{\omega^2 - i\omega\Gamma_B} - \sum_j \frac{S_j^2}{\omega_j^2 - \omega^2 - i\omega\gamma_j} \tag{2.26}$$

Where, $\mathcal{E}_1(\omega)$ and $\mathcal{E}_2(\omega)$ are the real and imaginary parts of dielectric function, ω_{PN}^2 and ω_{PB}^2 are the plasma frequencies and Γ_N , Γ_B are the widths of sharp and broad Drude components respectively. S_j^2 represents a mode strength of the harmonic oscillator, with the spectral width of γ_j at the central frequency ω_j [142, 154, 170, 173].

2.5. Sample preparation and Experimental details

In this section the technical details relating to the measurements for each material is described briefly.

2.5.1. $SrFe_2As_2$

The single crystals of $SrFe_2As_2$ were obtained from W. Z. Hu from the Beijing National laboratory for condensed matter Physics, Beijing, China [135]. The surface quality of the crystal is shown in Figure 2.17. The material has layered structure with a bulk modulus less than 100 GPa which makes it very fragile and soft. This makes the crystal prone to break during polishing and DAC filling. Since the as grown surface was not good enough for reflectivity measurements, it was polished down in order to get a finished surface as shown in Figure 2.18.

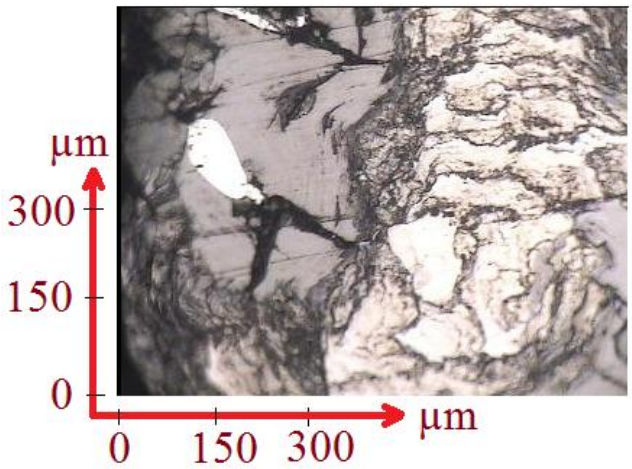

Figure 2.17. The surface quality of the single crystal of $SrFe_2As_2$ pnictide.

The easyLab cell (CryoDAC Mega) was used to carry out the measurements. The 400 µm thick CuBe gasket was pressed with DAC and drilled with EDM (Electric discharge machine) micro–driller. The technical details of the measurements are summarized in Table 2.1.

A very fine polished piece of $SrFe_2As_2$ crystal was used to fill the DAC (see Figure 2.19) with CsI as a pressure transmitting medium. The low–temperature and high–pressure measurements were carried out with the LTHP setup, which was coupled with the Vertex–80 spectrometer. Nine pressure cycles were measured with two releasing pressures in the mid infrared range. For the far infrared range, the DAC was drilled with 400 µm hole, in order to

fill with larger sample as shown in Figure 2.20. Four pressure cycles with eight sets of low temperatures were measured in the far infrared range.

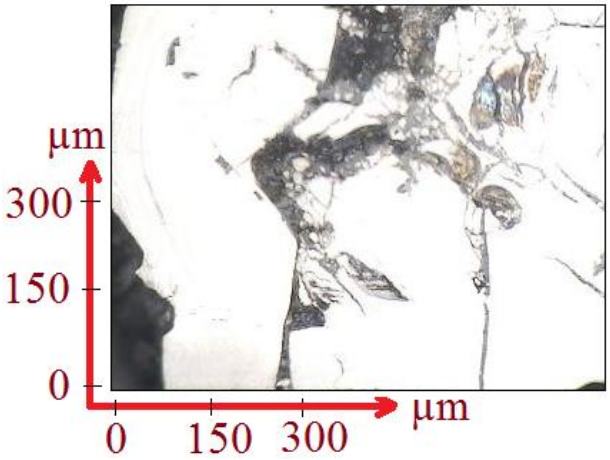

Figure 2.18. The surface quality of the single crystal of $SrFe_2As_2$ after fine polishing.

For further analysis, the far and mid infrared spectra were merged for the similar temperatures and closest pressures, within a range of +/- 0.5 GPa. Furthermore, the spectra were separated from the different pressure cycles for the pressure within +/- 0.5 GPa at various temperatures. The spectra for the similar pressure (+/- 0.5 GPa) of different temperatures were grouped and presented as the "pressure cycles" in section 3.3.1. In "temperature cycles" as shown in section 3.3.2, the pressure dependent spectra for each temperature are grouped in order to observe the explicit behaviour of the pressure at each temperature.

Table 2.1: Summary of the technical details regarding the type of measurements for the $SrFe_2As_2$ crystal.

S. No.	Type	No. of pressure cycles	Gasket material	Initial thickness (µm)	Indented area (µm)	Hole diameter (µm)	Sample thickness (µm)	Starting Pressure (GPa)
1	FIR	4	CuBe	400	110	400	40	0.18
2	MIR	11	CuBe	400	70	300	45	0.7

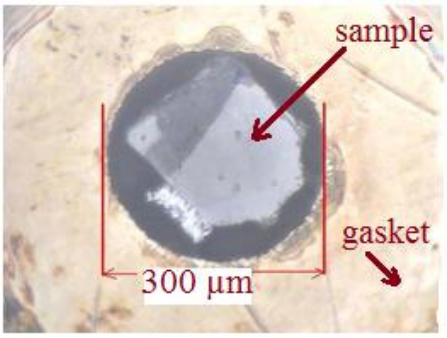

Figure 2.19. Filled DAC with the $SrFe_2As_2$ crystal for measuring the mid infrared range as shown in reflection mode. The photo is taken under the Bruker IFS66 microscope at 15 X magnification.

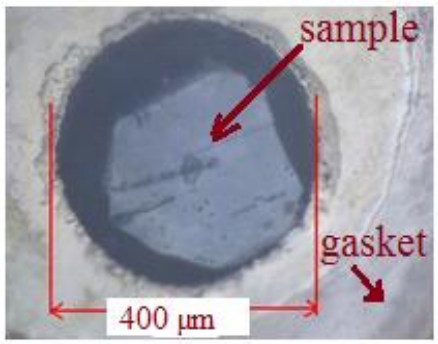

Figure 2.20. Filled DAC with the $SrFe_2As_2$ crystal for measuring the far infrared range as shown in reflection mode. The photo is taken under the Bruker IFS66 microscope at 15 X magnification.

2.5.2. $SrFe_{1.9}Co_{0.1}As_2$

The single crystals of $SrFe_{1.9}Co_{0.1}As_2$ were obtained from A. Jesche from the Max Planck Institute for Chemical Physics, Dresden, Germany [92]. The surface quality of the polished and raw samples is shown in Figure 2.21 (a). The thickness of the raw samples was around 900 µm, which was polished down to 50 µm.

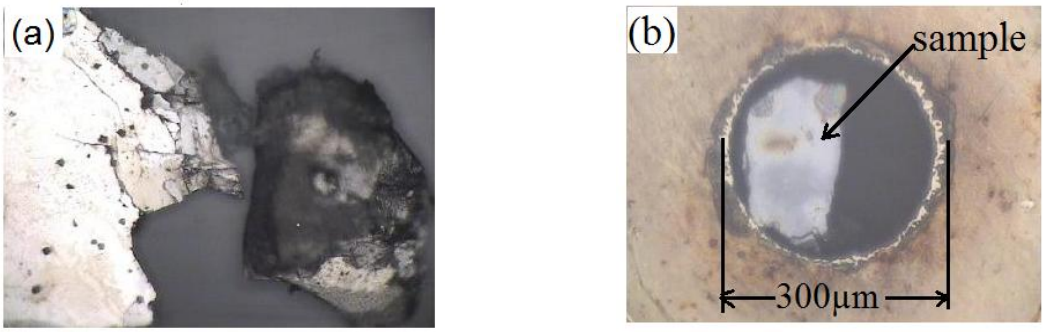

Figure 2.21. Surface quality of the $SrFe_{1.9}Co_{0.1}As_2$ crystals (a) Mirror like polished and unpolished crystals are shown with 4 X magnification. (b) Filled DAC with the sample at 15 X magnification.

The CuBe gasket was indented with the easyLab cell and drilled with a 300 µm hole. The well polished sample was cut and filled in the easyLab cell as shown in Figure 2.21 (b). The closing pressure of DAC was 0.4 GPa. The low temperature and high pressure measurements were carried out with the LTHP setup which was coupled with the Vertex–80 spectrometer.

2.5.3. EuB_6

The single crystals of EuB_6 were obtained from Jungo Kim from the department of Physics, university of Toronto, Canada [79]. The quality of the sample's surface is shown in Figure 2.22 at various locations. The CuBe gasket was indented and drilled by the easyLab cell with a diameter of 300 µm. The measurements were carried out with the LTHP setup coupled with the Vertex–80 spectrometer.

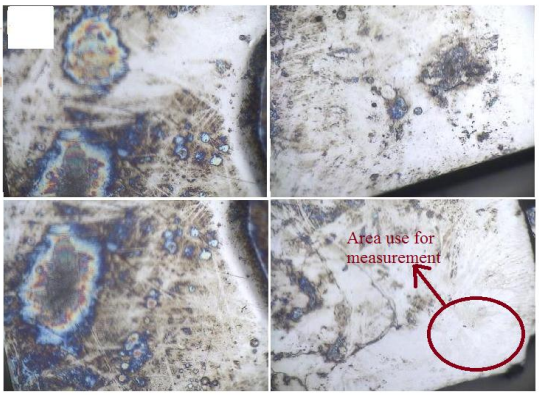

Figure 2.22. Surface quality of the polished EuB_6 with 4 X magnification at various locations on the crystal surface. The marked area was selected to fill the DAC.

The near–normal incident reflectivity was measured for the nine sets of low temperatures at seven different pressures. In order to check the reproducibility, two releasing pressures cycles were measured at 1.0 GPa and 0.4 GPa. This gave a huge amount of spectra for the various pressure and temperature values. Therefore, the spectra were organized into two main groups, i.e. pressure and temperature cycles.

The "pressure cycles", include the spectra measured at each temperature (300–10 K) for the set pressure value which is presented in section 4.2.1. In "temperature cycle group", the spectra for the various pressures at constant temperature were separated from the pressure cycles and presented in section 4.2.2 for the few selected temperatures.

3. The iron arsenide pnictides

3.1. Physical properties of iron arsenide pnictides

A generic phase diagram for the $SrFe_{2-x}Co_xAs_2$ compound is shown in Figure 3.1 as a function of doping and pressure. The material shows three distinct phases, i.e. paramagnetic PM), antiferromagnetic (AFM) and superconducting (SC) phase. At room temperature, the material is paramagnetic with tetragonal crystal symmetry [136, 137, 141].

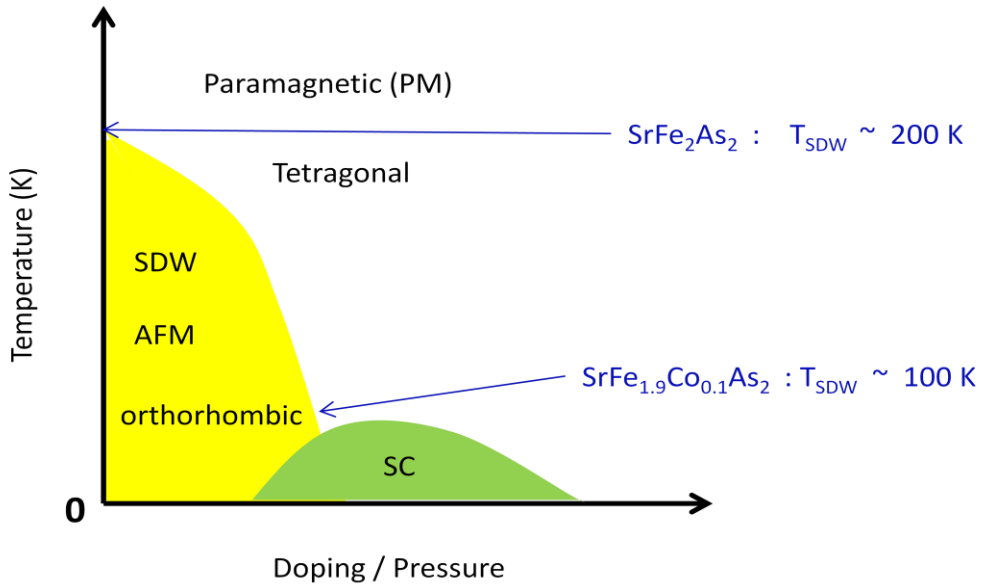

Figure 3.1. A generic phase diagram of iron–pnictide based superconductors as a function of doping and pressure. SDW stands for spin density wave, AFM for the antiferromagnetic and SC for the superconducting phase. T_{SDW} is the SDW transition temperature shown for the measured $SrFe_{2-x}Co_xAs_2$ compound at x = 0 and 0.1.

The material undergoes a structural transition from tetragonal to orthorhombic and a transition from paramagnetic (PM) to antiferromagnetic (AFM) at around 200 K. The phase transition (yellow colour in Figure 3.1) is identified as a spin density wave (SDW) ground state on the basis of first principle calculations and neutron diffraction experiments. The SDW state is an antiferromagnetic ground state which occurs due to modulation of the spins of itinerant electrons with an anti–parallel alignment [136, 137, 141, 155].

Doping or application of high pressure suppresses the structural and magnetic transitions and leads to the induction of a superconducting (SC) state as shown in Figure 3.1. The $SrFe_{2-x}Co_xAs_2$ system with doping concentration x = 0 and 0.1 is indicated at their approximate positions in the phase diagram. At x = 0.1, the material lies close to the boundary of the SDW and the superconducting phase, where a small amount of pressure would be enough to induce the superconducting state [89, 93, 137, 141].

It is unusual for (122)–pnictides, that electron or hole doping suppresses the phase transitions in a similar way with the induction of superconducting state. The superconducting state is also suppressed if the doping or pressure exceeds the optimum critical value [89, 93].

3.1.1. The AFe_2As_2 Systems

The generic formula of the compound is AFe_2As_2, where *A* is normally an alkaline earth metal, i.e. Ba, Ca or Sr. They form a body centre tetragonal lattice with space group of I4/mmm, which has two formula units per unit cell. The crystal structure is shown in Figure 3.2 which belongs to the $ThCr_2Si_2$ type system [*28*, 85, 87].

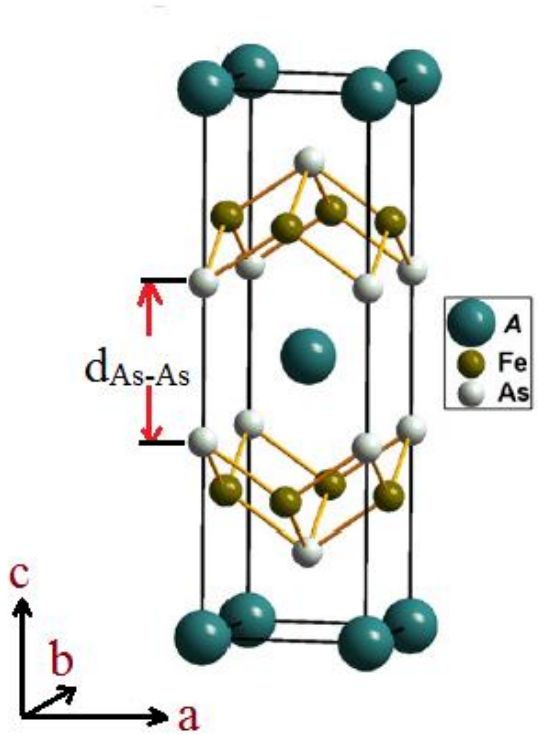

Figure 3.2. Crystal structure of $SrFe_2As_2$ at room temperature. The $d_{As\text{-}As}$ is an interlayer distance, separated by Sr atoms. The picture was taken and modified from – [28].

The iron atoms form square lattices, which are connected in such a way that the arsenide atoms lie at the apex of iron atoms with four irons as the nearest neighbours. This forms the

layered structure of Fe–As atoms, which are separated by an atomic sheet of strontium atoms. The separation between the layers is shown by the distance $d_{As\text{-}As}$ in Figure 3.2.

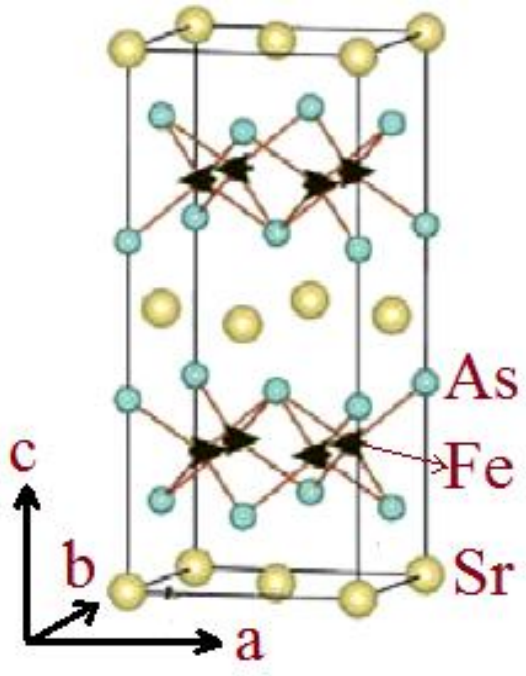

Figure 3.3. Crystal structure of $SrFe_2As_2$ below T_{SDW}, after the structural and magnetic transitions. The magnetic moment of iron atoms align parallel to the a–axis. The picture was taken and modified from – [35].

The distance $d_{As\text{-}As}$ shows a decreasing trend, if iron is replaced by some other transition metals with a higher atomic number. However, the interaction between the adjacent layers and atomic sheet is found to be very weak with a Bulk Modulus less than 100 GPa for $SrFe_2As_2$. Therefore, the crystal is very soft and fragile which lies at the border line of mechanical stability [*28*, 115, 132].

The crystal structure below T_{SDW} is shown in Figure 3.3 where the crystal symmetry is orthorhombic (Fmm) and iron atoms form an antiferromagnetic collinear pattern in the ab–plane with parallel spins [35, 36, 115].

The situation can be clearly observed from the top view as shown in Figure 3.4, where the c–axis is perpendicular to the plane of the page. The parallelization of iron spins in ab–planes creates the repulsive forces between iron atoms, which push the iron atoms farther apart in order to balance these repulsive forces. As a result, the arsenic atoms move towards the iron square lattice, which appears as a considerable shrinkage of the c–axis [35, 36, 115, 131, 132].

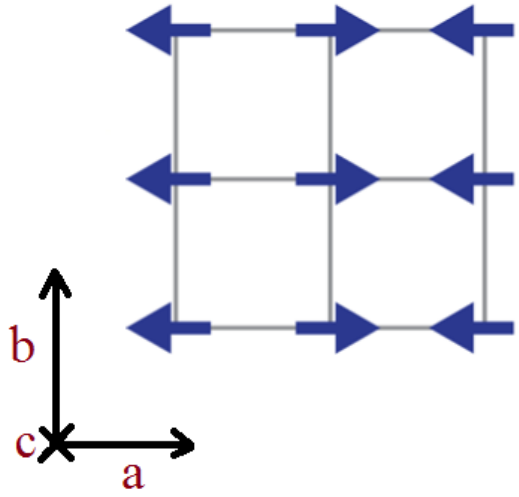

Figure 3.4. Magnetic moments of the iron atoms in $SrFe_2As_2$ below T_{SDW}*, where the c–axis is perpendicular to the plane of the page. The picture was taken and modified from the reference– [36].*

3.1.2. Hall effect Measurements

The temperature–dependent Hall–Effect measurement as reported by G. F. Chen et al [159] for $SrFe_2As_2$ is shown in Figure 3.5. The Hall–coefficient is almost temperature independent and negative above 200 K, while it increases slightly to a positive value below 190 K, indicating an increased concentration of holes in the conduction carriers. It drops down to a negative value for temperatures below 100 K, which indicates a drastic increase in electronic current. The absolute value of R_H at 2 K is 35 times higher than the value at 300 K [142, 154].

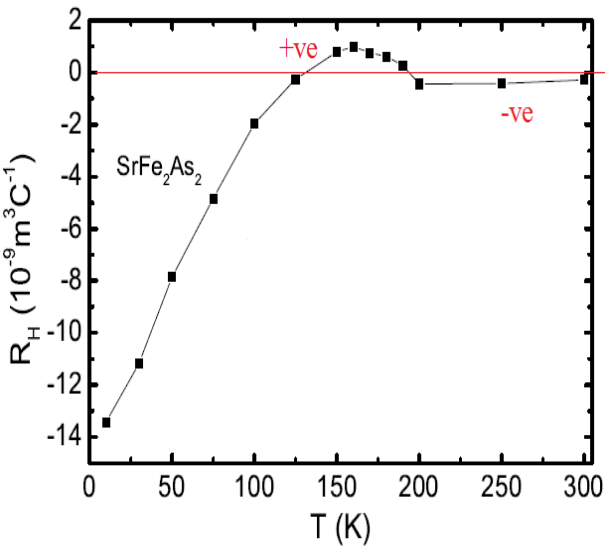

Figure 3.5. Temperature–dependent Hall–coefficient for $SrFe_2As_2$ as reported by G. F. Chen et al [159].

According to band structure calculations, there are "three hole pockets" at the Γ point and "two electron pockets" at the M point [159]. At the onset of the SDW state, the hole pockets

are almost fully gapped, and the electrical conduction is explicitly due to the partially gapped electron pockets, which appears as a negative R_H value [160, 159]. This is a reasonable justification for using two Drude terms for fitting the reflectivity data in the paramagnetic state ($T > T_{SDW}$) [142, 154].

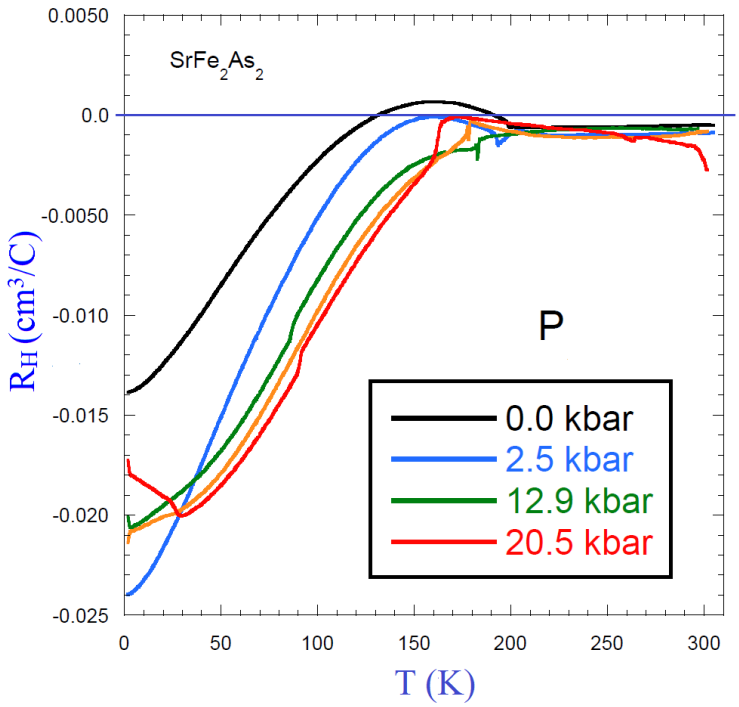

Figure 3.6. Temperature dependent Hall–coefficient for $SrFe_2As_2$ at various pressures, as reported by D. J Padilla [160].

Figure 3.6 shows the temperature dependent Hall–coefficient (R_H) for the various pressures as reported by D. J Padilla [160]. It is obvious that the application of high pressure decreases the absolute value of R_H, but the overall temperature–dependent changes remains similar. This is a clear indication that electrons are the majority conduction carriers, even if the SDW gap is suppressed. This suggests that the suppressed SDW state can be fitted with a single Drude component [160, 142].

3.1.3. Effects of doping

Doping $SrFe_2As_2$ by substituting iron with another transition metal leads to the fast suppression of the magnetic and structural transitions and the appearance of a superconducting state [89, 93].

Figure 3.7 shows the superconducting transition temperature (T_c) for $SrFe_{2-x}M_xAs_2$ as a function of doping concentration (x), where M represents the transition metals which are

successfully used for synthesis. The synthesis with zinc is not yet successful. In most cases, the structural and magnetic transitions are suppressed with emergence of a superconducting state. For manganese and chromium the magnetic and structural transitions are suppressed but without emergence of superconductivity [89, 93].

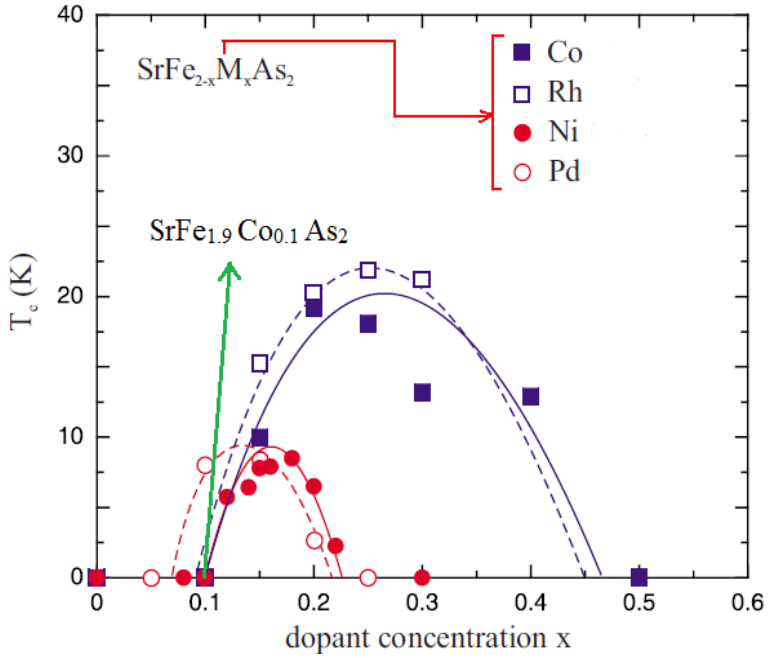

Figure 3.7. The phase diagram represents the superconducting–temperature (T_c) as a function of doping concentration (x), for 3d and 4d transition metals. Solid square/circle represents the 3d–electron metal (Co and Ni). Open square/circle represents the 4d–metals (Rh and Pb). References from: Co [89] , Rh [101] , Ni [98], Pd [105].

Figure 3.7 shows a dome–like behaviour of the superconducting–temperature (T_c) as a function of doping concentration for various transition metals. For Co [89] and Rh [101] the maximum transition temperature rises up to 20 K at doping (x) value of 0.25. In case of Ni [98] and Pd [105], the transition temperature rises up to around 10 K, at doping concentration of ~ 0.15. In most cases, the lattice constants increase along a–b planes and shrink along the c–axis. The compound $SrFe_{1.9}Co_{0.1}As_2$ marked with a green arrow was used for the infrared measurements under high–pressure [101 - 109].

3.1.4. High pressure Electrical transport experiments

In this section, a brief literature review of the electrical transport measurements under high pressure for $SrFe_2As_2$ will be discussed.

Figure 3.8 shows the electrical transport measurements carried out by T. C. Kobayashi et al [30], with an indenter type pressure cell [129] in uniaxial configuration, by using three different kinds of pressure–transmitting media.

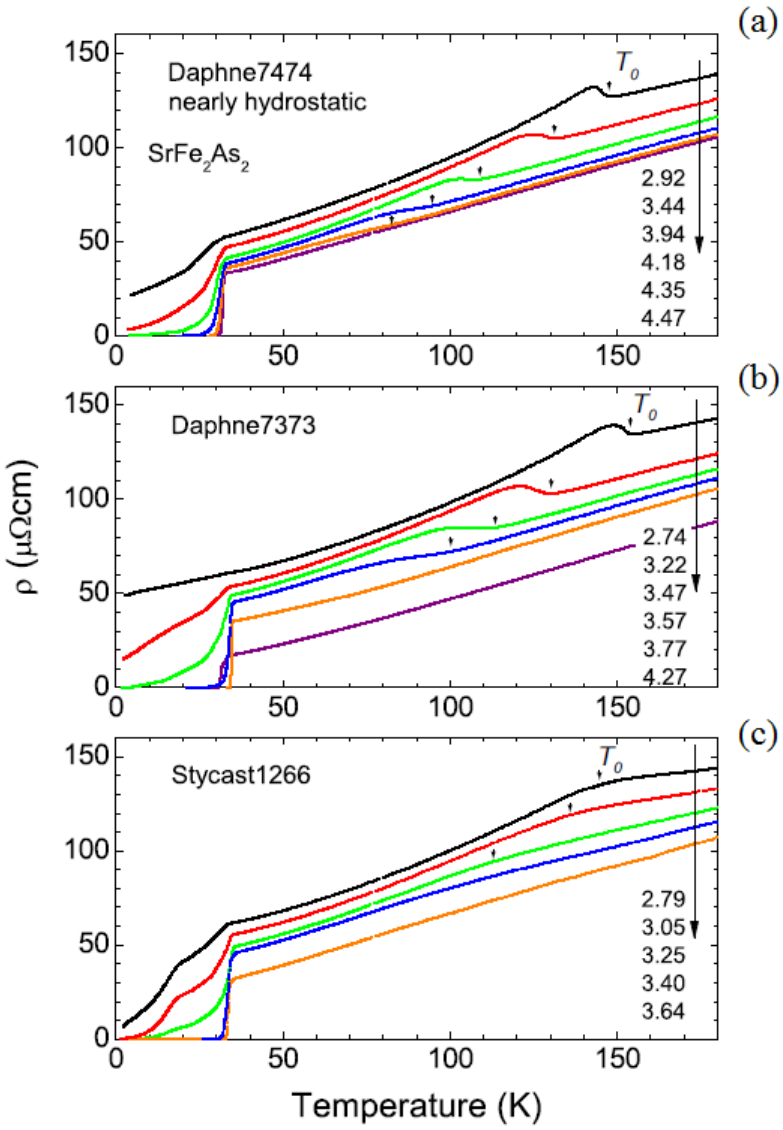

Figure 3.8. Temperature–dependence of the DC–resistivity under high pressure for three types of pressure–transmitting media. (a) Daphne 7474 (b) Daphne 7373 and (c) Stycast 1266. The picture is taken from T. C. Kobayashi [30] et al.

The sharp peak at T_0, represents the transition from the paramagnetic (tetragonal) to the antiferromagnetic (orthorhombic) phase which is related to the ordering of iron spins. The shape and position of T_0 is changed with respect to the pressure–transmitting medium [136, 141, 155].

The critical pressure (P_c) relating to the suppression of transition varies with different pressure–transmission media, which is listed below. The Daphne 7474 gives the most hydrostatic conditions [30]:

Daphne7474; P_c = 4.4 GPa; which is almost hydrostatic.

Daphne 7373; P_c = 3.6 to 3.7 GPa.

Stycast 1266; P_c = 3.4 to 3.5 GPa.

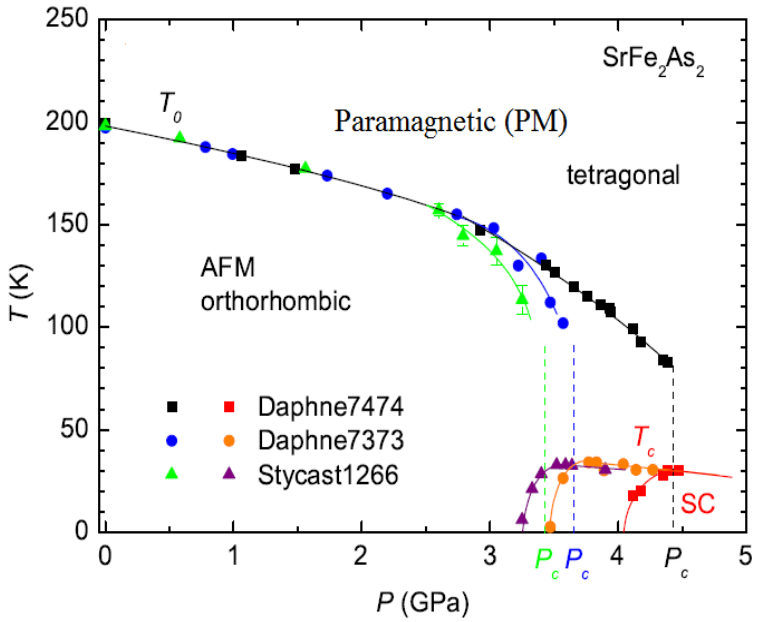

Figure 3.9. The phase diagram shows the pressure–dependence of phase transition temperature (T_0) for three kinds of pressure–transmitting media. The measurements are done in uni–axial configuration with the indenter–type pressure cell. The picture is taken from T. C. Kobayashi et al [30].

The phase diagram for three different kinds of pressure–transmitting media in uniaxial configuration is shown in Figure 3.9. The zero–resistance temperature is taken as the critical superconducting temperature and the phase is represented as SC in the phase diagram [136, 141, 155].

The phase boundaries between PM and AFM start to split for pressures higher than 2.5 GPa and below 180 K, which corresponds to the non hydrostatic behaviour of the pressure–transmitting media. Even though, the pressure is applied along the c–axis; the critical pressure value (P_c = 4.4 GPa) measured with Daphne7474 is almost consistent with the measurement done with a cubic anvil cell and Glycerine as a pressure–transmitting medium (see Figure 3.12). This suggests that under better hydrostatic conditions, the uniaxial and cubic anvil configuration will yield similar results [29, 30].

Figure 3.10 shows the electrical transport measurement carried out by using a cubic–anvil pressure cell, as reported by K. Matsubayashi et al [29]. The Glycerine was used as a pressure–transmitting medium. The peak at the temperature T_s is related to the magnetic and structural transition of $SrFe_2As_2$.

The transition shifts monotonically to lower temperatures with increasing pressure and disappears completely at around 5 GPa. At 4.5 GPa, the resistivity shows a sharp drop which approaches to zero–resistance at T_c ~ 23 K as shown in Figure 3.10 (b). However, at 5 GPa, the drop in resistivity becomes sharper and T_c increased to ~ 32 K. For pressures higher than 5 GPa the drop in resistivity starts to become broader again and T_c starts to decrease [29].

K. Matsubayashi et al [29] also performed ac–susceptibility measurement to probe the bulk nature of the superconducting state. The real part of the ac–susceptibility χ'_{ac} as a function of temperature is shown in Figure 3.11 at various pressures. The modulation field is applied along the ab–plane.

For pressures higher than 3 GPa, χ'_{ac} starts to deviate from zero at 10 K, which indicates the shielding response of the material. At 5.0 GPa, the shielding reaches to around 60 % indicating the existence of a bulk volume fraction with diamagnetic response. This mixed state can be related to the onset of zero–resistance or a partially superconducting state [29]

At 5.5 GPa χ'_{ac} reaches to 90 %, which indicates more prominent shielding and can be related to the appearance of bulk superconducting state. The structural and magnetic transitions are completely suppressed for that regime [29].

Figure 3.12 shows the phase diagram drawn as reported by K. Matsubayashi et al [29], where the pressure–temperature behaviour of the transition temperature (T_s) is shown for Glycerine as a pressure–transmitting medium. T_s shows a sharp decrease for pressures above 3.5 GPa. The critical–pressure (P_c) is the pressure required to suppress the structural and AFM transition, with an emergence of the superconducting (SC) state. The superconducting

transition temperature (T_{SC}) corresponds to the 50 % of the full shielding effect of $\chi'_{ac,}$ which shows an overlapping of AFM and SC states. The bulk superconducting state corresponds to the 90 % shielding effect, which is started at 5.5 GPa.

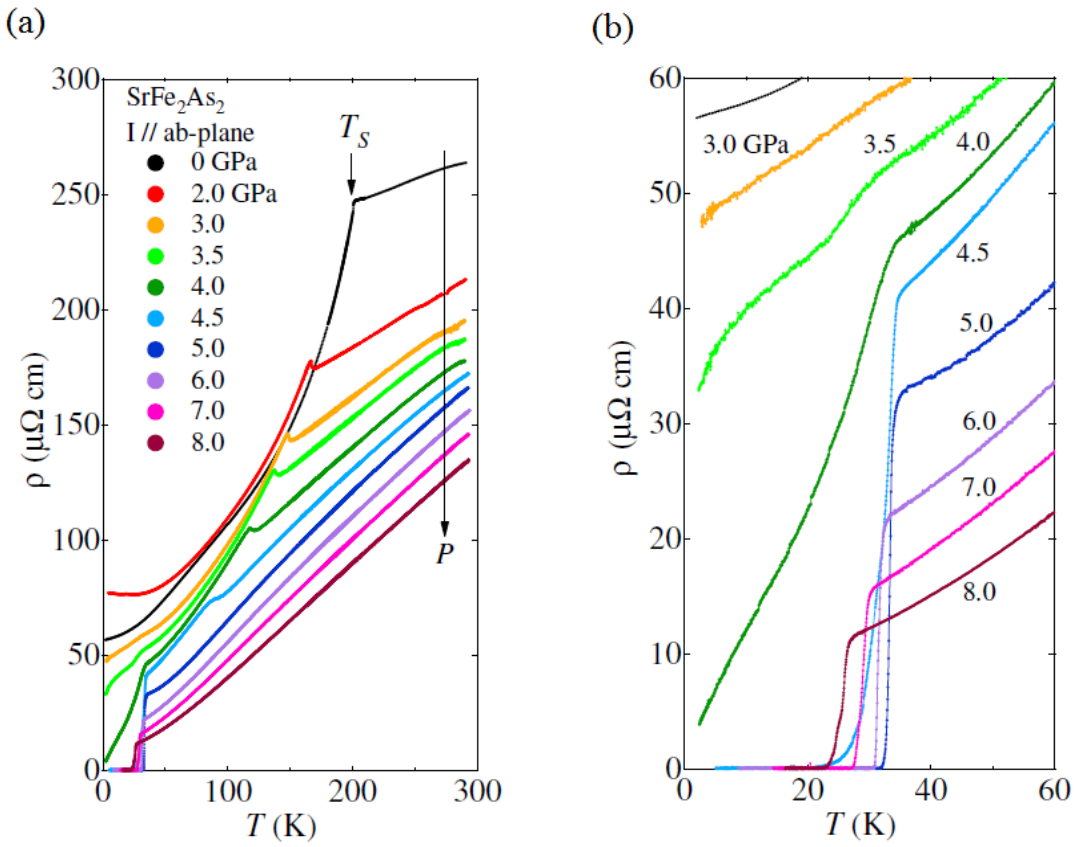

Figure 3.10. (a) Temperature–dependence of the DC–resistivity under high–pressure by using Glycerine as a pressure transmitting medium, with a cubic anvil cell. (b) Enlarged view of left panel in the low–temperature regime. The picture is taken from K. Matsubayashi et al [29].

In retrospect, the effect of high pressure and cobalt doping on $SrFe_2As_2$ compound cannot be considered exactly the same. For instance, the distance between the Fe and As atoms changes differently with pressure or when arsenic is replaced by phosphorous. In addition, Fe–As layers show significant changes when an extra electron or hole is inserted either by chemical doping or by changing crystal symmetry (high pressure). In fact, chemical doping introduces some sort of distortion in system and affects most of chemical bonding, which can also results in a change in crystal symmetry [99, 100, 180].

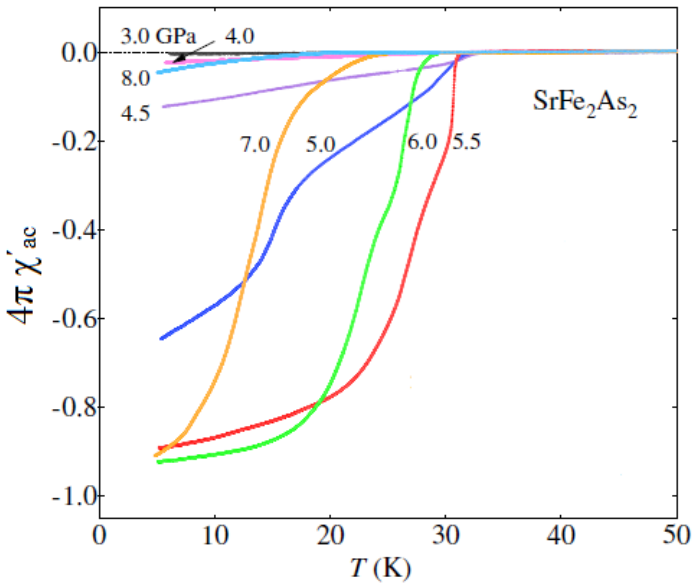

Figure 3.11. Temperature–dependence of the real part of the ac–susceptibility. The modulation field is applied along the ab–plane. The picture is taken from K. Matsubayashi et al [29].

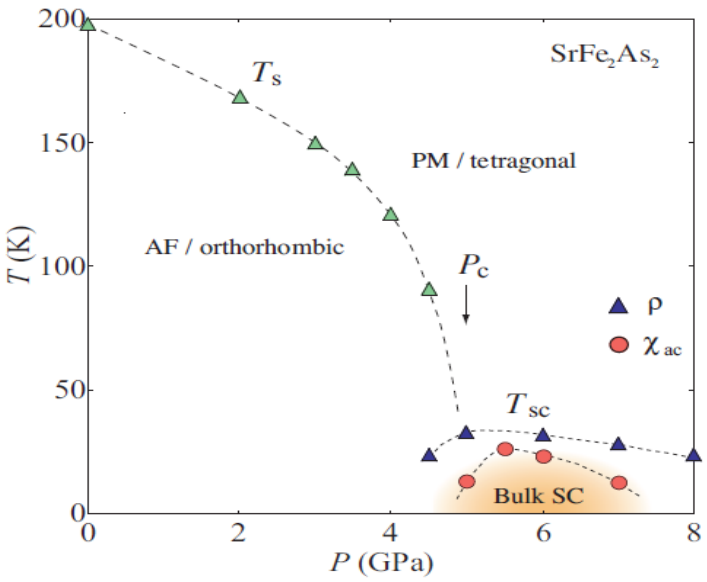

Figure 3.12. Phase diagram showing the pressure–dependence of the phase transition temperature (T_s) with Glycerine as a pressure–transmitting medium. The measurement is carried out with a cubic–anvil cell. The picture is taken from K. Matsubayashi et al [29].

3.2. Infrared spectroscopy

The $SrFe_2As_2$ shows interesting features in the infrared range at low temperature. In Figure 3.13, the reflectivity (R) of $SrFe_2As_2$ is shown at various temperatures as reported by W. Z Hu et al [135]. At 300 K and 205 K, the reflectivity increases as the frequency decreases, indicating a metallic response of the material [135, 161].

The opening of a SDW gap is observed at 160 K as a drastic suppression of reflectivity in the frequency range of 600–1300 cm^{-1} and then a steep increase below 400 cm^{-1}. At 60 K and 10 K, the suppression in reflectivity gets more pronounced, while the low frequency ($\leq$ 400 cm^{-1}) reflectivity becomes steeper and approaches a higher level as shown in Figure 3.13 [135, 161]. This indicates that the material is still metallic and the Fermi surfaces are partially gapped and only certain parts of Brillouin zone are gapped. The effect is observed as higher electrical conductivity at zero–frequency in transport measurements as reported by K. Matsubayashi et al [29].

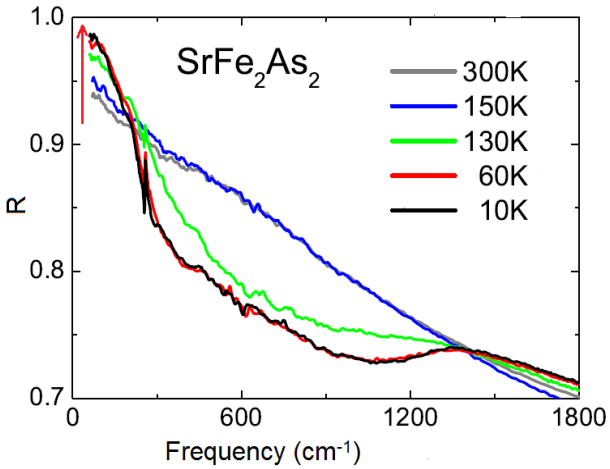

Figure 3.13. Reflectivity of $SrFe_2As_2$ at various temperatures (300–10 K) as reported by W. Z. Hu et al [135].

3.2.1. Effect of high–pressure

Recently, high–pressure infrared measurements are reported on $BaFe_2As_2$ and $SrFe_2As_2$ to address the pressure–temperature induced phase transition in SDW state [176, 174].

L. Baldassarre et al [176] reported high pressure measurement for $BaFe_2As_2$ at 300 K, 160 K and 110 K in the mid infrared range. The DAC with type IIa diamond was used with CsI as a pressure transmitting medium. Only three pressure values at 110 K were shown, i.e. 1.2 GPa, 6.6 GPa and 11.4 GPa, which showed a clear opening of the SDW gap at 1.2 GPa as a

suppression in reflectivity in the low frequency range. The SDW gap was closed when the pressure was increased to 6.6 GPa and the material showed enhanced metallicity when the pressure was further increased to 11.4 GPa.

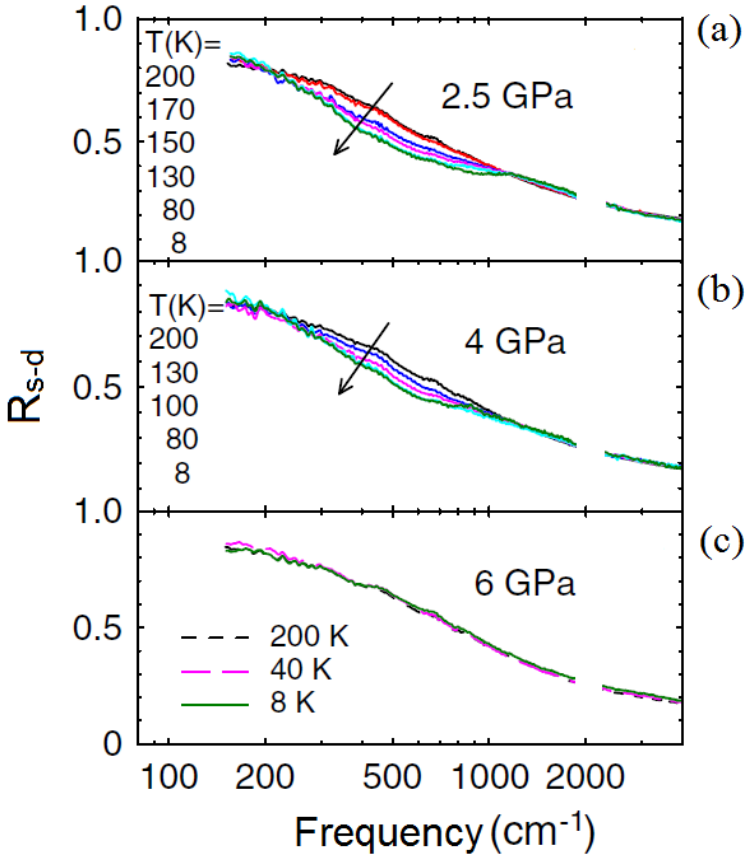

Figure 3.14. Reflectivity of $SrFe_2As_2$ under high pressure at various measured temperatures as reported by H. Okamura et al [174] (a). At 2.5 GPa, (b) 4 GPa and (c) 6 GPa. The figure is taken from-[174].

K. Ahilan et al [177] investigated the behaviour of $BaFe_2As_2$ under hydrostatic pressure up to 2.75 GPa and observed that application of pressure progressively suppresses the SDW transition temperature (T_C) to ~ 150 K. The authors concluded that there is no sign of pressure–induced superconductivity in undoped $BaFe_2As_2$ down to 1.8 K but the applied pressure can surprisingly enhance the superconducting temperature [178]. Furthermore, they [177] also observed that the effect of pressure on T_c is very small in the optimally and over–doped crystals.

Similar behaviour is also reported by Zhao et al [178] in CeFeAsO where the system is tuned from a semimetal to a high–temperature superconductor by doping the material with

fullerene. The changes of the structural lattice distortion around 155 K is due to the noticeable structural phase transition temperature, which decreases gradually with increasing fullerene concentration and disappears at certain values of fullerene doping, when superconductivity is already well developed. The author attributed the observed enhancement of the superconducting temperature (T_c) to the decrease of Fe-Fe distance that occurs upon chemical doping.

Now, H. Okamura et al [174] reported high–pressure (0–6 GPa) infrared measurement on $SrFe_2As_2$ at temperatures from 200 K down to 8 K. The DAC with type IIa diamond was used with Glycerine or Daphne oil 7474 as a pressure–transmitting media. Ruby luminescence technique was used for the pressure measurement and both pressure transmitting media show similar results.

The plots at 2.5 GPa, 4 GPa and 6 GPa are shown in Figure 3.14. The reflectivity at 200 K shows an increasing trend with increasing pressure (see Figure 3.14 (a)), indicating a conventional metallic behaviour. The high frequency part, i.e. above 6000 cm^{-1}, shows no pressure or temperature dependence. The SDW gap shows the gradual suppression when the pressure was increased from 2.5 GPa (Figure 3.14 (a)) to 4.0 GPa (Figure 3.14 (b)) and completely closed at 6 GPa (see Figure 3.14 (c)).

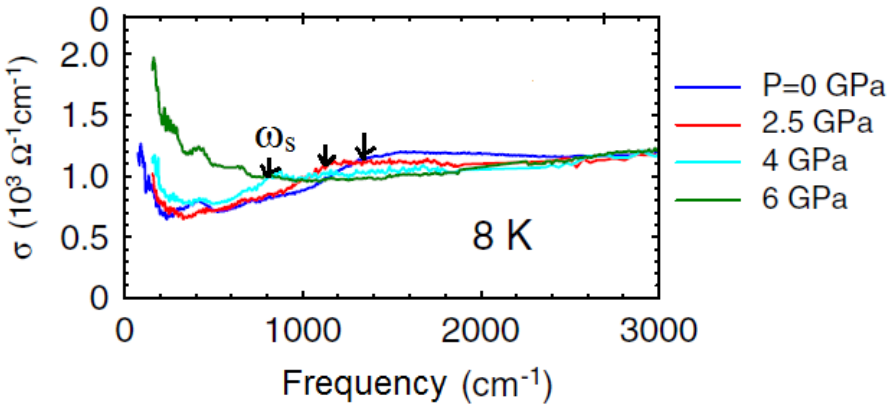

Figure 3.15. Real part of the optical ($\sigma_1(\omega)$) conductivity for $SrFe_2As_2$ at 8 K as reported by H. Okamura et al [174] (a). The shoulder frequency (ω_s) is shown with black arrows. The figure is taken from [174].

L. Badassarre et al [176] extract the real part of the optical conductivity by fitting the reflectivity with a Lorentz–Drude model according to the approach by S. J. Moon et al [142] for sample–diamond interface. The authors [176] perform a spectral weight analysis by using

the fitting contributions and calculate the degree of electronic correlations which will be discussed in section 3.5.

H. Okamura et al [174] extract the real part of optical conductivity by using the modified Kramers–Kronig analysis [175] for sample–diamond interface. The extracted real part of optical conductivity at 8 K for various pressures is shown in Figure 3.15. It shows a depletion in the optical conductivity which appears as a gap like structure relating to the formation of the SDW gap. As the pressure increased to 6 GPa, the depletion in optical conductivity is suppressed and $SrFe_2As_2$ exhibits conventional metallic response.

H. Okamura et al [174] marked that frequency where the depletion in optical conductivity started as a shoulder frequency (ω_s) as shown with arrows in Figure 3.15. The authors [174] plotted ω_s in the phase diagram, where it shows similar behaviour as that of the SDW transition temperature (see Fig. 1 (b) of reference [174]).

In fact, the overall level of the optical conductivity as reported by H. Okamura et al [174] is lower by a factor of two (approximately) compared to the results reported by other groups [135, 176, 154]. The reason is not clear yet even though the quality of crystals were similar to the previous result as reported by W. Z. Hu et al [135]. Furthermore, they [174] used samples without any mechanical polishing and cleaved them just before each measurement. Therefore, the authors agreed to consider the importance of surface finishing for the reflectivity measurement. Beside the problem in absolute level, the spectral features are similar to the results reported by the other groups – [135, 176, 154].

3.3. Experimental results and discussion for $SrFe_2As_2$

In this part of thesis, the effect of high–pressure (0–6 GPa) was studied on the SDW state by measuring the near–normal incident reflectivity for a single crystal of $SrFe_2As_2$ at temperature from 300 K down to 10 K, in the far and mid–infrared ranges. The experimental results and discussions will be presented in this section.

3.3.1. Pressure cycles

The reflectivity (R_{s-d}) of $SrFe_2As_2$ in the far and mid–infrared frequency range is shown in Figure 3.16 at 1.0 GPa for various measured temperatures (300–10 K). The diamond multi–phonon absorption around 2000 cm^{-1} is cut from the spectra. The reflectivity above 3000 cm^{-1} shows almost no dependence on temperature or pressure.

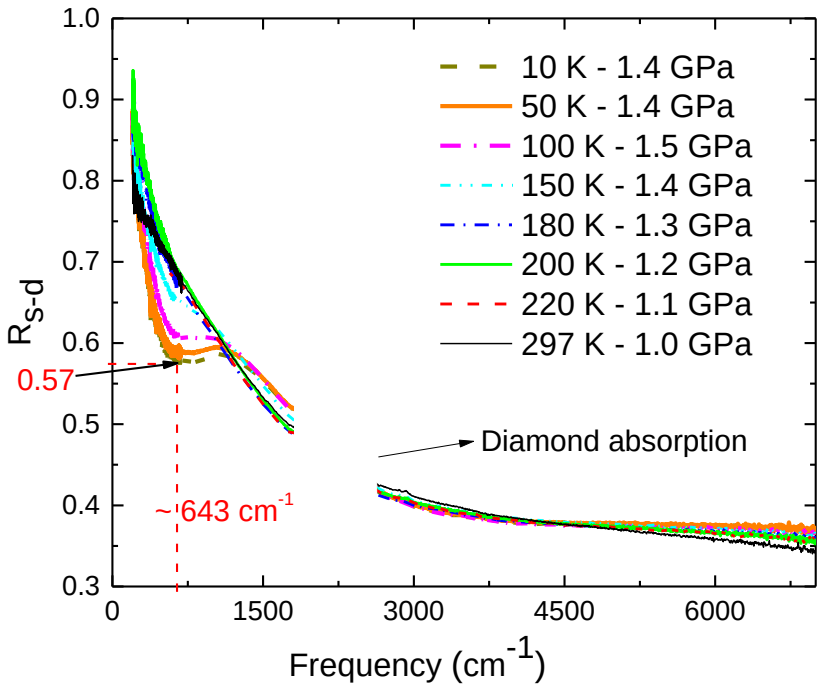

Figure 3.16. Frequency–dependent reflectivity (R_{s-d}) of $SrFe_2As_2$ at 1.0 GPa, in the far and mid infrared frequency range measured at various temperatures. The diamond multi–phonon absorption around 2000 cm^{-1} is cut from the spectra.

In Figure 3.17 (a), the enlarged view of Figure 3.16 is shown in the low frequency range, 200–1900 cm^{-1} at 297 K, 220 K, 200 K and 180 K. The reflectivity at 297 K and 220 K shows conventional metallic response while at 200 K and 180 K, the reflectivity shows a

slight change in slope below 400 cm^{-1}, which approaches an absolute level of 0.88 at 200 cm^{-1}. The effect can be more clearly observed in Figure 3.24, where the effect of pressure is shown explicitly at 200 K as described in section 3.3.2.

In Figure 3.17 (b) the enlarged view of the Figure 3.16 is shown in the low frequency range at 180 K, 150 K, 100 K, 50 K and 10 K. The reflectivity at 150 K shows a clear suppression in the range of 500–800 cm^{-1}. The suppression in reflectivity increased with decrease in temperature. For instance, the absolute level of reflectivity at 643 cm^{-1} and 150 K is around 0.65, which decreases to 0.60 at 100 K and 0.57 at 10 K. In addition, the reflectivity shows a steep increase like a Drude tail below 500 cm^{-1} as shown with a blue dashed arrow in Figure 3.17 (b) which is a clear indication of the formation of SDW gap as reported by W. Z. Hu et al [135] and H. Okamura [174] (see section 3.2).

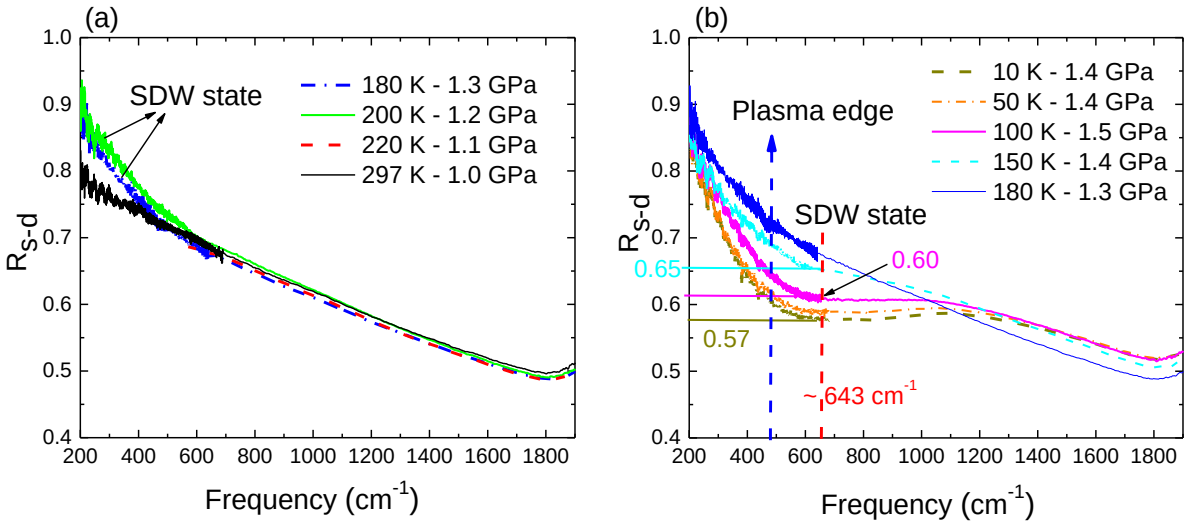

Figure 3.17. Enlarged view of Figure 3.16 shows the reflectivity of $SrFe_2As_2$ in low frequency range, 200–1200 cm^{-1}. (a) At 297 K, 220 K, 200 K and 180 K. (b) At 180 K, 150 K, 100 K, 50 K and 10 K.

In Figure 3.18 (a) the reflectivity (R_{s-d}) of $SrFe_2As_2$ is shown at 2.2 GPa for various temperatures (300–10 K). The high frequency part, i.e. above 3000 cm^{-1} does not depend on pressure or temperature. The enlarged view of the low frequency regime is shown in Figure 3.18 (b). The absolute level of reflectivity at 643 cm^{-1} increased to 0.61 at 10 K. Similarly, at 100 K and 150 K the absolute level of reflectivity increased to 0.66 and 0.70 respectively. This shows that the increase in pressure leads to progressive suppression of the SDW gap as observed by H. Okamura et al [174] recently (see section 3.2.1).

In Figure 3.19 (a) the reflectivity (R_{s-d}) is shown, at 3.7 GPa in far and mid–infrared range. The increase of pressure shows an almost negligible effect at the high frequency part, i.e. above 3000 cm^{-1}. In Figure 3.19 (b), the reflectivity at all temperatures shows conventional metallic behaviour except 50 K and 10 K. The reflectivity at 10 K shows a small SDW gap, while at 50 K the gap is near to close. The criteria for distinguishing the SDW and Suppressed SDW states will be described in section 3.3.4.

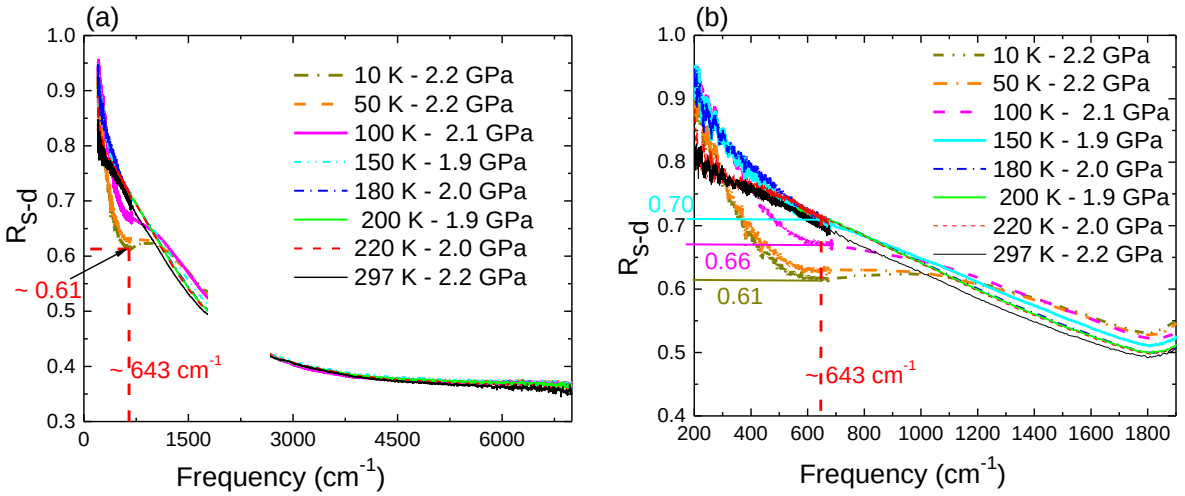

Figure 3.18. Reflectivity (R_{s-d}) of $SrFe_2As_2$ at 2.2 GPa, in the far and mid–infrared frequency range. (b) Enlarged view of the left panel in the low frequency range, 200–1200 cm^{-1}.

In Figure 3.20 (a) the reflectivity (R_{s-d}) at 4.0 GPa is shown, where the high frequency part, i.e. above 3000 cm^{-1}, still shows negligible changes. In the low frequency part (see Figure 3.20 (b)) the SDW gap is suppressed for all temperatures, and the $SrFe_2As_2$ shows a conventional metallic reflectivity. This shows that the SDW gap is completely suppressed at ~ 4.5 GPa at 10 K. The value is in good agreement with the electrical transport measurements as reported by Matsubayashi et al [29] and Kobayashi et al [129]. In fact, Okamura et al [174] shows a complete suppression of the SDW gap at around 6 GPa, but their intermediate pressures between 4 and 6 GPa are not shown. In addition, they used glycerine or Daphne 7474 as pressure transmitting media.

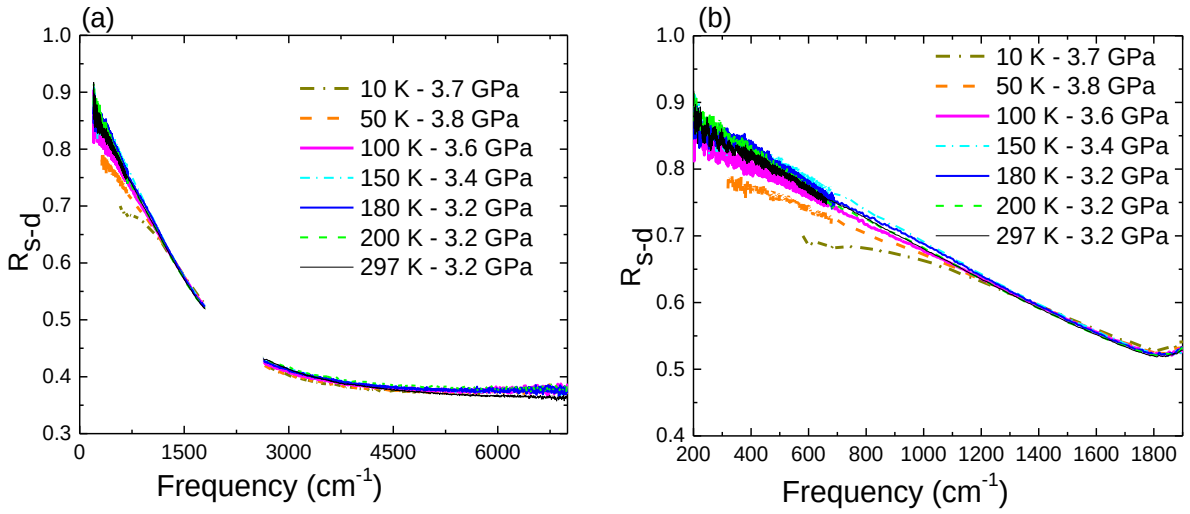

Figure 3.19. Reflectivity (R_{s-d}) of $SrFe_2As_2$ at 3.7 GPa, in the far and mid–infrared frequency range. (b) Enlarged view of the left panel in the low frequency range, 200–1200 cm^{-1}.

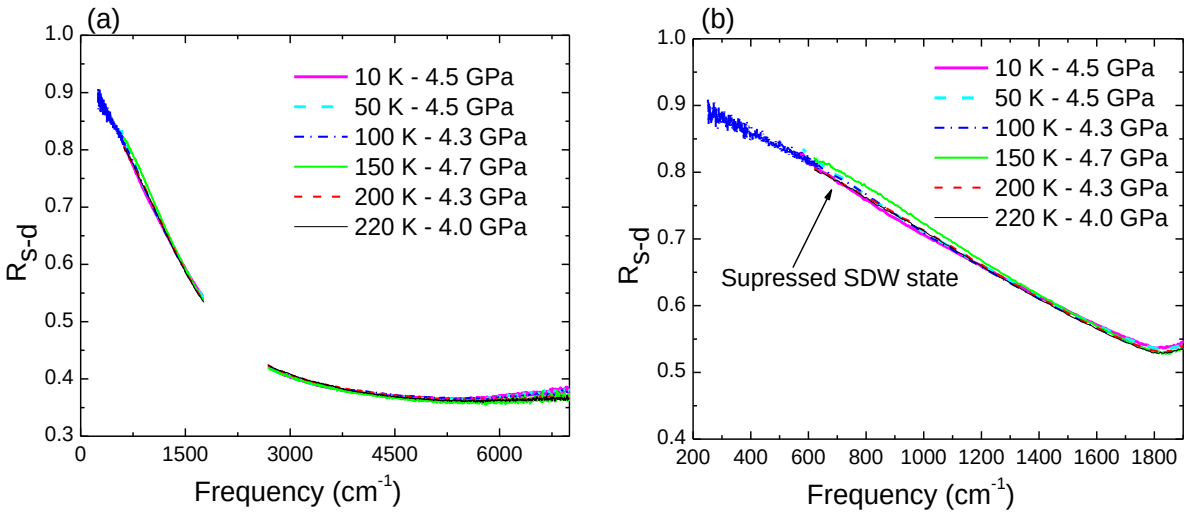

Figure 3.20. Reflectivity (R_{s-d}) of $SrFe_2As_2$ at 4.5 GPa, in the far and mid–infrared frequency range. (b) Enlarged view of the left panel in the low frequency range, 200–1200 cm^{-1}.

To check the reversibility of the transitions, two releasing pressure cycles were measured; one at 2.4 GPa (Figure 3.21) and another at 1.3 GPa (Figure 3.22). The pressure was

released slowly in small steps after the high–pressure cycles, in order to avoid any leakage in the gasket.

The first releasing cycle is shown in Figure 3.21, which shows the reflectivity of $SrFe_2As_2$ at 2.4 GPa for various measured temperatures. The freshly measured spectra are also shown with dashed–lines for the closest *P*, *T* values. The spectrum at "50 K – 2.9 GPa" (blue–colour) shows a small suppression in reflectivity, which gets more pronounced for the spectrum at "10 K – 2.9 GPa" (cyan colour).

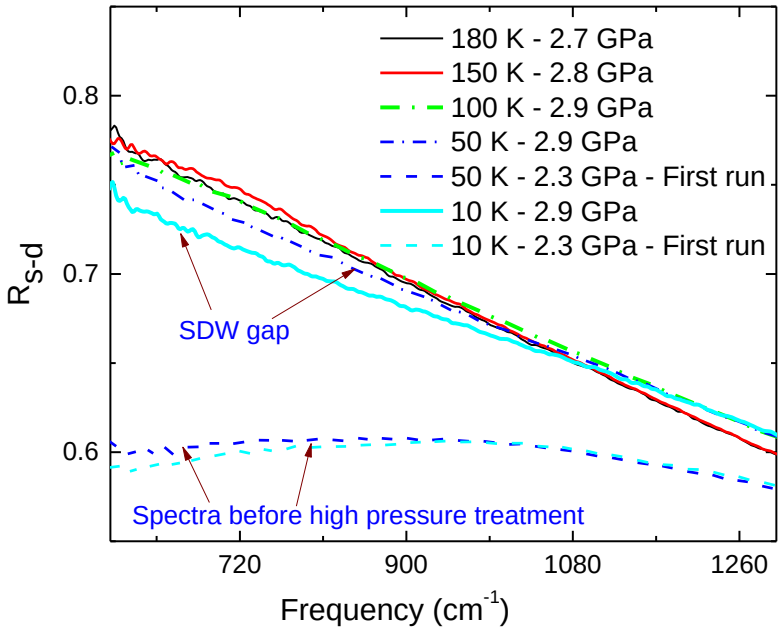

Figure 3.21. Reflectivity of $SrFe_2As_2$ for the first releasing pressure cycle at 2.4 GPa. The spectra shown as "first run" is taken from the fresh measured spectra, with the closest P, T values (represented by dashed lines).

The second releasing cycle is shown in Figure 3.22, where the level of reflectivity at "10 K – 1.4 GPa" and "100 K – 1.5 GPa" is suppressed to 0.64 and 0.66. In addition, the suppression in reflectivity at "150 K – 1.4 GPa" spectrum is also obvious. Thus, the suppression in reflectivity can be taken as an evidence for the reopening of the SDW gap once the high–pressure was released.

The reversibility of the SDW gap in the first releasing cycle is smaller than in the second releasing cycle. For instance, for the first releasing cycle (Figure 3.21) the level of reflectivity at "10 K – 2.9 GPa" spectrum is 0.74; while for "10 K – 2.3 GPa – First run" spectrum, it is 0.59, before high–pressure treatment. The difference in reflectivity level at 10

K is 0.15 for the first releasing cycle (Figure 3.21), which is decreased to 0.6 (Figure 3.22) in the second releasing cycle. This indicates that, the reversibility of the SDW transition increases with decrease in "releasing pressure".

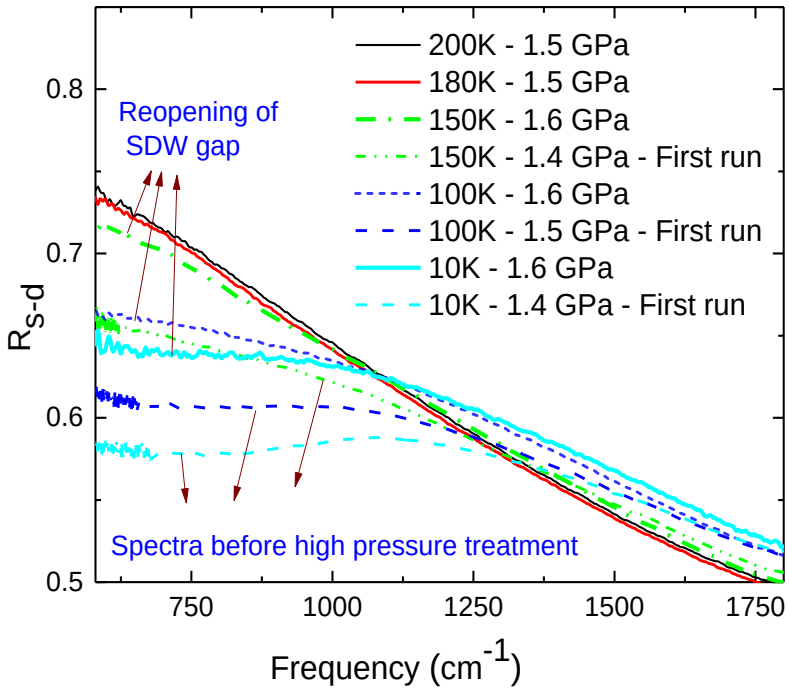

Figure 3.22. Reflectivity for $SrFe_2As_2$ the first releasing pressure cycle at 1.3 GPa. The spectra represented as "first run" is taken from the fresh measured spectra, with the closest P, T values (represented by dashed lines).

As described in section 3.1.1, in the SDW state $SrFe_2As_2$ undergoes structural and magnetic transitions, which are reported as weak first order by Y. Zhong et al [115]. The transition becomes strong first order if Sr is replaced with Ca. However, $CaFe_2As_2$ undergoes a different nature of transition compare to other AFe_2As_2 compounds, i.e. it undergoes from magnetic–orthorhombic to non magnetic collapsed–tetragonal phase transitions, under high–pressure and low–temperature [34, 116 - 120].

In fact, the situation is not clear yet and there is long debate about the order and the nature of transitions in AFe_2As_2 systems. The structural and magnetic transitions occur at the same temperatures [115, 159] for $SrFe_2As_2$ and $BaFe_2As_2$. Therefore, there can be a possibility that the structural distortion leads to the antiferromagnetic alignment of iron spins. But this

reasoning gets weakened and more ambiguous in case of $CaFe_2As_2$, where the material undergoes a phase transition from magnetic to non–magnetic phase at low–temperature.

3.3.2. Temperature cycles

In the temperature cycles group the spectra for each temperature was separated for the various measured pressures. The plots for few temperatures are shown in the following section.

Figure 3.23 shows the frequency–dependent reflectivity at room temperature for the various measured pressures. The spectra show an increasing trend with decreasing frequency confirming the metallic response of $SrFe_2As_2$. Furthermore, the level of reflectivity increases with increasing pressure, which shows an increased metallicity of $SrFe_2As_2$ with application of high pressure. This shows complete agreement with the results as reported by L. Baldassarre et al [176] recently (see section 3.2.1).

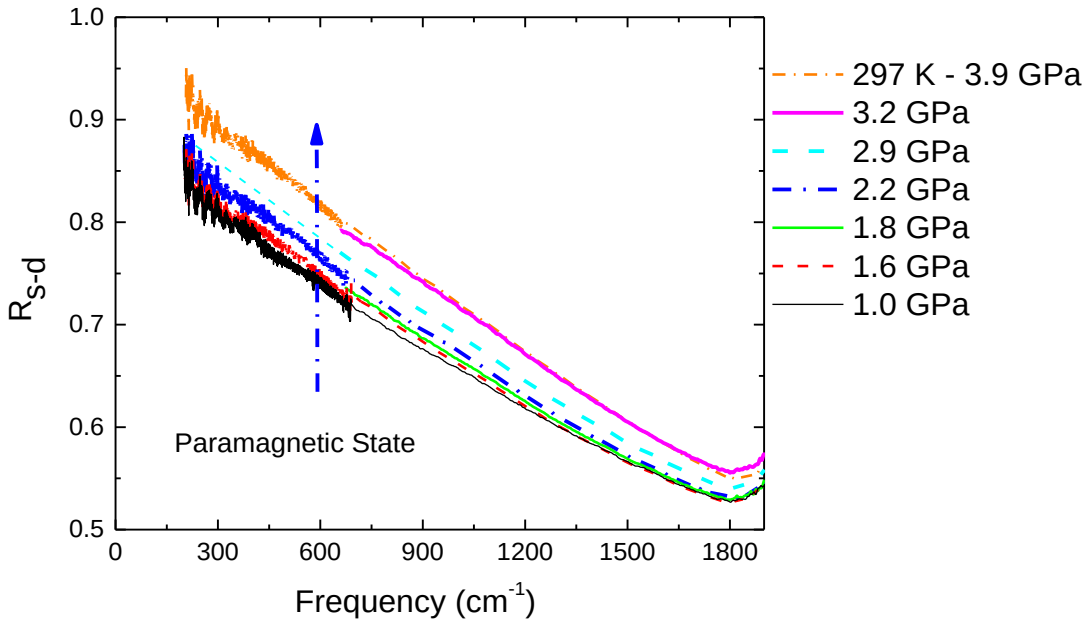

Figure 3.23. Temperature cycle at 297 K for $SrFe_2As_2$ shows the reflectivity at various measured pressures in low frequency regime.

In Figure 3.24 the reflectivity at 200 K is shown for the various measured pressures. The reflectivity at 1.2 GPa and 1.5 GPa shows a sharp increase in the slope below 400 cm^{-1} which can be easily distinguished from other high–pressure spectra. For pressures ≥ 1.7 GPa the

reflectivity exhibits conventional metallic behaviour, which shows an increase in reflectivity level as the pressure increases. The analytical details regarding the quantitative extraction of the SDW gap will be described in section 3.3.4.

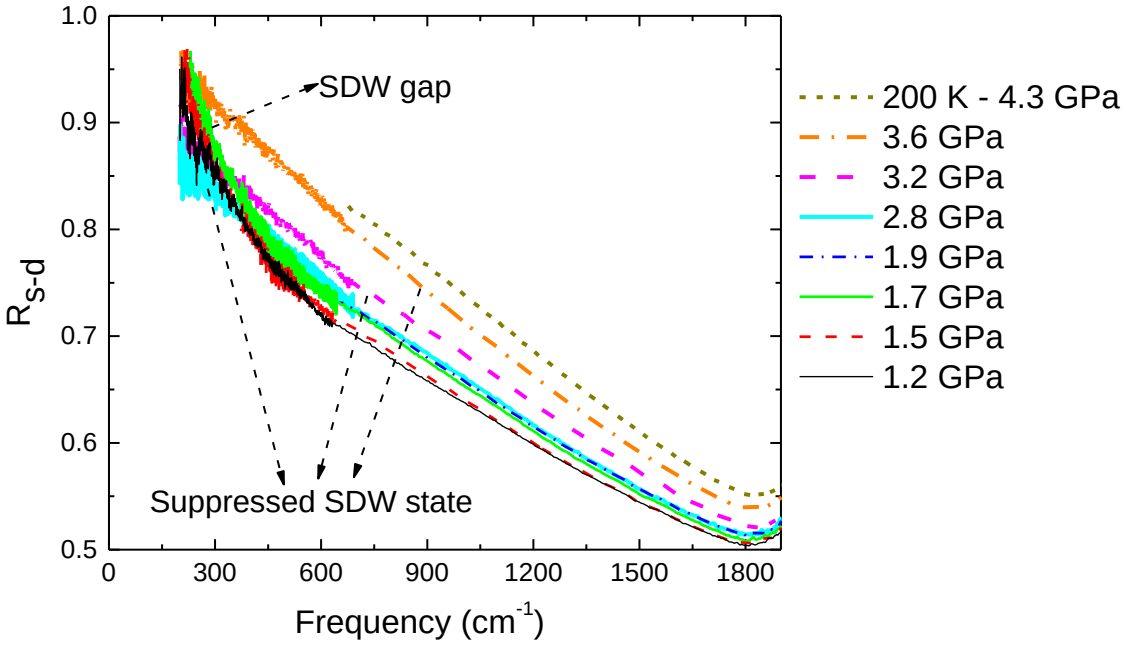

Figure 3.24. Temperature cycle at 200 K for $SrFe_2As_2$ shows the reflectivity at various measured pressures in low frequency regime.

The existence of SWD gap at "200 K – 1.5 GPa" for $SrFe_2As_2$ shows remarkable consistency of the measured LTHP data with earlier measurements at ambient pressure as reported by W. Z. Hu et al [135] and D. Wu et al [154]. In fact, Ba, Sr or Eu appear as insulating atomic sheets, which separate Fe–As conducting layers, but T_{SDW} (SDW transition temperature) changes significantly, when Sr is replaced by Ba or Eu, for example the SDW gap opened for $BaFe_2As_2$ at 140 K, and at 190 K for $EuFe_2As_2$ [150, 151, 152, 154].

Furthermore, the magnetic ordering in $EuFe_2As_2$, related to Eu^{+2} ions is observed explicitly at 19 K, which indicates that there is no magnetic interaction between Fe and Eu ions. Therefore, the change in T_{SDW} due to the change of various ions might be linked with some other phenomena which may need further investigations [150, 151, 152, 154].

In Figure 3.25 the reflectivity at 100 K is shown for the various measured pressures. At 1.4 GPa, the $SrFe_2As_2$ shows a drastic suppression in reflectivity in the range 600–1200 cm^{-1} and then a steep increase below 600 cm^{-1}, which indicates the formation of a SDW gap. The

suppression in reflectivity decreases with increasing pressure and at 3.6 GPa, it shows conventional metallic behaviour which corresponds to the suppressed SDW state. Upon further increase in pressure only the reflectivity level of the spectra is increased.

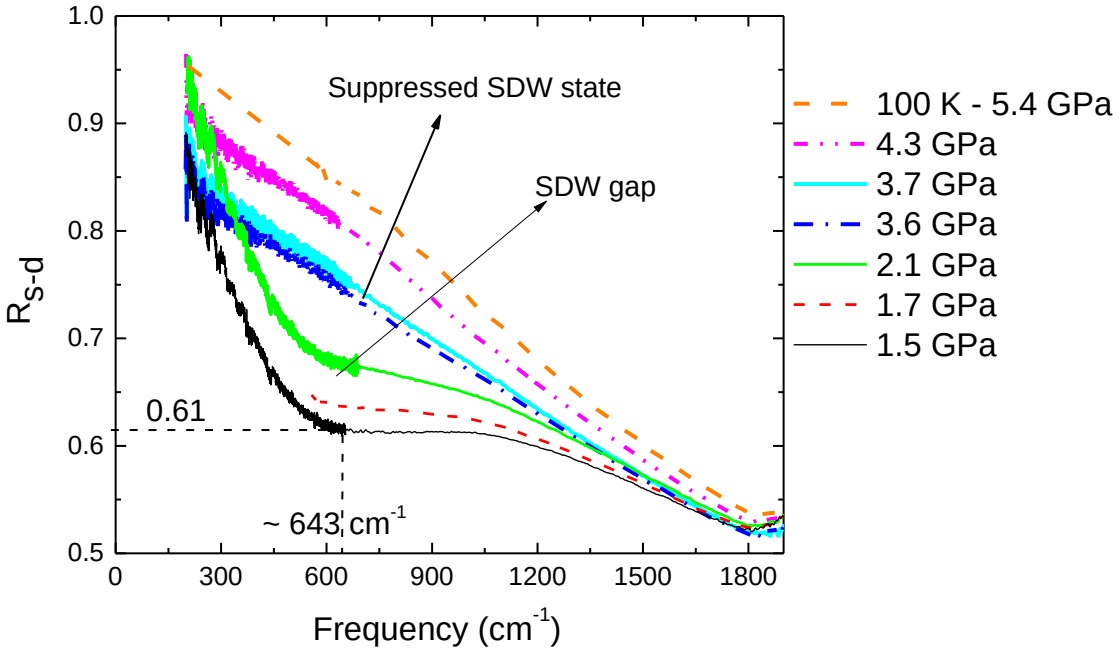

Figure 3.25. Temperature cycle at 100 K for $SrFe_2As_2$ shows the reflectivity at various measured pressures in low frequency regime.

In Figure 3.26 the reflectivity at the lowest measured temperature, i.e. 10 K is shown for various measured pressures. The absolute level of reflectivity at 643 cm^{-1} is 0.57 at 1.4 GPa, which is lower than the absolute level of 0.61 for the spectrum at "100 K - 1.5 GPa", (see Figure 3.25). This indicates that the suppression in reflectivity level increases with decreasing temperature. Furthermore, the SDW gap is completely suppressed at pressure ≥ 4.5 GPa. For the pressure ≥ 3.7 GPa, the far–infrared extrapolation were obtained by using Lorentz–Drude fits as described in section 3.3.3.

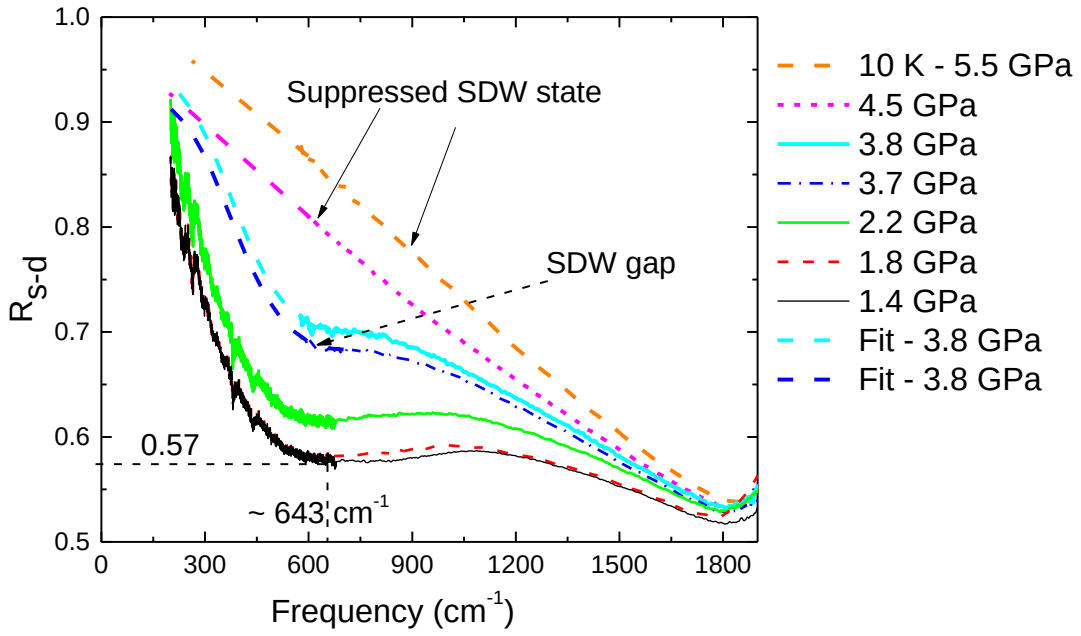

Figure 3.26. Temperature cycle at 10 K for $SrFe_2As_2$ shows the reflectivity at various measured pressures in low frequency regime.

3.3.3. Analysis and interpretation of $SrFe_2As_2$ results

The Lorentz–Drude model [8] was used to fit the reflectivity spectra as explained in sections 2.4 and 3.1.2. The frequency range from 7,000–100,000 cm^{-1} was extracted from the reference–[135] and merged with the measured LTHP spectra as shown in Figure 3.27 . The pressure–dependent electrical conductivity values (σ_{dc}) were extracted from the electrical transport measurements as reported by K. Matsubayashi et al [29].

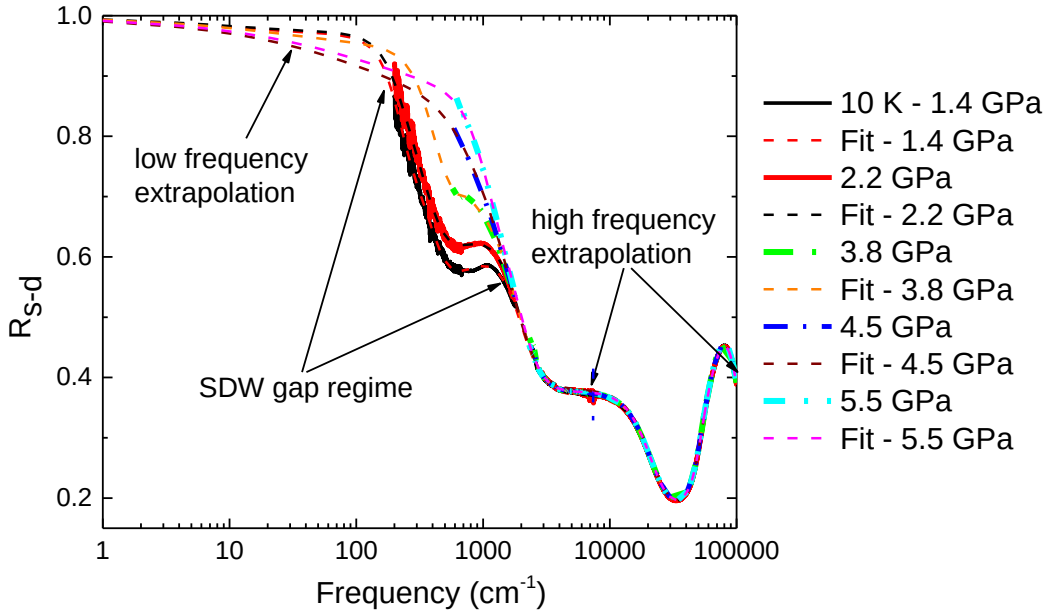

Figure 3.27. Fitting curves (dashed lines) with the measured reflectivity (R_{s-d}) spectra (solid lines) at 10 K for $SrFe_2As_2$ along with the high and low frequency extrapolations, in logarithmic scale.

W. Z Hu et al [135] fitted the temperature–dependent reflectivity data with a single Drude component and one harmonic oscillator in the paramagnetic state. For the SDW state two harmonic oscillators together with a sharp Drude peak were used to fit the data.

Later on, S. J. Moon et al [142] suggested to fit the data with two Drude terms, together with one harmonic oscillator in the paramagnetic state, in order to extract the contributions due to the electrons and holes. The hole conductivity is supposed to be incoherent and temperature independent. The approach is also adopted by D. Wu et al [154], A. Lucarelli et al [170] and L. Baldassarre et al [176] for their reflectivity data, while H. Okamura et al [174] used modified Kramers–Kronig analysis [175] for their pressure–dependent data as explained in section 3.2.1.

In principle, the optical data can be fitted with one or two Drude terms, together with at least one harmonic oscillator in the paramagnetic state and two in the SDW state. It is not possible to fit the data only with the one or two Drude terms without any harmonic oscillator.

Eq. (2.26) as described in section 2.4 was used to model the reflectivity ($R_{s\text{-}d}$) at "10 K - 1.4 GPa" as shown in Figure 3.27, along with high and low frequency extrapolations. The enlarged view in the low frequency regime is shown in Figure 3.28 in linear scale. Three harmonic oscillators *L1*, *L2* and *L3* were used to fit the high frequency region; whereas one sharp Drude (*D2*) component and two harmonic oscillators (*L4*, *L5*) were used to fit the SDW gap regime.

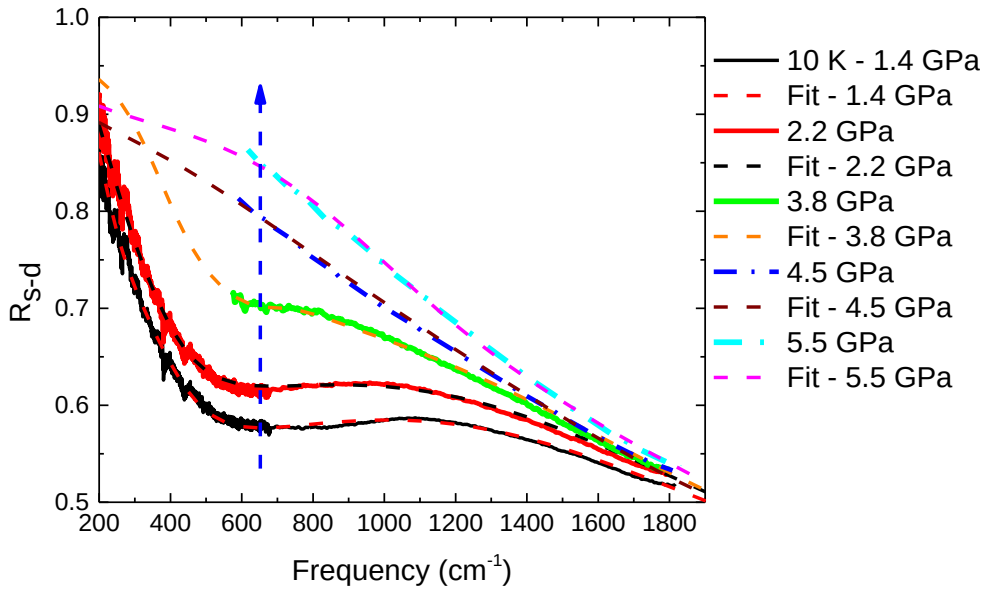

Figure 3.28. Enlarged view of Figure 3.27 in low frequency regime 200–1900 cm^{-1} in linear scale.

The fitting model was kept constant for all higher–pressures and temperatures while only *L4*, *L5* and *D2* were changed in order to fit the spectra. The room temperature fitting was done with one broad (*D1*) and one sharp (*D2*) Drude component along with one harmonic oscillator *L4*; while the remaining fitting components, i.e. *L1*, *L2*, *L3* were kept constant for all higher pressures.

The calculated real part of the optical conductivity ($\sigma_1(\omega)$) at 10 K for various measured pressures is shown in Figure 3.29. A quick glance at Figure 3.28 and Figure 3.29 shows that the material under pressure behaves similar to the case of low temperature and ambient

pressure studies. The highest pressure at 10 K corresponds to the spectrum at room temperature and with decrease in pressure the SDW gap starts to appear more clearly.

Furthermore, the shoulder frequency (ω_s) which defines the starting point of the depletion in optical conductivity as explained in section 3.2.1, shows a shift towards lower frequencies and becomes completely flat for pressures ≥ 4.5 GPa. The calculated shoulder frequency (ω_s) at 10 K for the various pressures is plotted in Figure 3.30 along with the extracted values from Okamura et al [174] at 8 K. The frequency is progressively decreasing with increasing pressures which is in agreement with the recent results reported by H. Okamura et al [174].

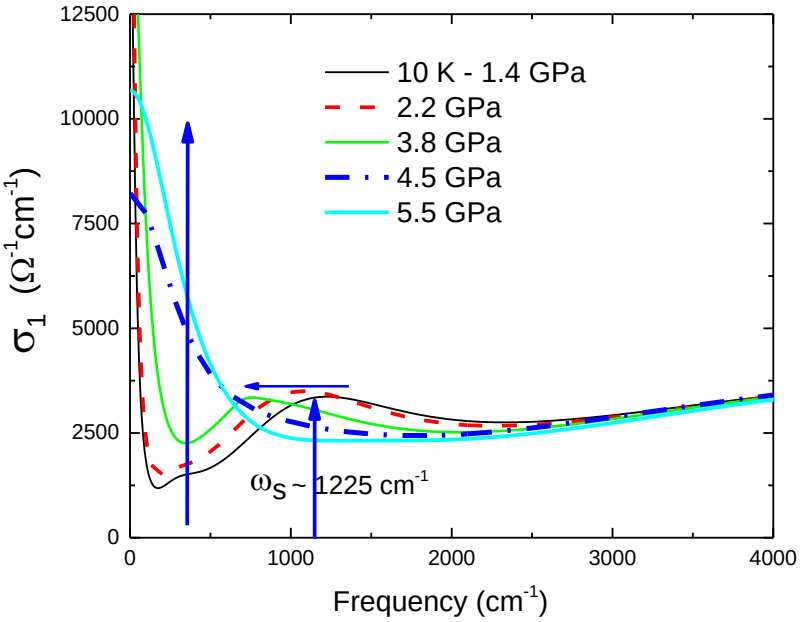

Figure 3.29. Frequency–dependent of the real part of optical conductivity ($\sigma_1(\omega)$) for $SrFe_2As_2$ at 10 K for the various measured pressures.

In Figure 3.31, the real part of optical conductivity ($\sigma_1(\omega)$) along with fitting contributions in the low frequency regime is shown for some selected pressures. At 1.4 GPa and 2.2 GPa, $\sigma_1(\omega)$ shows two peaks relating to *L*5 and *L*4 as shown in Figure 3.31 (a and b), which indicates the multiband nature of $SrFe_2As_2$.

The two peak feature is also observed by S. J. Moon et al [142] and W. Z. Hu et al [135] for $BaFe_2As_2$ and $EuFe_2As_2$ compounds. However, the ambiguity regarding its similarity with a s–wave superconducting gap was distinguished by their different coherent factors which is explained in detail by L. Degiorgi [38] and V. Vescoli [39] et al in case of one dimensional organic $(TMTSF)_2$ X superconductors [161, 135].

In Figure 3.31 (c) $\sigma_1(\omega)$ in the suppressed SDW state at 4.5 GPa is shown along with fitting contributions, where *L*5 is completely diminished and *D2* gets broadened. The peak *L4* is strongly suppressed in comparison to the SDW state (see Figure 3.31 (a and b)). As the pressure increases to 5.5 GPa as shown in Figure 3.31 (d) the suppression of *L4* is increased, while D2 gets broadened.

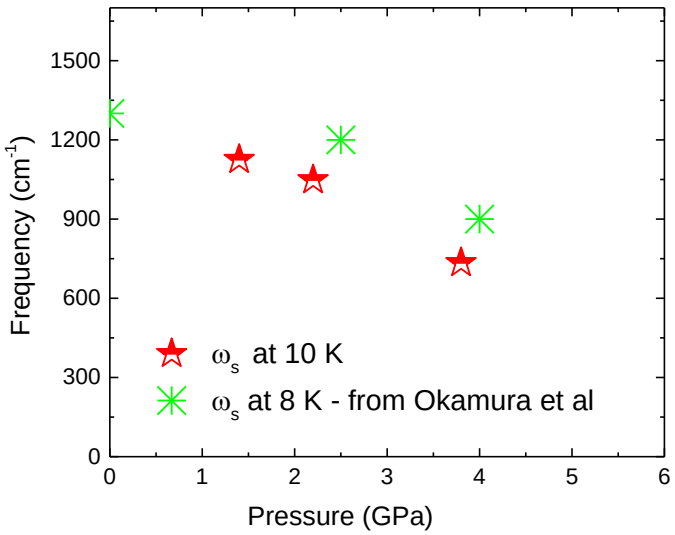

Figure 3.30. Shoulder frequency (ω_s) as function of pressure at 10 K, along with the extracted values from H. Okamura et al [174] at 8 K.

According to the band structure calculations reported by S. J. Moon et al [142], the peak *L5* (α) is formed due to the joint contributions coming from the two parallel bands, i.e. d_{yz} (spin–up) and d_{xz} (spin–up). In ambient pressure studies, *L5* is unaffected due to the, "same spin orbital" and "same spin sub–lattice", because of the exchange splitting which turns out as an itinerant nature of the SDW gap with a mean field BCS type of character. Furthermore, the authors concluded that the peak *L4* (β) is formed due to the joint contribution of the majority unoccupied d_{xz} (spin–down) orbital at one Fe atom, and minority unoccupied d_{xy} (spin–down) orbital at the adjacent Fe atom. The direction of longer and shorter Fe–Fe bonds is in the direction of *x* and *y* axis. The peak *L5* is sensitive to the long range magnetic ordering while *L4* is less sensitive and connected to the local magnetic moments for the Fe ions [142].

The calculation reported by D. Hsieh et al [146] and T. Shimojima et al [153], attributed *L5* to the non–nested bands which become partially gapped due to the opening of SDW gap; while *L4* is attributed to the nested bands which were completely gapped and found in both the paramagnetic and the suppressed SDW states.

In addition, the band structure calculations for $EuFe_2As_2$ by Jeevan et al [150] and Moon et al [142] shows that the exchange splitting of the Fe–d_{xz} band into spin–up and spin–down bands create an energy difference of around 1 eV; which appears as a major magnetic–interaction for driving SDW transition. In fact, there is only weak magnetic coupling between Eu and Fe, because of different ordering temperatures. Therefore, the SDW driving mechanism in $SrFe_2As_2$ can be considered similar to $EuFe_2As_2$.

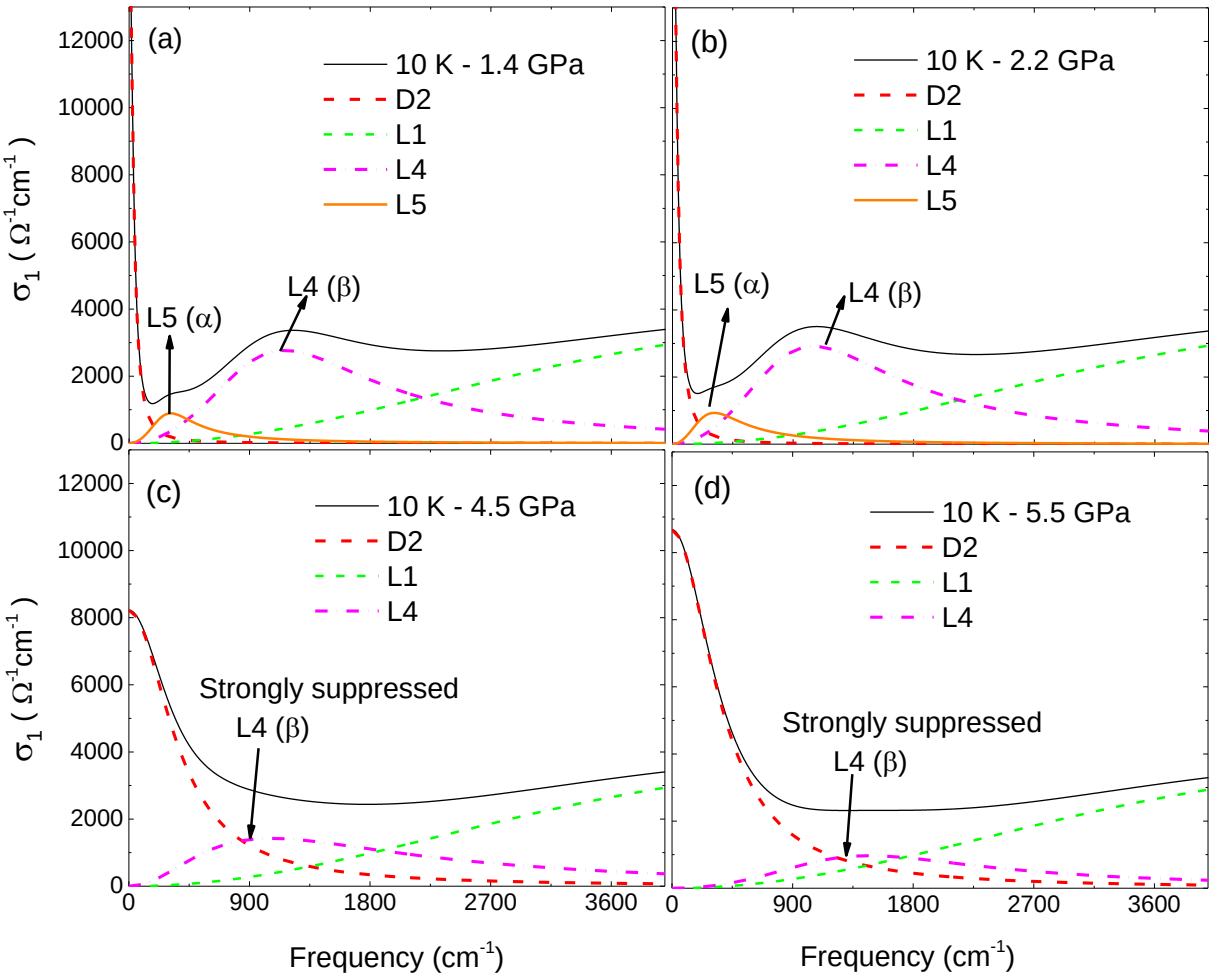

Figure 3.31. The real part of optical conductivity with fitting contributions for $SrFe_2As_2$ at 10 K. D2 is a sharp Drude term; L1, L4 and L5 are harmonic oscillators. (a) In SDW state at 1.4 GPa and (b) at 2.2 GPa. (c) In the suppressed SDW state at 4.5 GPa and (d) 5.5 GPa.

In conventional metals the spectral weight is proportional to the total number of electrons or holes (both valance and core) which contributes to the electrical transport [135, 154, 170]. However, in correlated metals the correlations affect the transport mechanism, which appears

as reshuffling of spectral weight among various fitting contributions. Mathematically, the spectral weight can be written as Eq. (3.1).

$$\text{Spectral weight}\,(\omega) = 8\int_0^{\omega_c}\sigma_1(\omega)\mathrm{d}\omega = \frac{4\pi n e^2}{m_{eff}} \qquad (3.1)$$

The selection of the cut–off frequency (ω_c) depends on the type of contribution needed to be extracted, "*n*" is the carrier density and "*e"* is the charge of the electron. Since there is no electron–phonon coupling in the SDW state, the effective mass (m_{eff}) can therefore be substituted by the band mass (m_b) [37, 135].

The spectral weight for the Drude components (*D1* and *D2*) and harmonic oscillators (*L5* and *L4*) were computed at 10 K, 100 K, 200 K and 297 K for $SrFe_2As_2$. The error bar in computations due to the fitting procedure was around 1 x 10^{-6} ohm cm^{-2}, which is in good agreement with the error bars of the calculations by S. J. Moon et al [142] (see Figure 4 of reference – [142]).

Figure 3.32 (a) shows the pressure–dependent spectral weight of *D1*, *D2* at 10 K, 100 K, 200 K and 297 K. The spectral weight of *D2* at 10 K and 100 K increased by a factor larger than two at around 4.3 GPa, which corresponds to the transition from SDW to suppressed SDW states. The broad Drude component (*D1*) only exists in the paramagnetic state, i.e. above T_{SDW}. The sum of the Drude components (*D1* + *D2*) at 297 K shows the joint contribution due to the electrons and holes in the paramagnetic phase, which linearly increases with increasing pressure.

Figure 3.32 (b) shows the temperature–dependent change in spectral weight for the sum of *D1* and *D2* at fixed pressures, i.e. within a range of +/- 0.5 GPa. The spectral weight (*D1* + *D2*) below 50 K start from ~ 1 x 10^6 ohm^{-1} cm^{-2} which increases with increasing pressure and approaches to around 6 x 10^6 ohm^{-1} cm^{-2} at 5.5 GPa. In fact, it is obvious that the increase in spectral weight decreases as the temperature increases, i.e. at 297 K the spectral weight increase from ~ 5.5 x 10^6 ohm^{-1} cm^{-2} to ~ 7.5 x 10^6 ohm^{-1} cm^{-2}. The behaviour of the spectral weight is in close agreement with the normalized spectral weight as reported by H. Okamura et al [174] recently.

Figure 3.33 (a) shows the pressure–dependent spectral weight of *L5* and *L4* at 10 K, 100 K, 200 K and 297 K for $SrFe_2As_2$. The spectral weight of the *L4* shows a huge decrease at 4.3 GPa, while *L5* completely diminishes after the suppression of the SDW gap. The spectral

weight of *L4* at 297 K shows a linear decreasing trend with increasing pressure. The temperature–dependent illustration at fixed pressure, i.e. within a range of +/- 0.5 GPa is shown in Figure 3.33 (b). It shows a considerable decrease in spectral weight at 4.5 GPa and 5.5 GPa, which corresponds to the suppressed SDW state.

N. Ni et al [180], relate the behaviour of change in spectral weight of *L4*, to the suppression of long range magnetic ordering, but with enhancement in spin fluctuation. However, A. Sacchetti et al [181] relate it to the reduced anisotropy and destruction of nesting in Fermi surfaces. Thus, in case of doping [180], the long range magnetic ordering is suppressed, while spin fluctuation gets enhanced. In contrary, the high–pressure [181] changes the crystal symmetry which results in the decrease in nesting of Fermi surfaces.

Normally, external pressure does not change the symmetry of the crystal lattice. It just reduces and may be results in deformation of the unit cell. However, the symmetry only changes in case of pressure driven structural transition, which is a case for pnictides but the change in symmetry might be a consequence not the reason for the phase transition.

Lester C. et al [171], argued in favour of a local magnetic picture, on the basis of their neutron scattering experiments which shows a decrease in ordered magnetic moments with increasing cobalt concentrations. On the other hand, W. Z. Hu et al [135], claim for the itinerant picture on the basis of their temperature–dependent reflectivity measurements, for both $SrFe_2As_2$ and $BaFe_2As_2$ compounds.

Further discussion is presented together with measured LTHP data for cobalt doped $SrFe_{1.9}Co_{0.1}As_2$ compound in section 3.4.

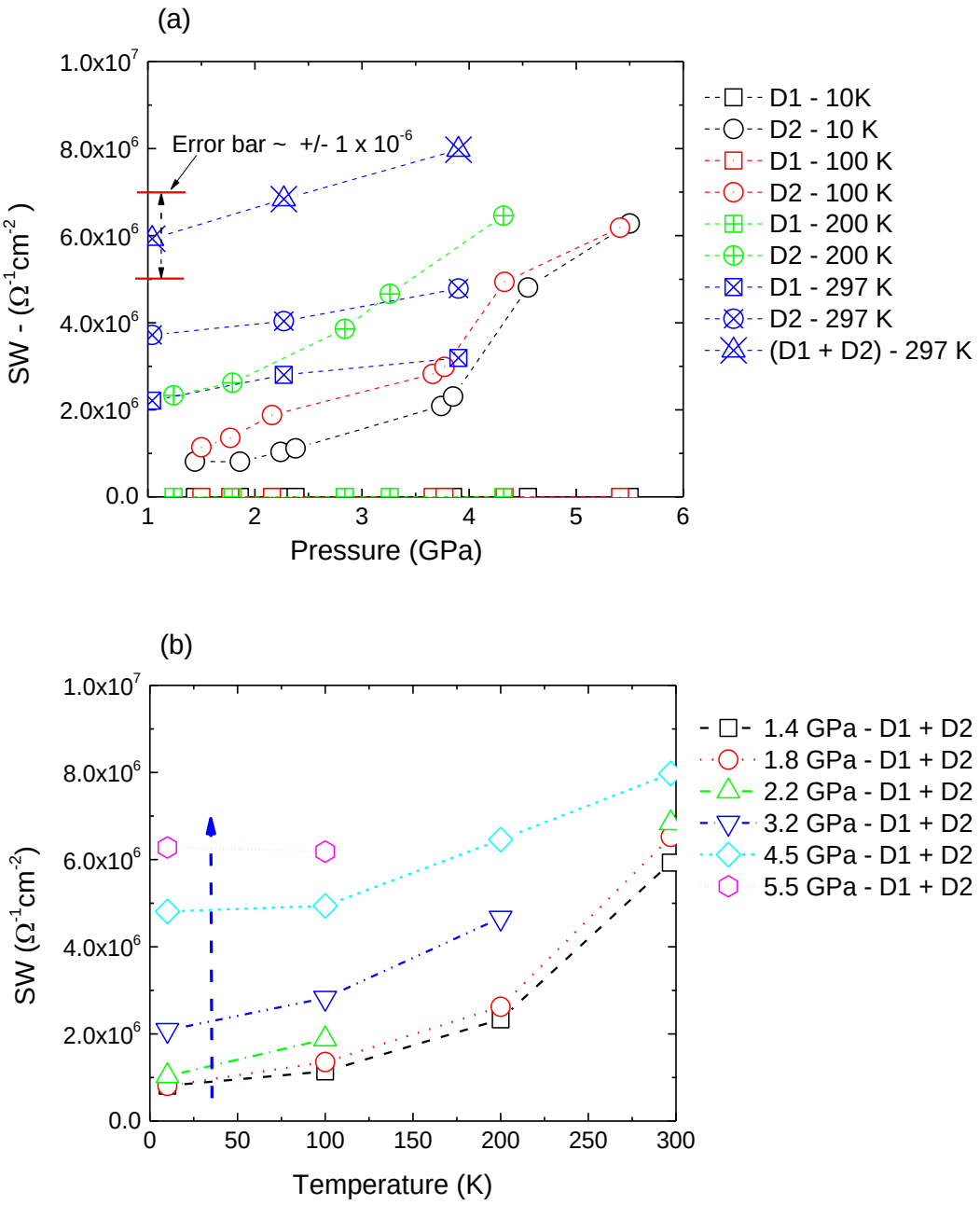

Figure 3.32. Spectral weight of the Drude components for $SrFe_2As_2$ at 10 K, 100 K, 200 K and 297 K. D1 is a broad Drude peak which exists only at 297 K and represents the hole current. D2 is a sharp Drude peak which represents the electronic current. The error bar in fitting is around +/- 1 x 10^{-6} ohm cm^{-2}, which is comparable to the error bar in S. J. Moon [142] et al, temperature–dependent calculations. (b) Temperature–dependent behaviour of spectral weight of Drude (D1 + D2) components.

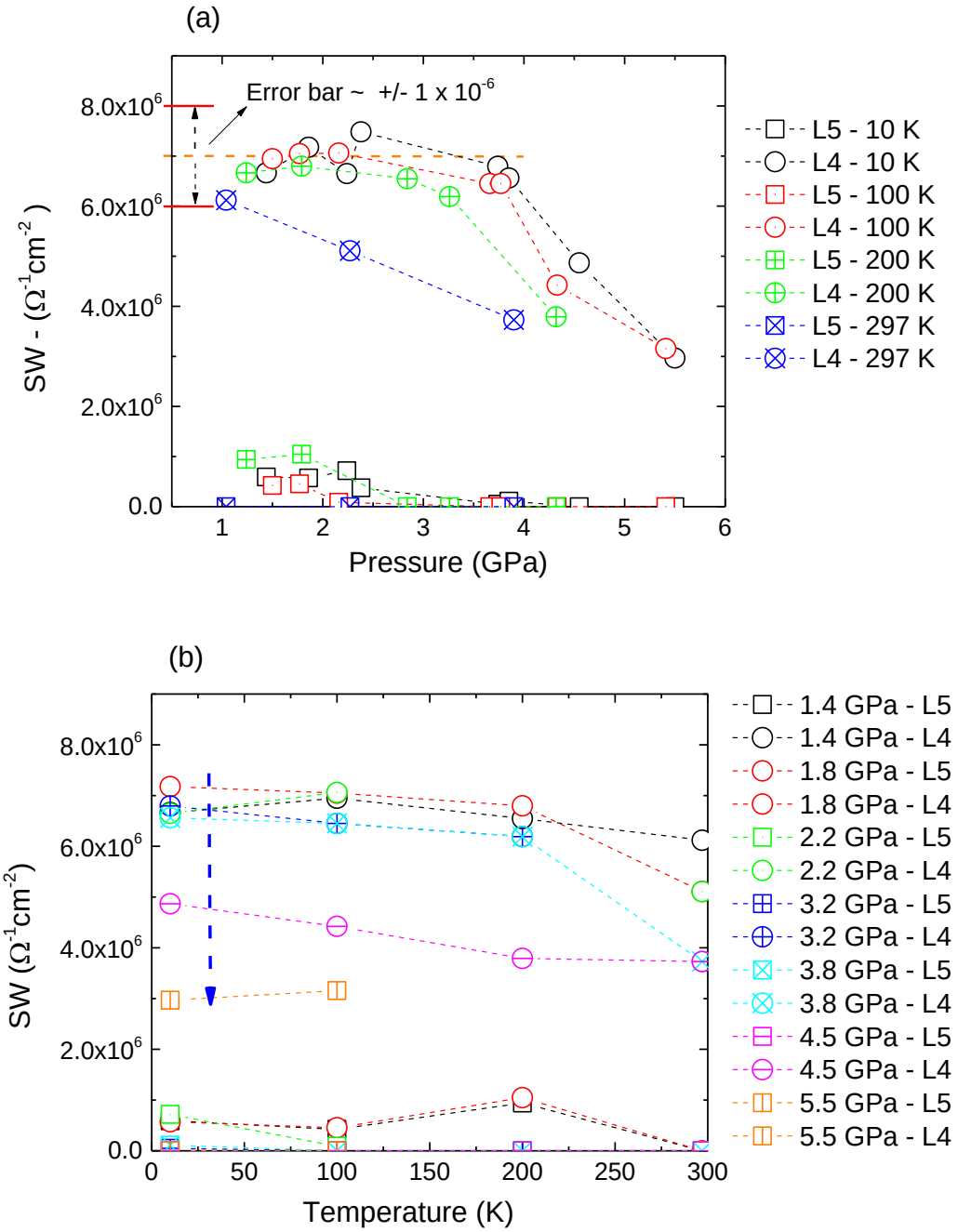

Figure 3.33. (a) Pressure–dependence of the spectral weight for L5 and L4 at 10 K, 100 K, 200 K and 297 K for $SrFe_2As_2$, where L5 is diminished after suppression of SDW gap. The error bar in fitting is around +/- 1 x 10^{-6} ohm cm^{-2}, which is comparable to the error bar in S. J. Moon et al [142], temperature–dependent calculations. (b) Temperature–dependent behaviour of the spectral weight of L4 and L5 grouped for the spectra within a range of +/- 0.5 GPa.

3.3.4. The Phase Diagram

In order to draw the pressure (*P*) – temperature (*T*) phase diagram, a quantitative method was searched for characterizing the different states of $SrFe_2As_2$.

In Figure 3.34, three different pressure were selected at 50 K, i.e. at 1.4 GPa (SDW state), 3.7 GPa (near to close SDW state) and at 3.8 GPa (suppressed SDW state). The Lorentz–Drude fits for the corresponding spectra are also shown with dashed–lines.

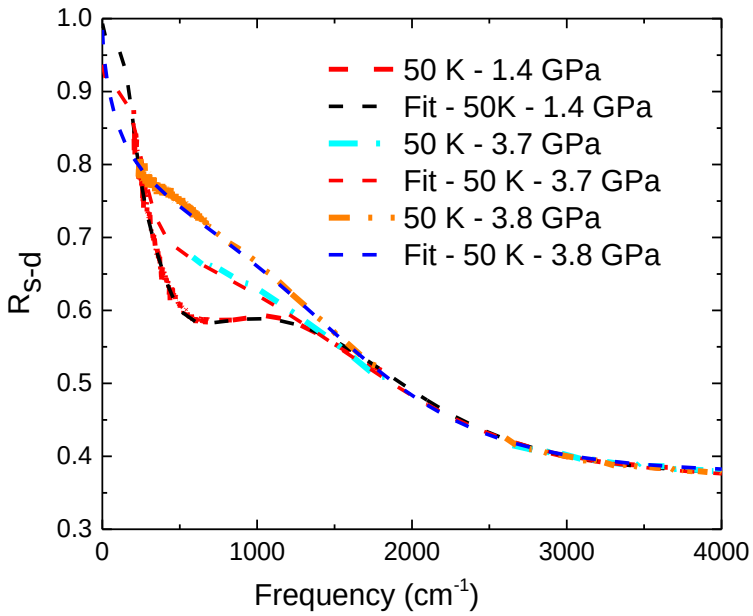

Figure 3.34. Measured data for $SrFe_2As_2$, with fitting curve at 50 K for 1.4 GPa, 3.7 GPa and 3.8 GPa.

In the first approach, two straight–lines were fitted at higher (700 cm^{-1}) and at lower frequency (350 cm^{-1}) parts of the measured data as shown in Figure 3.35. The ratio of slopes for the two fitted lines at "50 K - 1.4 GPa" is 96.5, while for the spectra at "50 K – 3.8 GPa" the ratio of slopes approaches to 1.38. Thus, for the slopes ratio (R) ≥ 2, the spectrum can be marked as SDW state, while for R $\leq$ 1.5 the spectra can be classified as paramagnetic or suppressed SDW state.

In the second approach, the first order derivative of fitting curve was taken as shown in Figure 3.36. It shows a clear peak for the spectra at "50 K - 1.4 GPa" and "50 K - 3.7 GPa", which becomes almost flat for the spectra at "50 K - 3.8 GPa" in suppressed SDW state.

The drawn phase diagram is shown in Figure 3.37, where the paramagnetic state is represented with the black squares, while red squares represent the suppressed SDW state.

The area filled with cyan colour represents the paramagnetic phase and the yellow region indicates the suppressed SDW state. The area filled with an orange colour corresponds to the SDW state, where the blue circles correspond to SDW state, while the diamond blue related to the releasing pressure values. The red stars show the suppressed SDW state for the releasing pressure.

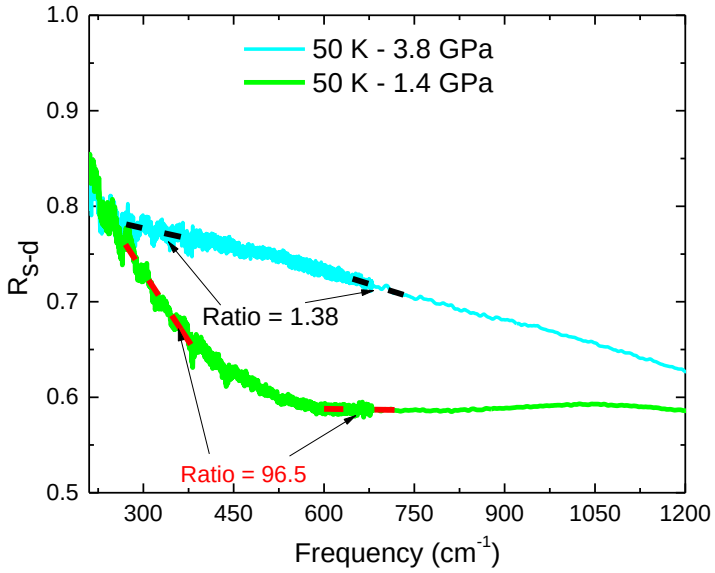

Figure 3.35. Linear fits to the measured data at two frequency regimes, i.e. at around 350 cm^{-1} and 700 cm^{-1}. The ratio of slopes (R) in SDW state is 96.5 and 1.38 in suppressed SDW state.

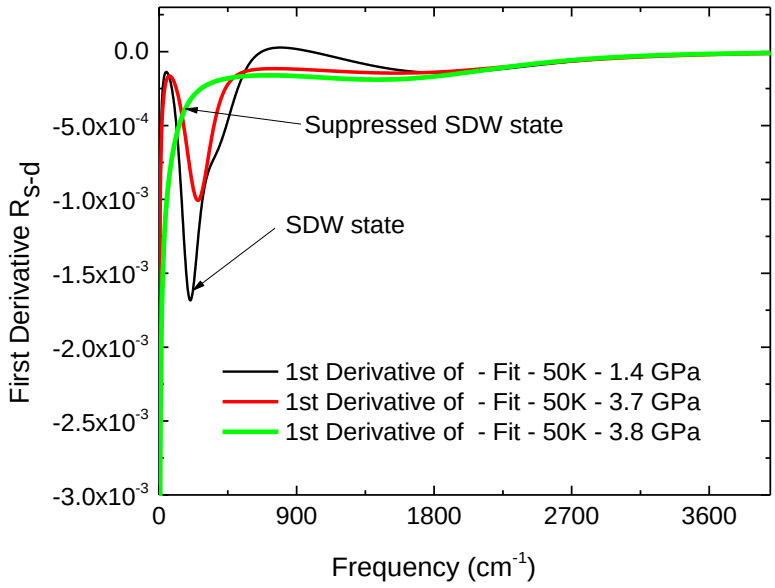

Figure 3.36. First order derivative of R_{s-d} taken for the fitting curves at 1.4 GPa (SDW state), 3.7 GPa (near to close SDW state) and 3.8 GPa (suppressed SDW state) for $SrFe_2As_2$ compound.

It can be seen in Figure 3.37 that some red stars lie inside the orange region, i.e. in the SDW phase, which indicates the irreversibility regime of $SrFe_2As_2$, back to its initial state. For the first releasing cycle (at 2.4 GPa) the SDW state was recovered only at 50 K and 10 K; while

for the second releasing cycle (at 1.3 GPa) the SDW state could not be recovered at 200 K and 180 K.

Figure 3.37 (b), shows the phase diagram drawn on the basis of the minimum pressure (P_{SDW}) required to suppress the SDW gap at the corresponding measured temperature. The *P*, *T* values are shown in the Table 3.3. It is clear from the phase diagram that higher pressures are required (P_{SDW}) to suppress the SDW state, when the material is cooled down to the low temperatures.

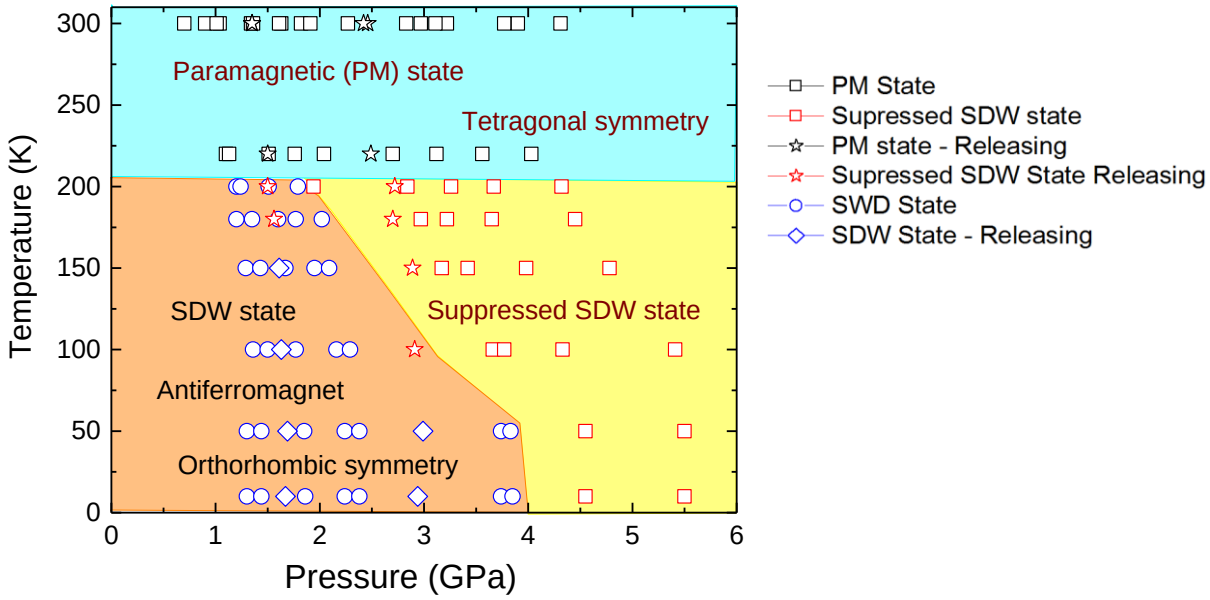

Figure 3.37. Pressure (T)–temperature (T) phase diagram for $SrFe_2As_2$ drawn by taking the first order derivative of the fitting curves for the measured P, T values. The stars represent the releasing pressure values in paramagnetic (black squares) and in suppressed SDW (red squares) states. The circles represent SDW state from the first run, while diamond corresponds to the releasing pressure values in SDW state.

The phase diagram reported by H. Kotegawa et al [30] in uniaxial configuration shows a critical pressure of around 4.4 GPa, required to suppress the SDW state for the most hydrostatic conditions (Daphne 7474)) which is in good agreement with the phase diagram drawn on the basis of LTHP measurements as shown in Figure 3.37. In addition, it is also consistent with the phase diagram drawn by K. Matsubayashi et al [127] with cubic anvil cell and glycerine as a pressure–transmitting medium as shown in Figure 3.12.

Further discussion regarding the effect of doping in combination with pressure, as measured for $SrCo_{1.9}Fe_{0.1}As_2$ will be discussed in section 3.4.

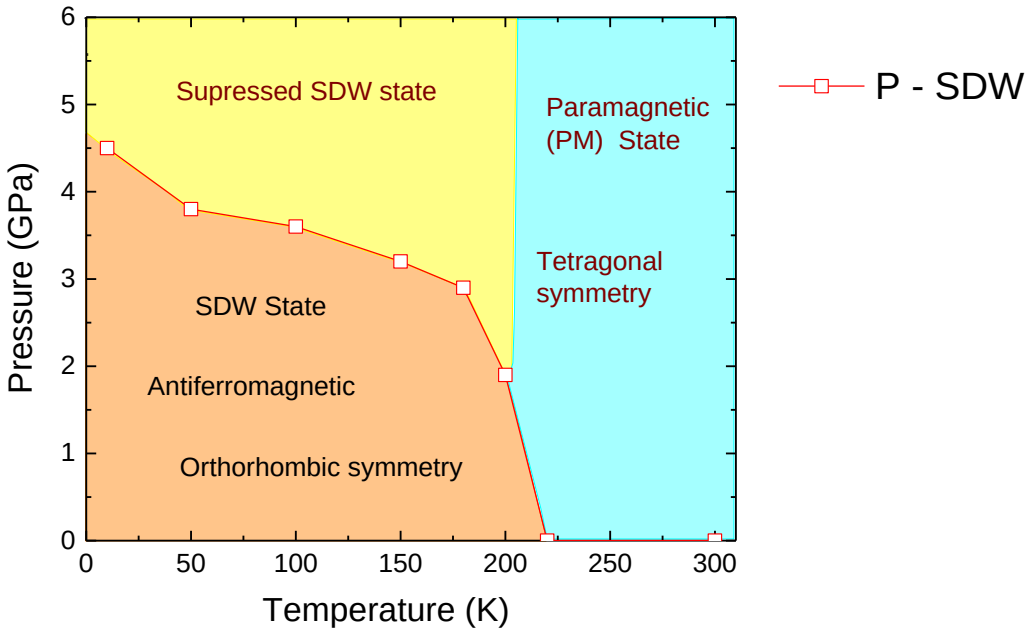

Figure 3.38. Pressure (T) – temperature (T) phase diagram for $SrFe_2As_2$, drawn on the basis of P_{SDW} (minimum pressure) required to suppress SDW gap as given in table – 2.3.

3.4. Experimental results and discussion for $SrFe_{1.9}Co_{0.1}As_2$

In this part of thesis, the effect of high–pressure (0–1.8 GPa) was studied on the SDW state by measuring the near–normal incident reflectivity for the single crystal of $SrFe_{1.9}Co_{0.1}As_2$ Pnictide at various temperatures (300–10 K), in the mid–infrared range.

Since the compound was doped, the SDW state was suppressed completely for a smaller pressure compared to the undoped compound. The experimental results and discussions will be presented in this section.

3.4.1. Pressure cycles

In this section, the measured pressure–cycles for $SrFe_{1.9}Co_{0.1}As_2$ are shown at various temperatures (300–10 K). The pressure was set at room–temperature and low–temperature infrared reflectivity was measured.

In Figure 3.39 (a) frequency–dependent reflectivity ($R_{s\text{-}d}$) is shown at 0.4 GPa for various temperatures. The reflectivity above 3000 cm^{-1} shows almost no pressure or temperature dependence. Figure 3.39 (b) shows an enlarged view of Figure 3.39 (a) in the low frequency regime. The reflectivity shows a clear suppression at 50 K and 10 K in the 780–1000 cm^{-1} frequency range. The reflectivity starts to increase like a Drude tail below 780 cm^{-1}, which confirms the existence of a SDW gap in $SrFe_{1.9}Co_{0.1}As_2$ at 10 K and 50 K.

The strength of the SDW gap is small compared to the undoped $SrFe_2As_2$ (see Figure 3.17 (b)) which indicates that $SrFe_{1.9}Co_{0.1}As_2$ lies at the border line of the “SDW” and “suppressed SDW” states. A. Lucarelli et al [170] also reported the existence of a SDW gap for $Ba(Co_xFe_{1-x})As_2$ at x = 0.05 ($BaFe_{0.94}Co_{0.05}As_2$), which is completely suppressed for higher doping concentrations, i.e. for $x \geq 0.11$ ($BaFe_{0.89}Co_{0.11}As_2$).

In Figure 3.40 (a) the pressure–dependent reflectivity at 0.8 GPa is shown for the various measured temperatures. The reflectivity (see Figure 3.40 (b)) shows a decrease in the strength of the SDW gap at 50 K and 10 K. Figure 3.40 (b) shows reflectivity at 1.4 GPa which indicates the complete suppression of SDW gap for all measured temperatures, confirming the conventional metallic behaviour of $SrFe_{1.9}Co_{0.1}As_2$.

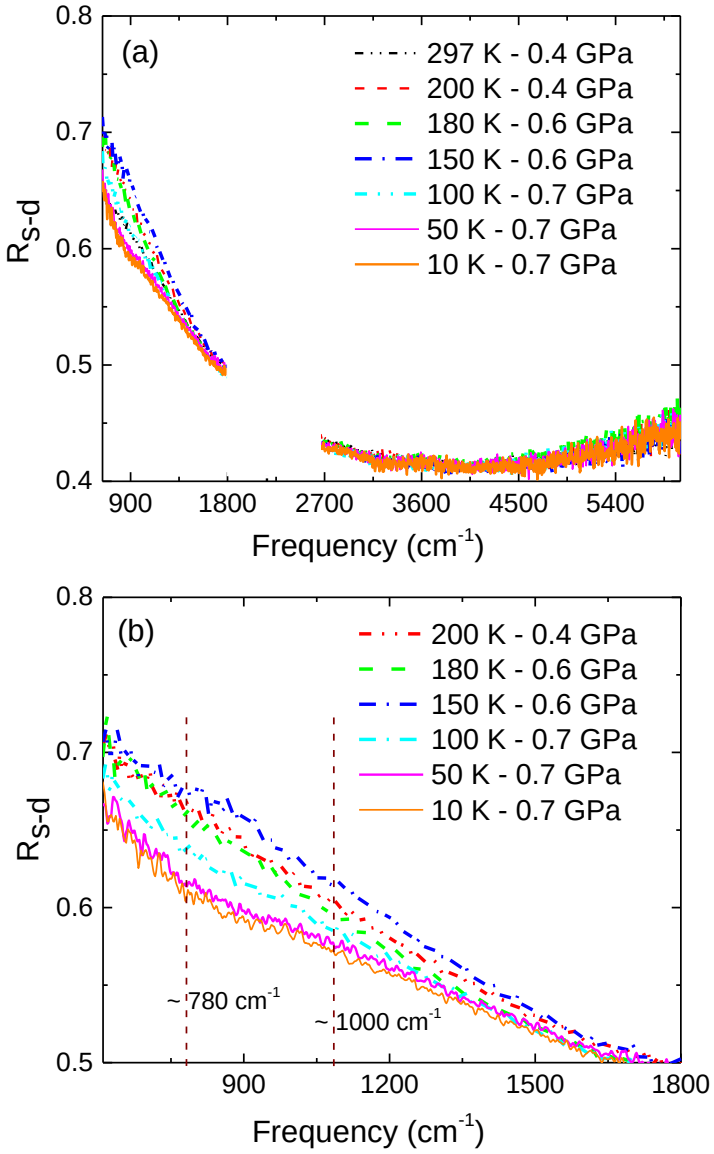

Figure 3.39. (a) Reflectivity (R_{s-d}) of $SrFe_{1.9}Co_{0.1}As_2$ at 0.4 GPa for various measured temperatures. (b) Enlarged view of the left panel in the low frequency range.

In order to check the reversibility of SDW transition, a releasing pressure cycle was measured at 0.8 GPa. Figure 3.41 (a) shows the reflectivities at 297 K, 180 K and 150 K which indicates an increase in reflectivity level with decreasing temperature.

Two straight lines were fitted at low (750 cm^{-1}) and at high frequency (1300 cm^{-1}) parts of each spectrum and their slope ratios (R) are shown in Figure 3.40 (b). Indeed, the slope ratios (R) show the absence of any SDW gap, but the drop in reflectivity level can be taken as an indication that some sort of SDW ordering exists. Therefore, it was taken as an indication of

the reopening of the SDW gap. The physics behind the phenomena is already explained in section 3.3.1, relating to releasing pressure cycles for the undoped $SrFe_2As_2$.

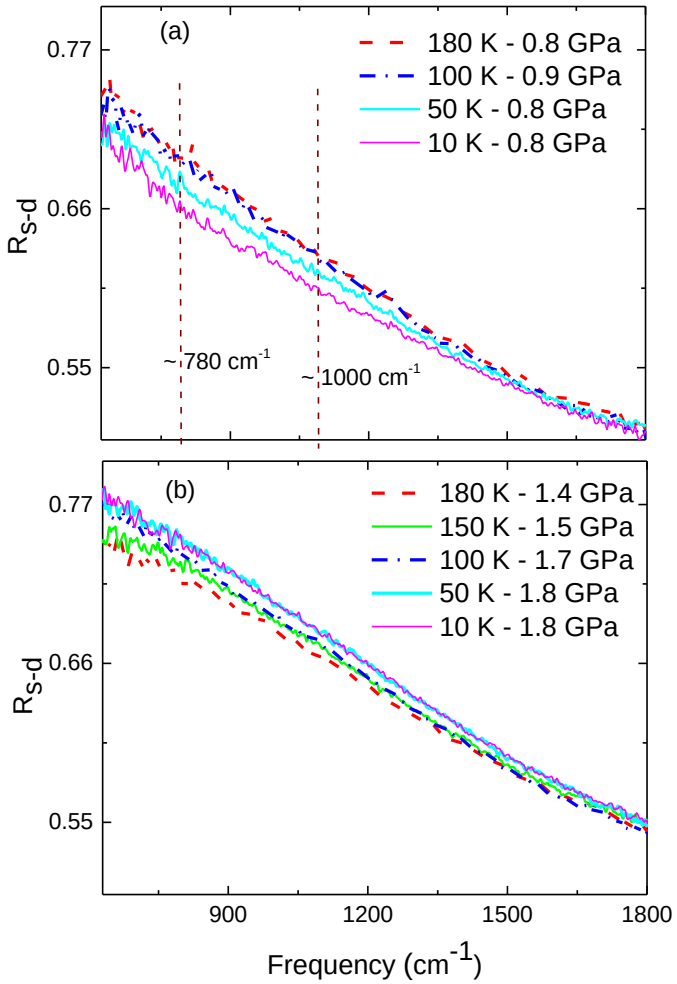

Figure 3.40. Reflectivity (R_{s-d}) of $SrFe_{1.9}Co_{0.1}As_2$ for various measured temperatures under high–pressures. (a) At 0.8 GPa and (b) at 1.4 GPa.

3.4.2. Temperature cycles and Phase diagram

The spectra for various pressures at same temperature were separated and plotted as "temperature cycles" in order to observe the explicit behaviour under pressure at each temperature as shown in Figure 3.42 and Figure 3.43.

In order to quantify the SDW gap, two straight lines were fitted, as described in section 3.3.4, at 750 cm^{-1} (low frequency LF) and at 1300 cm^{-1} (high frequency HF) for each spectrum (see Figure 3.42 and Figure 3.43). The ratio of slopes (R) was calculated and shown with the

corresponding spectra. The criteria was developed to assign the spectra to the paramagnetic or the suppressed SDW state for the slope ratio (R) ≤ 1.3, while for $R \geq 1.3$ the spectra were taken as in the SDW state.

In Figure 3.42 (a) reflectivity at 150 K is shown, which shows the absence of the SDW gap for all measured pressures, because $R \leq 1.3$. Figure 3.42 (b) shows the reflectivity at 100 K, where the slope ratios at 0.7 GPa (R_1 = 1.34) and 0.9 GPa (R_2 = 1.52) may indicate the existence of a SDW gap. The SDW gap was suppressed completely at 1.0 GPa (R_3 = 1.34) and 1.1 GPa (R_4 = 1.04).

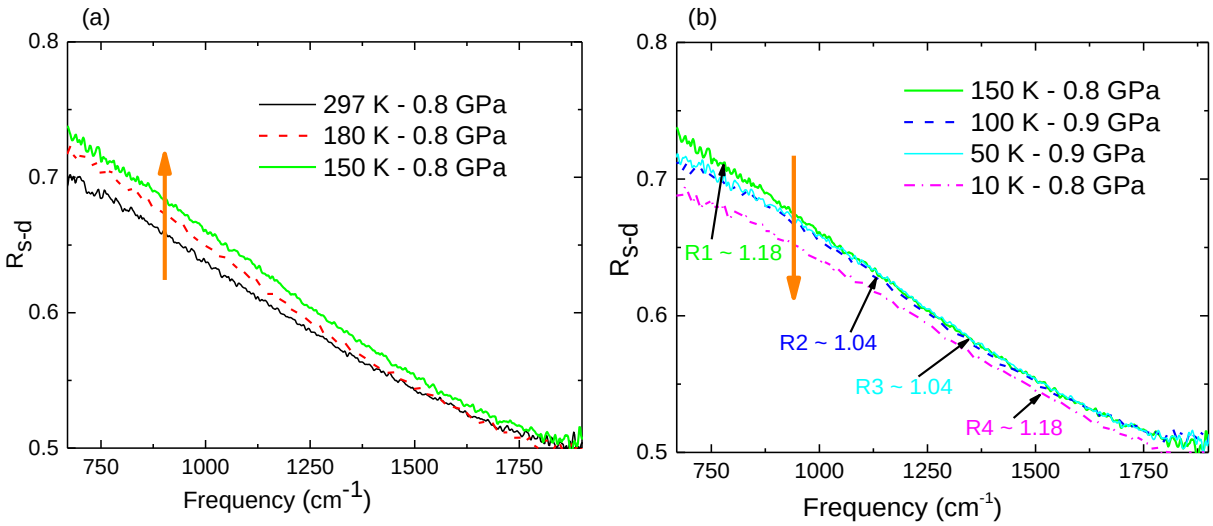

Figure 3.41. Releasing pressure cycle for $SrFe_{1.9}Co_{0.1}As_2$ at 0.8 GPa, shows the reflectivity at various temperatures. (a) At 297 K, 180 K and 150 K. (b) At 150 K, 100 K, 50 K and 10 K. The ratio of the slopes (R) of linear–fits to the reflectivity for each curve is shown with similar colour.

In Figure 3.43 (a) reflectivity at 50 K is shown, where R_1 increased to 2.00 for the spectrum at 0.7 GPa. The ratio gradually decreases as the pressure increase and approaches R_3 = 1.11 at 1.0 GPa, which corresponds to the suppressed SDW state. In Figure 3.43 (b) the SDW gap exists at 10 K up to a pressure of 1.0 GPa, while it is suppressed completely at 1.1 GPa.

The phase diagram is drawn on the basis of the above mentioned criteria and shown in Figure 3.44. The paramagnetic phase is represented by an area filled with cyan colour and the area is comparatively larger than that of undoped $SrFe_2As_2$ (see Figure 3.37) compound. The suppressed SDW state is represented by a yellow colour.

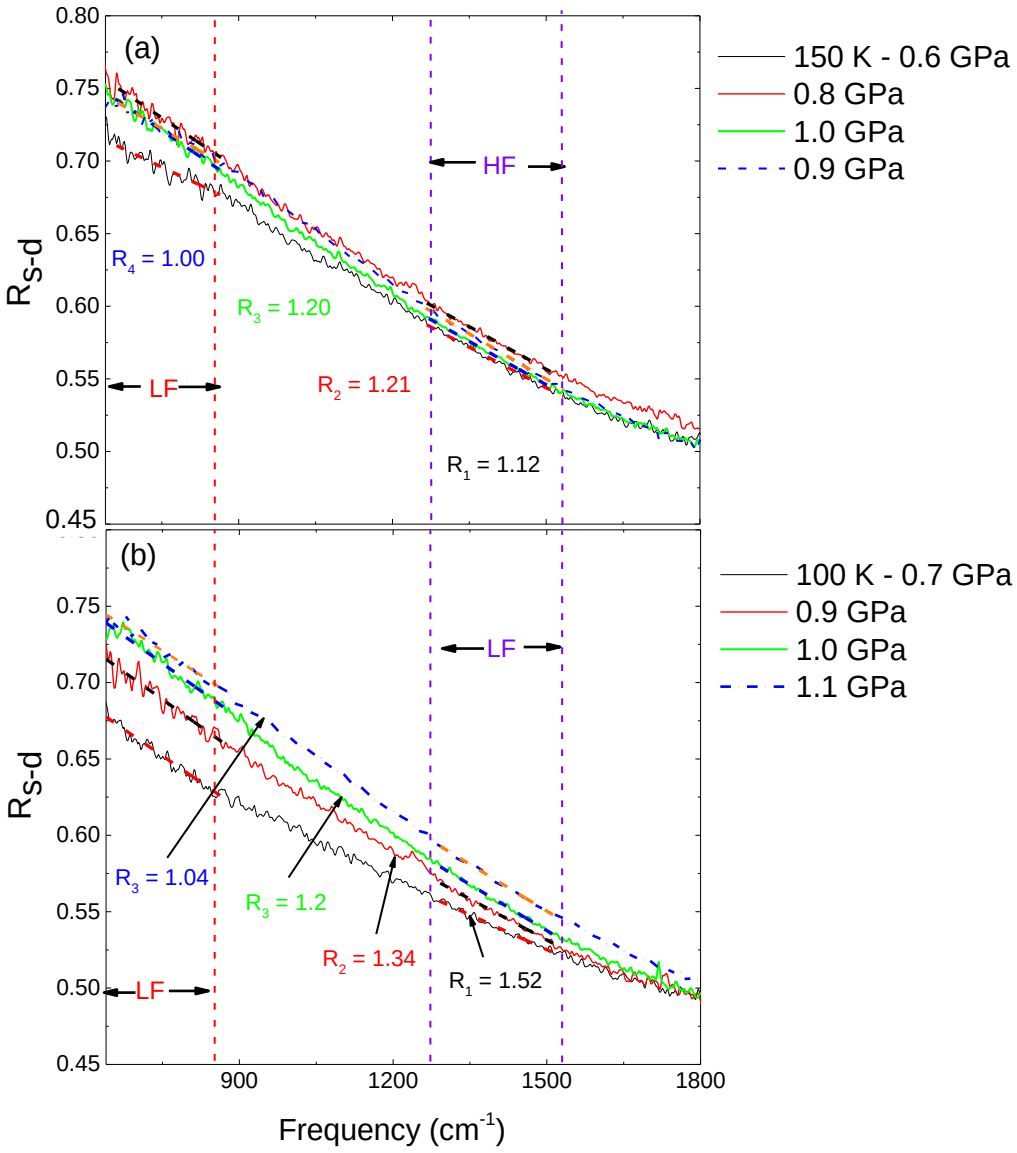

Figure 3.42. Temperature cycles for $SrFe_{1.9}Co_{0.1}As_2$ show the reflectivity at various measured pressures. The dashed lines corresponds to the linear fits at low (LF) and high (HF) frequency ranges. The ratio of slopes (R) for two linear fits at each spectrum was calculated. For R ≤ 1.3, the spectra were taken as paramagnetic or suppressed SDW state, while for R ≥ 1.3, the spectra was assumed in SDW state. (a) At 150 K, the ratio of the slopes (R) for all spectra is ≤ 1.3, representing a paramagnetic state. (b) At 100 K, the black (R_1 ~ 1.52) and red (R_2 ~ 1.34) spectra are in SDW state, while green (R_3 ~ 1.2) and blue (R_4 ~ 1.04) are in suppressed SDW state.

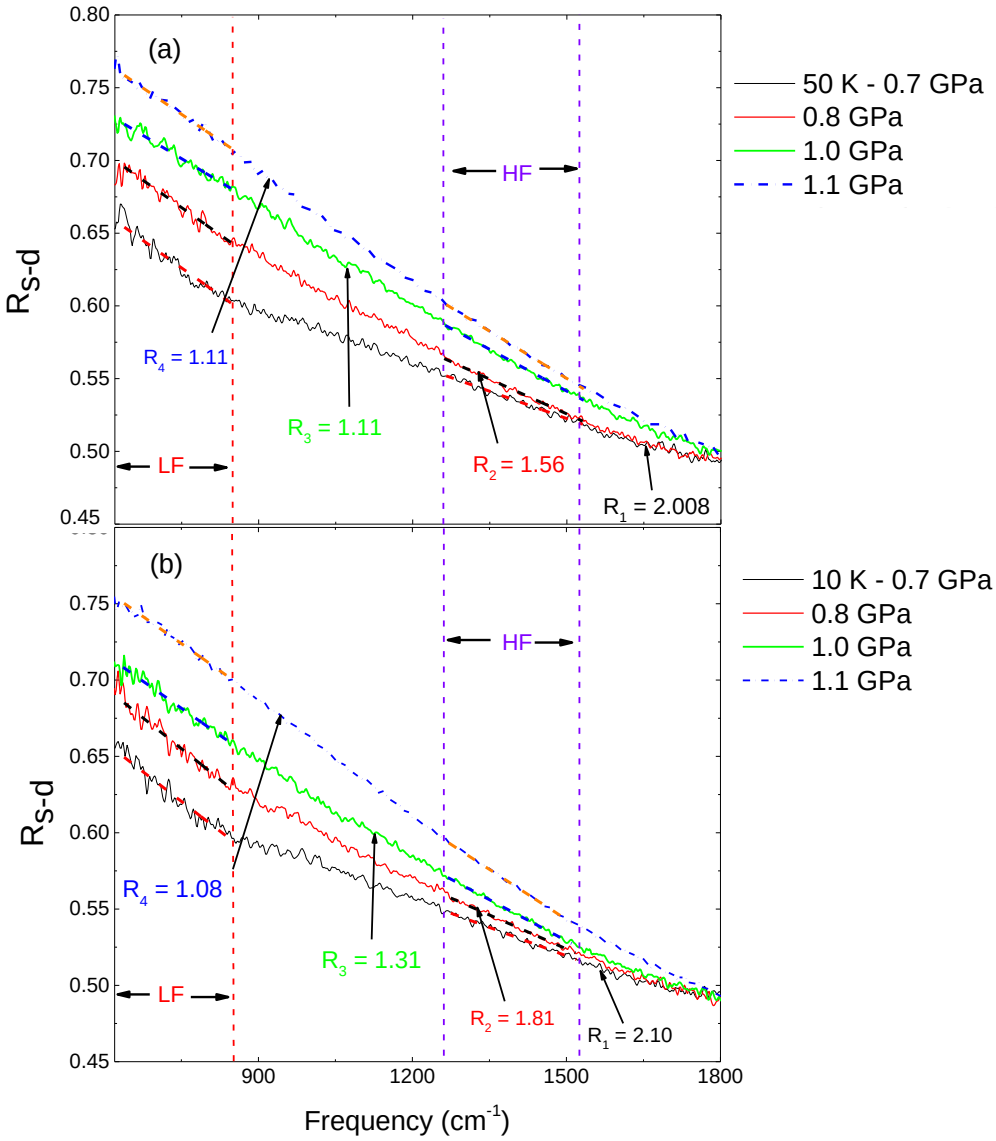

Figure 3.43. Temperature cycles for $SrFe_{1.9}Co_{0.1}As_2$ shows the reflectivity at various measured pressures. The dashed lines corresponds to the linear fits at low (LF) and high (HF) frequency ranges. (a) At 50 K, the black (R_1 ~ 2.00) and red (R_2 ~ 1.56) spectra are in SDW state, while green (R_3 ~ 1.11) and blue (R_4 ~ 1.11) spectra are in suppressed SDW state. (b) At 10 K, the black (R_1 ~ 2.10), red (R_2 ~ 1.81) and green (R_3 ~ 1.31) spectra are in SDW state, while only blue (R_4 ~ 1.08) spectrum is in suppressed SDW state.

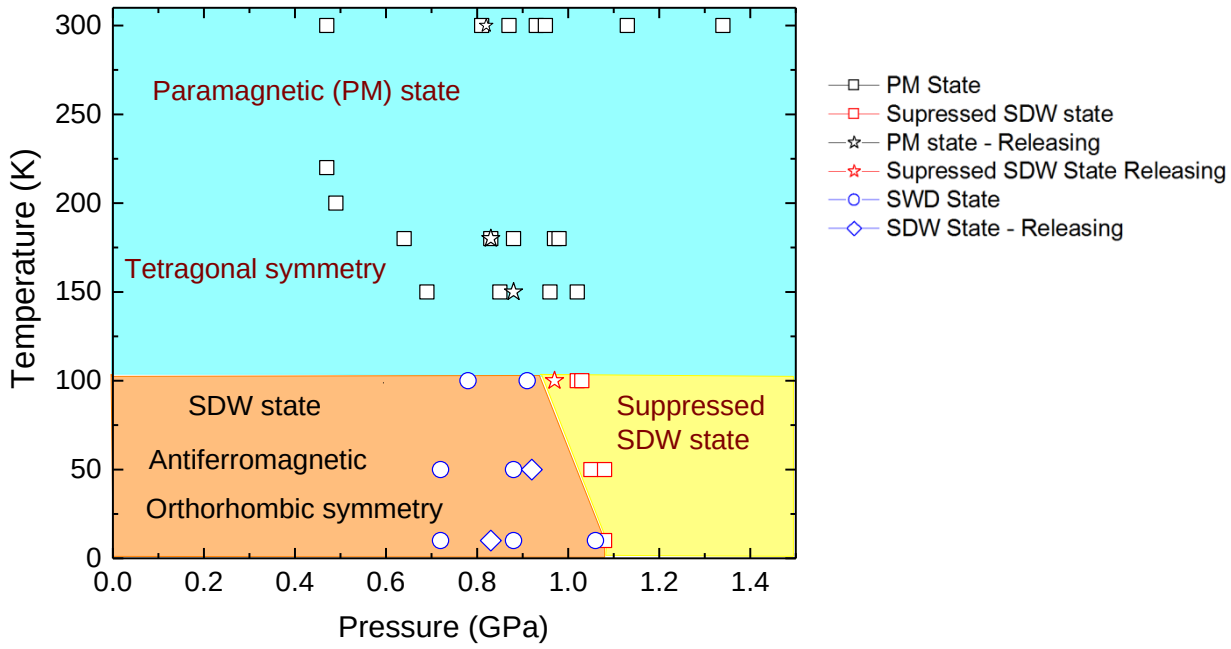

Figure 3.44. Pressure–temperature phase diagram of $SrFe_{1.9}Co_{0.1}As_2$, drawn on the basis of measured LTHP reflectivity data. The black squares represent the paramagnetic (PM) state, while the red squares indicate the suppressed SDW state. The stars represent the releasing pressure values. The blue circles indicate the SDW state, while blue diamond represents the suppressed SDW state.

In fact, higher pressure of around 4.5 GPa was required to suppress the SDW state for $SrFe_2As_2$ (see Figure 3.37) while for $SrFe_{1.9}Co_{0.1}As_2$ a pressure of around 1 GPa was enough to suppress the SDW gap as shown in Figure 3.44.

The cobalt doping decreases the onset of the SDW ordering temperature (T_{SDW}) to 100 K, which is decreased by about 100 K compare to undoped $SrFe_2As_2$ (see Figure 3.37). The results are consistent with the doping dependent phase diagram for $BaFe_{1-x}Co_xAs_2$ [31] and Pt doped $SrF_{2-x}Co_xAs_2$ [96] compounds. This verifies the phenomena for the effects of doping and pressure for $SrFe_{2-x}Co_xAs$, at $x = 0$ and 0.1.

The size of the dopant atoms does not show a clear relationship with the SDW or superconducting transition temperatures. Since the atomic size of Co, Rh and Ir are 58.9, 102.9 and 192.2 dalton respectively, doping the Fe–As planes should create a huge difference in carrier concentration, if a simplified electron–phonon model [101] is considered.

Therefore, cobalt doped compounds should have the highest while Ir should have the lowest transition temperatures (T_c). However, the experimental results show a different picture for their T_c, i.e. Co ($T_c \approx 24$ K), Rh ($T_c \approx 22$ K) and Ir ($T_c \approx 23$ K) [101 - 105, 110, 120, 121].

Since the doping of the material with different transition elements has negligible effect on the transition temperatures (T_c), antiferromagnetic spin fluctuations could be a major source for driving the superconducting pairing mechanism in AFe$_2$As$_2$ compounds [101 - 105, 110, 120, 121].

3.4.3. Analysis of $SrFe_{1.9}Co_{0.1}As_2$ results

Since the pressure–dependent electrical conductivity data was not available for $SrFe_{1.9}Co_{0.1}As_2$, ambient temperature conductivities from the Fig 4 of E. Colombier [121] et al were extracted for undoped $SrFe_2As_2$ as a function of pressure. The conductivity values at the ambient conditions were used to normalize the remaining higher pressures values. The normalized ratios were multiplied with the conductivity values for $SrFe_{1.9}Co_{0.1}As_2$ which was extracted from Figure 1 of reference–[169] at room temperature. This gives the pressure–dependent values of the electrical conductivities for $SrFe_{1.9}Co_{0.1}As_2$ compound, where the effect of temperature was assumed negligible [169].

The fitting model and extrapolations of $SrFe_2As_2$ as described in section 3.3.3 was used to fit the $SrFe_{1.9}Co_{0.1}As_2$ data with one additional oscillator *L6* at ~ 6000 cm^{-1}. The measured data along with the extrapolations and fitting curves is shown in Figure 3.45.

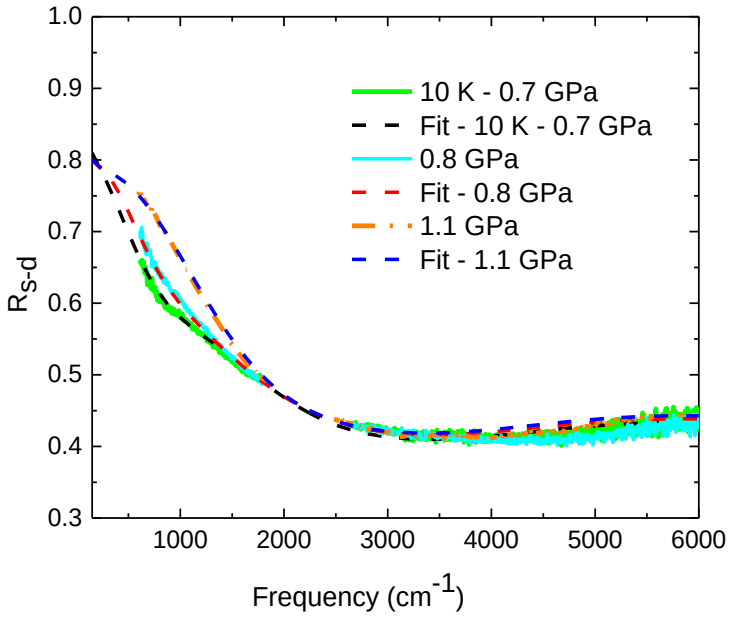

Figure 3.45. Reflectivity of $SrFe_{1.9}Co_{0.1}As_2$ at 10 K for various measured pressures with the Lorentz–Drude fits.

The real part of the optical conductivity with fitting contributions is shown in Figure 3.46 (a) at 0.7 GPa, where *D2* is sharp Drude and *L4*, *L5* are low frequency harmonic oscillators. The same fitting model was used to fit the higher pressures at 10 K by manipulating only *D1*, *L4* and *L5*. The pressure dependent real part of optical conductivity at 10 K is shown in Figure 3.46 (b). For room temperature (297 K) spectra, two Drude terms (*D1* and *D2*) with one harmonic oscillator (*L4*) were used as described in section 3.3.3.

The spectral weight for the Drude components (*D1* and *D2*) are shown in Figure 3.47 at 10 K, 100 K and 297 K. The error bar in the calculations is ~ 1 x 10^6 ohm^{-1} cm^{-2}, which is

comparable to the error bar of S. J. Moon et al [142]. The spectral weight of *D1* at 10 K - 0.7 GPa starts from ~ 5 x 10^6 ohm^{-1} cm^{-2} which is almost five times higher than the spectral weight of undoped $SrFe_2As_2$ as shown in Figure 3.32 (a).

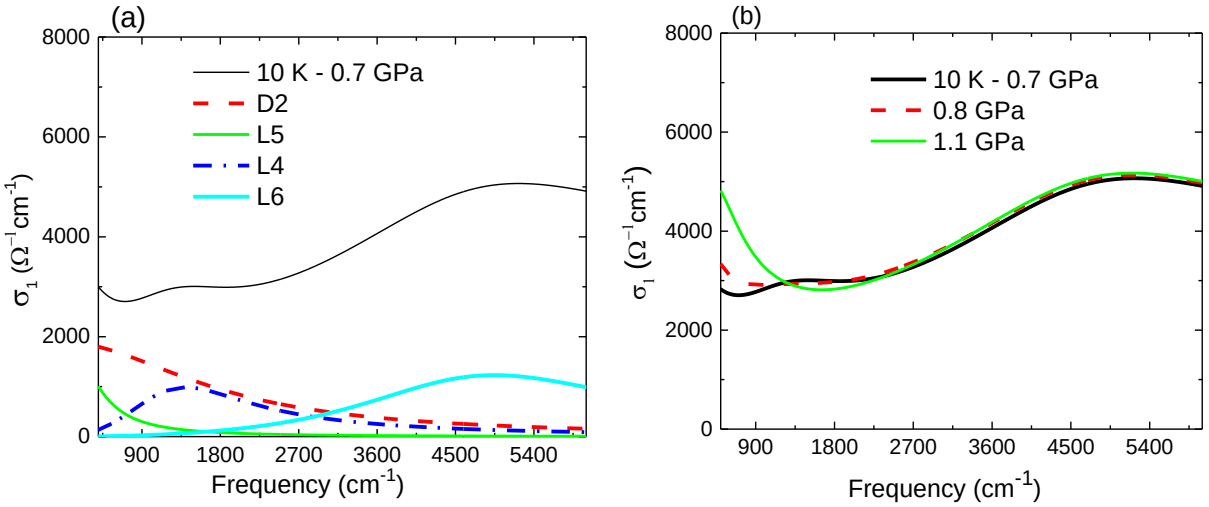

Figure 3.46. (a) Real part of the optical conductivity with fitting contributions for $SrFe_{1.9}Co_{0.1}As_2$ at 0.7 GPa, where D2 is sharp Drude term and L4 and L5 are the low frequency harmonic oscillators. L6 is an additional harmonic oscillator at around 6000 cm^{-1}, which was kept constant for fitting other spectra. (b) Pressure dependent real part of the optical conductivity at 10 K.

In Figure 3.46 (a) the spectral weight of harmonic oscillators *L4* and *L5* are shown at 10 K, 100 K and 297 K, which shows a complete suppression of *L5* at 0.8 GPa. The spectral weight of *L4* is comparable to the spectral weight of undoped $SrFe_2As_2$ at around 4 GPa (see Figure 3.33 (a)). The spectral weight of Drude terms and harmonic oscillators were used for calculating the degree of electronic correlations for the $SrFe_{1.9}Co_{0.1}As_2$ according to the method described in section 3.5.

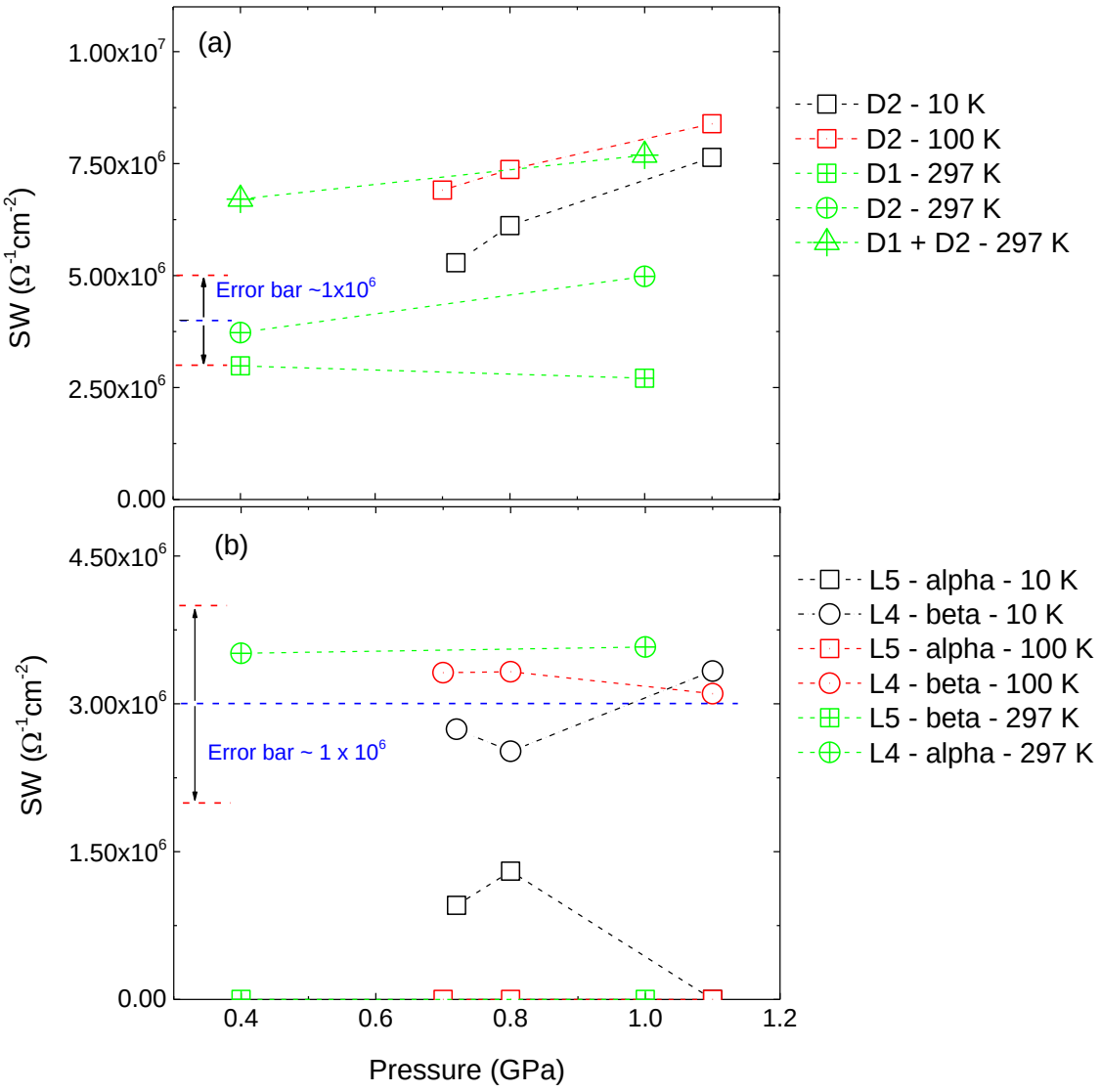

Figure 3.47. Spectral weight for the various fitting contribution at 10 K, 100 K and 297 K, for $SrFe_{1.9}Co_{0.1}As_2$. The error bar in calculations is 1 x 10^6 ohm^{-1} cm^{-2}, which is comparable to the calculations reported by S. J. Moon et al [142]. (a) For broad (D1) and sharp (D2) Drude components, where D1 is zero at 10 K and 100 K. (b) For harmonic oscillators, L4 and L5.

3.5. Electronic correlation effects

The kinetic energy of electron is an important parameter in order to study the many body effects on the electron. The electrons can be de-accelerated due to the interaction with their environment such as impurities or phonons, and an electron interacting with other electrons, spin ordering or magnetic interactions. Some of these effects are not taken into account by band structure calculations. Therefore, a direct measure of the reduction in kinetic energy of electron can provide a measure of the electronic correlations for a material.

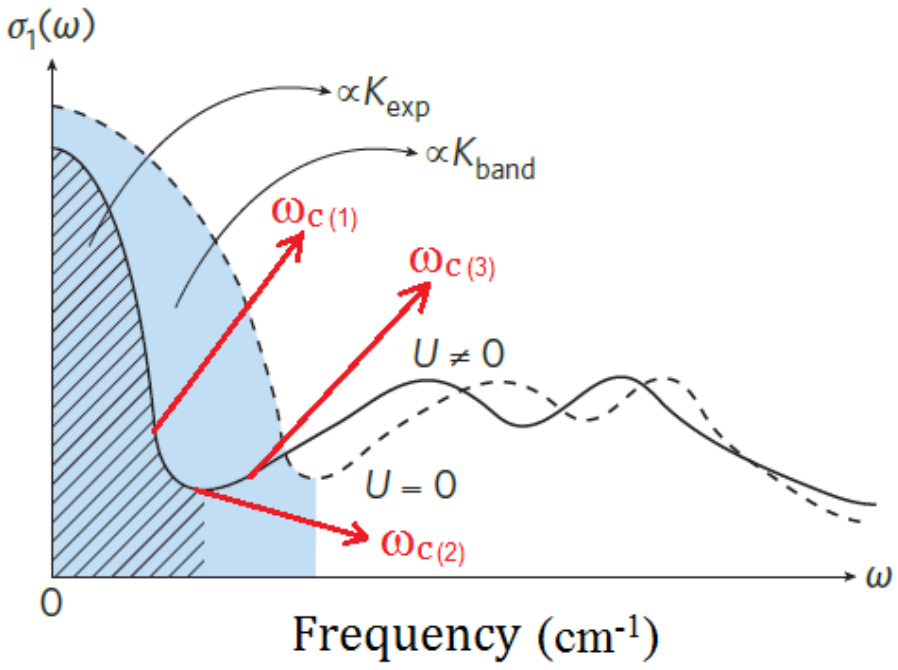

Figure 3.48. Real part of the optical conductivity extracted from band structure calculations (dashed lines) and from the experimental data (solid lines). K_{exp} and K_{band} represent the experimental and theoretical kinetic energies, ω_c represent the cut–off frequency, U is onsite coulomb–repulsion. The figure is taken and modified from–[163].

The kinetic energy (K) of the electrons can be calculated from the real part of the optical conductivity, which is proportional to the area under the Drude component as shown in Figure 3.48. The ratio between experimental (K_{exp}) and theoretical (K_{band}) kinetic energies gives a direct measure of the reduction in mobility of electron due to various interactions.

The value of kinetic energy can be defined as Eq. (3.2) [156, 162].

$$K(\omega_c) \;\alpha\; \int_0^{\omega_c} \sigma_1(\omega)d\omega \tag{3.2}$$

The integral shows the spectral weight of the Drude component up to the cut–off frequency (ω_c). Thus, the experimental kinetic energy can be calculated by using Eq. (3.3).

$$K_{exp}(\omega_c) = \frac{2\hbar^2 c_0}{\pi e^2} \int_0^{\omega_c} \sigma_1(\omega)d\omega \tag{3.3}$$

Where, e is the charge of the electron, h is Plank's constant and $\hbar = h/2\pi$, c_0 is the distance between Fe–As planes.

The selection of the cut–off frequency (ω_c) depends on the edge of $\sigma_1(\omega)$, as illustrated in Figure 3.48 for three different cases, i.e. $\omega_{c(1)}$, $\omega_{c(2)}$ and $\omega_{c(3)}$. The $\omega_{c(3)}$ seems to be not an appropriate estimate, because of some contributions from the inter–band transitions, while values smaller then $\omega_{c(1)}$ will cause a loss of spectral weight from the Drude component. Qazilbash et al [156] used two different cut–off frequencies in close proximity of the Drude component.

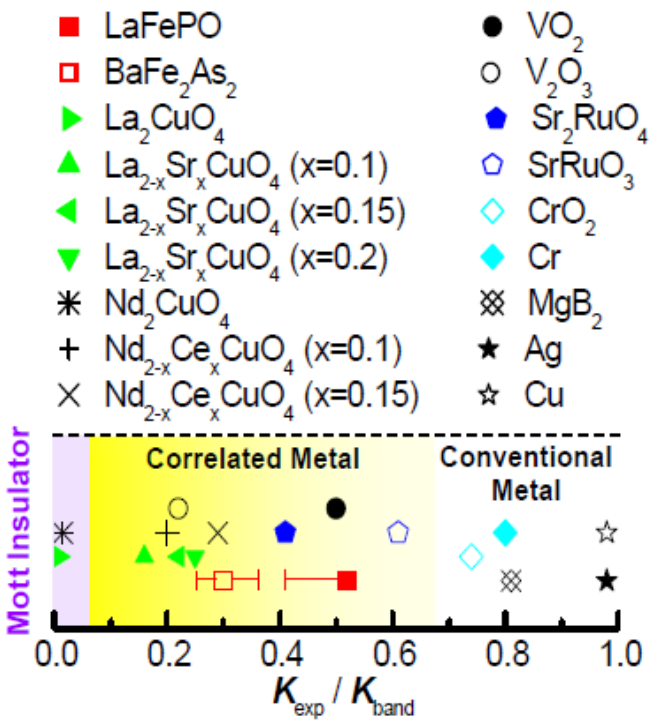

Figure 3.49. Classification of some famous materials on the basis of their K_{exp} / K_{band} ratios. The picture is taken from M. M. Qazilbash et al [156].

In Figure 3.49 the classifications of the materials are shown on the basis of their K_{exp} / K_{band} ratios. For gold and copper the values are close to 1. The conventional metals category expands to Cr and CrO_2 with the values ~ 0.75. The compounds $BaFe_2As_2$ and LaFePO lie in the area of moderately correlated metals [163].

The calculated K_{exp} / K_{band} ratio by Qazilbash et al [156] for LaFePO is done only at room temperature while the low temperature K_{exp} / K_{band} ratio is not shown. The reason might be the complication and larger error bars to calculate the ratio at each temperature. In case of LTHP data, the pressure effects will make theoretical approaches more difficult to find appropriate values for K_{exp} and K_{band}.

In order to rectify the above mentioned problem, A. Lucarelli et al [170] suggested a purely experimental approach for all states of material. It is simply based on the ratios between itinerant and localized carriers as given by Eq. (3.4).

$$\frac{\mathrm{K_{opt}}}{\mathrm{K_{band}}} = \frac{\text{Itinerant carriers}}{\text{Itinerant carriers} + \text{Localized carriers}} \tag{3.4}$$

The equation can be modified for the fitting parameters as follows.

$$\frac{\mathrm{K_{opt}}}{\mathrm{K_{band}}} = \frac{\int \sigma_{1N}(\omega)d\omega + \int \sigma_{1B}(\omega)d\omega}{\int \sigma_{1N}(\omega)d\omega + \int \sigma_{1B}(\omega)d\omega + \int \sigma_{1}^{MIR}(\omega)d\omega} \tag{3.5}$$

The numerator in Eq. (3.5)), shows the sum of spectral weight for the narrow and broad Drude components (K_{opt}), taken as itinerant carriers. The denominator represents the Drude component along with spectral weight of the mid infrared bands, i.e. *L5* (α) and *L4* (β). The scheme is illustrated in Figure 3.50 (a) for the paramagnetic state.

As the material cools down below T_{SDW} (see Figure 3.50 (b)) the SDW state is established which results in an increased localization of itinerant carriers due to the transfer of spectral weight from Drude components to *α* (*L5*) and *β* (*L4*). This appears as a drastic drop in K_{opt} / K_{band} ratio in SDW state, indicating a substantial increase in correlation effects. Henceforth, the Lucarelli [170] approach was used for estimating the K_{opt} / K_{band} ratio for both $SrFe_2As_2$ and $SrFe_{1.9}Co_{0.1}As_2$ compounds.

Figure 3.51 shows the K_{opt} / K_{band} ratio for $SrFe_2As_2$ at 10 K, 100 K, 200 K and 297 K as a function of pressure. The value at 10 K and at lowest pressure is 0.1 which is increased with increasing pressure and approaches to 0.7 at 5 GPa. This indicates that the material transforms to a conventional metallic system, after complete suppression of the SDW state. In Figure 3.52, its temperature dependent illustration of the K_{opt} / K_{band} ratio is shown for the various measured pressures within +/- 0.5 GPa. The K_{opt} / K_{band} ratio increases drastically below 100 K with increasing pressure while, at higher temperature, i.e. above T_{SDW}, the increase is considerably small.

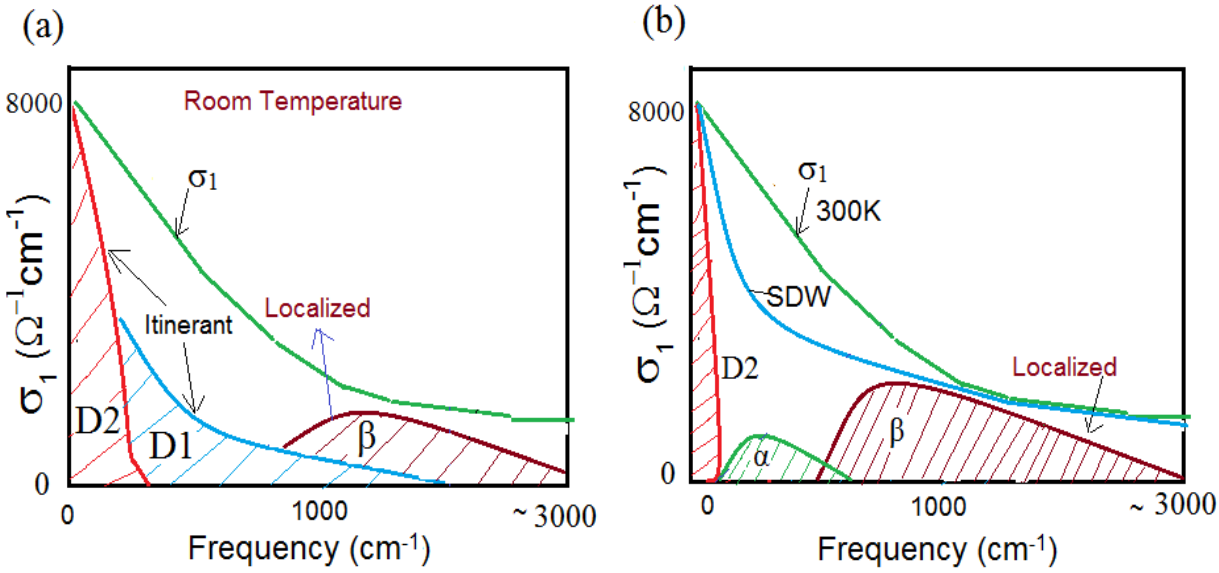

Figure 3.50. Schematic representation of the correlation effects in paramagnetic and SDW states. (a) Real part of the optical conductivity with two Drude components, which represents electronic and hole type itinerant carriers. The localized carriers are represented as β in the paramagnetic state. (b) Increased localization of itinerant carriers in SDW state, is observed as a transfer of the spectral weight from Drude component to the harmonic oscillators α (L5) and β (L4).

The calculated K_{opt} / K_{band} ratio for $SrFe_{1.9}Co_{0.1}As_2$ at 10 K, 100 K and 297 K is shown in Figure 3.53. The K_{opt} / K_{band} ratio at "10 K - 0.7 GPa" is around 0.6 and approaches 0.7 at 1.1 GPa. The ratio is consistent with the calculated ratio for the undoped $SrFe_2As_2$ at 5 GPa (see Figure 3.51). At 100 K and 297 K, the K_{opt} / K_{band} ratio is increased with a smaller amount and converges to 0.7 at highest measured pressure.

The K_{opt}/K_{band} (0.7) ratio in the suppressed SDW state for $SrFe_2As_2$ was almost close to the values of Cr and CrO_2 as shown in Figure 3.49. The value was also consistent with the calculated K_{opt}/K_{band} (0.6), for the optimal doped, $Ba(Co_xFe_{1-x})_2As_2$ at x = 0.17, as reported by A. Lucarelli et al [170]. The higher ratios of K_{opt}/K_{band} for $SrFe_2As_2$ and $SrFe_{1.9}Co_{0.1}As_2$ compounds in paramagnetic phases (297 K) were in contradiction with K_{exp}/K_{band} ratio (0.3) reported by Qazilbash et al [156] for $BaFe_2As_2$ (see Figure 3.49).

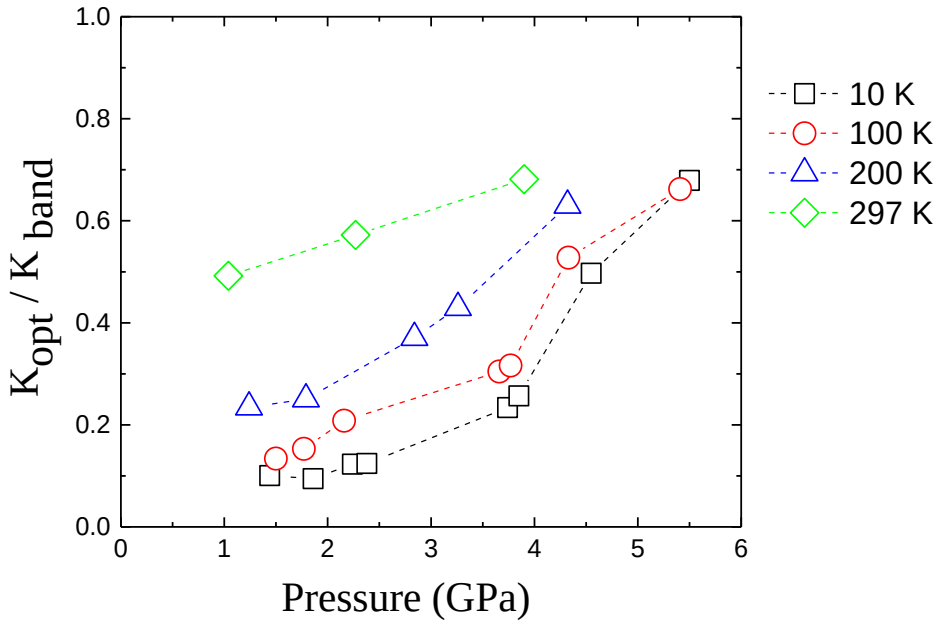

Figure 3.51. Pressure–dependent kinetic energies (K_{opt}/K_{band}) ratios for $SrFe_2As_2$ at 10 K, 100 K, 200 K and 297 K. The A. Lucarelli et al [170] experimental approach was used for computations. The error bar in calculations is around +/- 0.1.

Recently, L. Baldassarre et al [176] reported the kinetic energy ratios by both a theoretical and also the experimental approach by Lucarelli et al [170] for $BaFe_2As_2$. The calculated K_{opt}/K_{band} ratios by using Lucarelli's [170] experimental approach is started from 0.6 at ambient conditions (see Figure 3.54 (a)) which is increased with a small amount as the pressure increases and saturates to 0.7 at 10 GPa. This is in contradiction to the calculated ratio by Qazilbash et al [156] for $BaFe_2As_2$ at ambient conditions. This shows that there are larger discrepancies for finding a right value for the theoretical kinetic energy even at ambient conditions.

On the other hand, Baldassarre et al [176] reported a consistent K_{exp}/K_{band} (0.3) ratio with Qazilbash et al [156] from the theoretical calculations as shown in Figure 3.54 (b). However, the ratio does not show any clear trend with increasing pressure. Their ratio varies within a

range of 0.2 to 0.25 as a function of pressure (see Figure 3.54 (b)). This is in contradiction to the increase metallic behaviour of the $BaFe_2As$ and $SrFe_2As_2$ compounds with application of high–pressure. If the calculated ratio is considered to be right, then the ratio (K_{exp} / K_{band}) should increase from 0.2 (at lowest pressure) up to at least 0.6 at the highest pressure [176]. Thus, the theoretical approaches were found to be more erratic, when extracting the theoretical value of the kinetic energy (K_{band}). The higher ratio of K_{exp} / K_{band} (0.5) in the paramagnetic state seems to be more reliable, compared to the smaller ratio (0.3) as reported by Qazilbash et al [156].

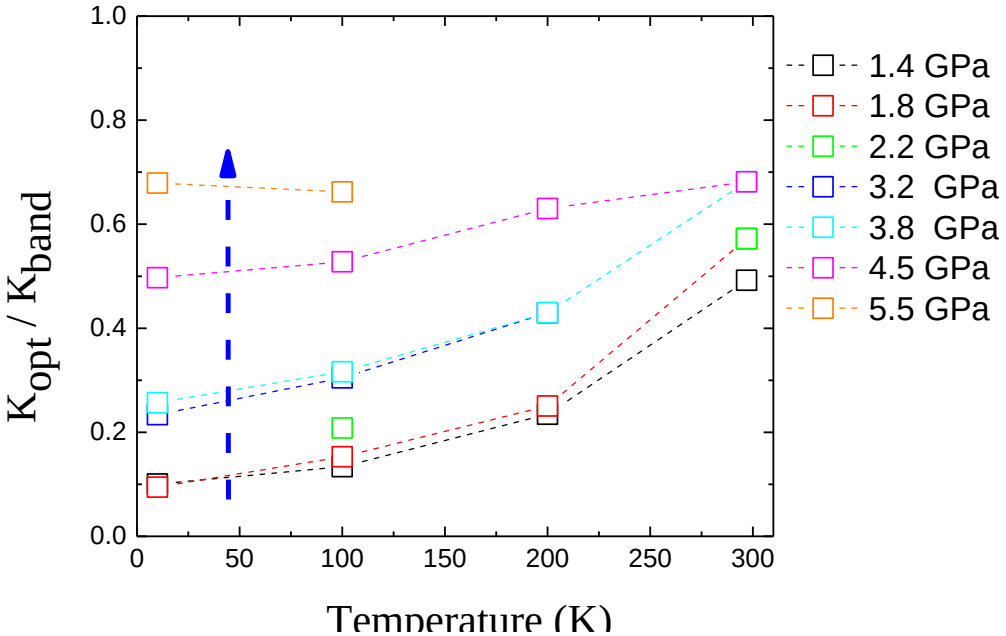

Figure 3.52. Temperature–dependent behaviour of kinetic energies (K_{opt} / K_{band}) ratio for $SrFe_2As_2$ at various measured pressure, which was grouped within a range of +/- 0.5 GPa.

The driving mechanism behind the drastic reduction in K_{exp} in iron–pnictides is somehow ambiguous and unclear. Unlike cuperates, they show poor metallic behaviour with magnetic ordering at low–temperature and without a complete insulating gap [164]. Furthermore, their electronic and magnetic properties vary significantly for the various phases, when synthesized with different pnictogen elements.

As in the case of LaFePO, the magnetic ordering and insulating behaviour is not observed [165, 166] but the spin correlation is reported by Singh [167] et al. However, spin correlation also exists in the paramagnetic phase (above T_{SDW}) of $BaFe_2As_2$. But the observed reduction in K_{exp} value for $BaFe_2As_2$ is found to be much smaller than expected, if only the spin

correlation will be considered. Therefore, Qazilbash et al [156] argue for the existence of "dynamical Coulomb correlation with onsite coulomb repulsion of the order of bandwidth and classified $BaFe_2As_2$ as moderately correlated metal, which lies in between the band like itinerant and Mott–like local magnetic moment type" [168].

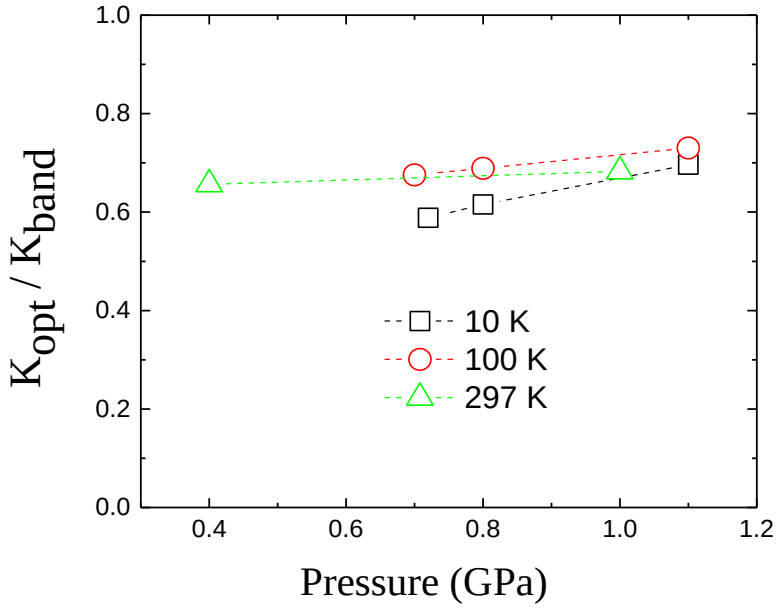

Figure 3.53. Pressure–dependent kinetic energies (K_{opt} / K_{band}) ratios for $SrFe_{1.9}Co_{0.1}As_2$ at 10 K, 100 K and 297 K by using the experimental approach by Lucarelli et al [170] as a function of pressure,

In fact, the assumption by Qazilbash et al [156] is based on smaller ratios of K_{exp} / K_{theo} (0.3) at room temperature, which contradicts the experimentally measured ratios. Thus, the measured LTHP data and analysis presented in this thesis suggests that $SrFe_2As_2$ can be classified as strongly correlated at 10 K ($K_{exp} / K_{band} \approx 0.1$) due to the strong electronic correlation in the SDW state. At 5 GPa, K_{exp} / K_{band} approaches 0.7 and the material can be classified as a conventional metal similar to Cr and CrO_2.

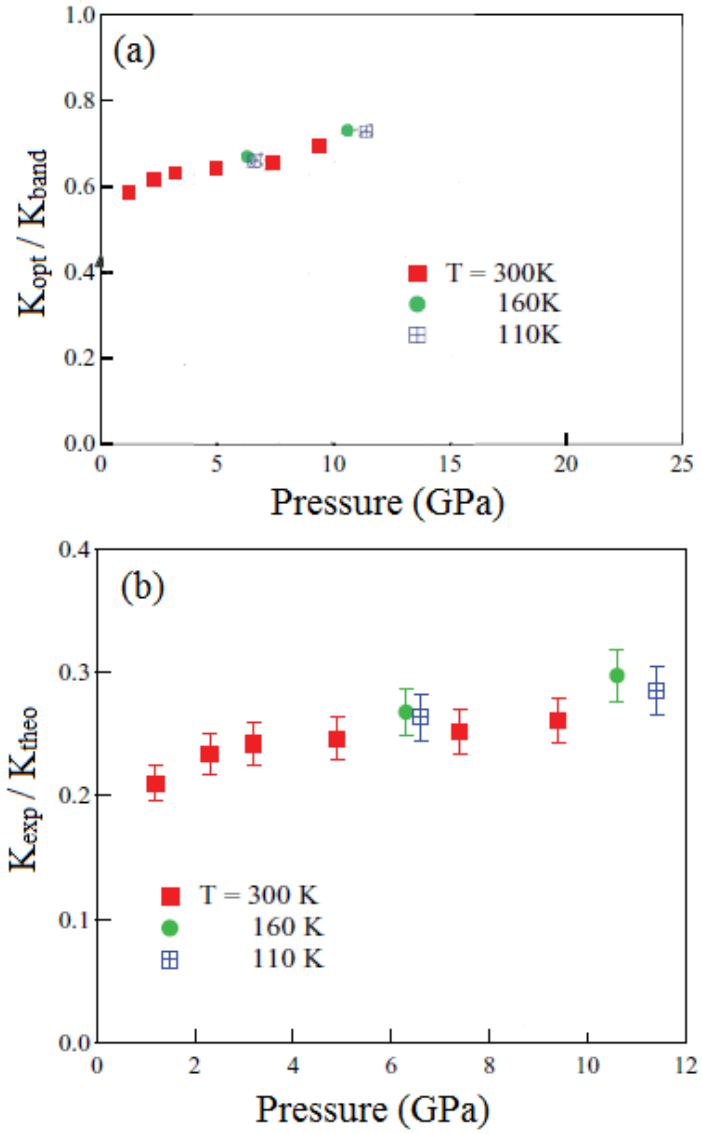

Figure 3.54. Baldassarre et al [176], calculated the kinetic energies ratio for $BaFe_2As_2$ (a) K_{opt} / K_{band} ratio by using the experimental approach by Lucarelli et al [170], at 300 K, 160 K and 110 K. (b) K_{exp} / K_{theo} ratio extracted from band structure calculations, at 300 K, 160 K and 110 K. The figures are taken and modified from – [176].

3.6. Summary

In this chapter, the electrodynamics of the SDW state was investigated for the parent compound $SrFe_2As_2$ and the doped $SrCo_{1.9}Fe_{0.1}As_2$ systems by using infrared spectroscopy under high–pressure and low–temperatures. The measurements were also tried with the synchrotron radiation source at ANKA as described in appendix–0.1.

The application of pressure shows a progressive suppression of the SDW gap for $SrFe_2As_2$. The drawn phase diagram shows that the SDW state was suppressed completely for pressures $\geq$ 4 GPa at 10 K, which is in good agreement with the electrical transport measurements as reported by Matsubayashi et al [29] and Kobayashi et al [129]. However, H. Okamura et al

[174] shows a complete suppression of the SDW gap at around 6 GPa, but their intermediate pressures between 4 and 6 GPa are not shown. In addition, they used glycerine or Daphne 7474 as pressure–transmitting media.

A smaller pressure of 1.7 GPa was enough to suppress the SDW state at 200 K compared to the pressure of 4 GPa required to suppress it at 10 K. This shows that the SDW state is more robust at low temperatures with respect to the structural deformation caused by the pressure.

The pressure–dependent electronic correlation (K_{exp} / K_{band}) ratio was calculated by using the experimental approach by Lucarelli et al [170]. The calculated K_{exp} / K_{band} ratio for $SrFe_2As_2$ at "10 K - 1.4 GPa", was found to be 0.1 and increased to 0.7 at 5.5 GPa. This is an indication of strong electronic correlations at 10 K which are suppressed at 5.5 GPa, indicating a conventional metallic response of $SrFe_2As_2$. This is consistent with the reported ratio of 0.6 by Lucarelli et al [170] for the optimally doped $BaFe_2As_2$.

The reflectivity was measured for the releasing pressure cycles, which shows reopening of the SDW gap, when the pressure was released to 2.4 GPa and 1.3 GPa. This shows that the reversibility of SDW transition increases with decrease in releasing pressure. Furthermore, the reversibility of SDW state was not observed at 200 K and 180 K, while it was recovered with a smaller intensity for temperatures ≤ 150 K. This confirms the weak first order [115] nature of the phase transitions caused due to the structural deformation in $SrFe_2As_2$ pnictide.

The cobalt doped $SrFe_{1.9}Co_{0.1}As_2$ pnictide was measured under high pressure and low temperatures. The pressure–temperature phase diagram was drawn on the basis of measured LTHP reflectivity data. The SDW state suppressed completely at 10 K for the smaller pressure of around 1.3 GPa compare to 4 GPa required for the undoped $SrFe_2As_2$. This indicates that $SrFe_{1.9}Co_{0.1}As_2$ lies at the border line of SDW (under doped) and suppressed SDW (over doped) states.

The calculated K_{opt} / K_{band} ratio for $SrFe_{1.9}Co_{0.1}As_2$ was found to be 0.6 at "10 K - 0.7 GPa", which was higher compared to the ratio calculated for undoped $SrFe_2As_2$ pnictide. The ratio increased to 0.7 at 1.1 GPa, which was consistent with the calculated K_{opt} / K_{band} ratio for $SrFe_2As_2$ at 5 GPa. This shows a remarkable consistency among the measured LTHP data for $SrFe_2As_2$ and $SrFe_{1.9}Co_{0.1}As_2$ pnictides presented in this thesis [89, 91, 93].

4. Europium hexaboride

4.1. Physical properties of EuB_6

EuB_6 is a correlated metal which undergoes phase transition from the paramagnetic (PM) to the ferromagnetic (FM) via two consecutive phases at 15.2 K and 12.2 K which corresponds to the phase separation between small magnetically ordered regions with mobile charge carriers and large disordered region with localized magnetic polarons. It shows large negative colossal magnetic resistance (CMR) when cooled down to liquid nitrogen temperatures [46, 47, 48].

It has a low itinerant carrier concentration, i.e. n ~ 19 cm^{-3}, with purely spin based Eu–4*f* moments. The interaction of itinerant carriers with localized magnetic moment of Eu–4*f* yields a substantial drop in electrical resistivity at the ferromagnetic ordering temperatures, which is observed as a huge shift of the plasma edge towards higher frequencies in the infrared reflectivity measurements [46- 48, 78].

4.1.1. Crystal structure

EuB_6 crystallize in simple cubic symmetry with the space group P/m–3m, where six boron atoms are connected to each other in the form of an octahedron, and the Eu ion at its centre. They form two cubic interpenetrating lattices of Eu and boron cages as illustrated in Figure 4.1. All boron atoms are apart from each other by a distance of 1.72 A_0 and form the covalent bonds within the boron cage [55, 56].

The oxidation state of the Eu in EuB_6 is +2, with localized magnetic moments at Eu sites which suggest that it is an *n*–type magnetic semiconductor [55, 56] while band structure calculations [45] found an overlap of valence and conduction band at the point–X of the Brillouin zone and designate it as a semimetal. This is in contradiction to the reported results based on ARPES (angle resolved photoemission), X–ray emission and absorption spectroscopic experiments where a band gap of more than 1 eV is found between valence and conduction bands [61].

The underlying physics of EuB_6 is complicated and it cannot be attributed to the Jahn–Teller effect or orbital ordering because of its simple chemical structure. In fact, it can be taken as a simple model system in order to understand the coupling between electronic and magnetic properties of the metal hexaborides [45, 46, 48, 55, 61, 78].

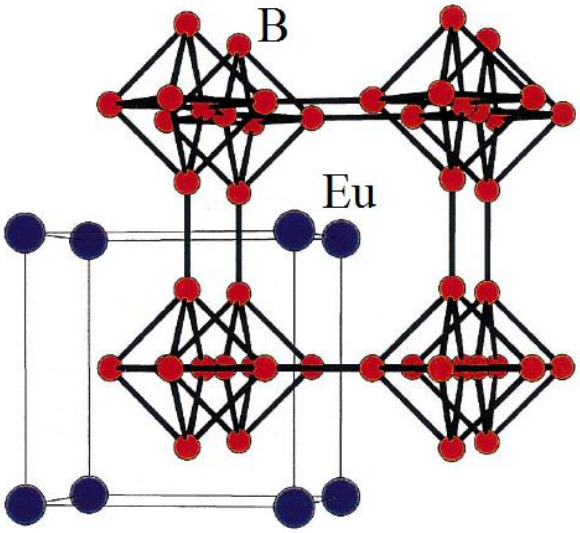

Figure 4.1. Crystal structure of EuB_6, where Eu is at the centre of boron cage. The figure is taken and modified from K. Schmitt et al [55].

4.1.2. Electronic structure

The electronic band structure of EuB_6 as reported by S. Massidda et al [60] by using full potential linearized augmented plane wave (FLAPW) method within the local density approximation (LDA) is shown in Figure 4.2. The solid lines represent the majority (*n*–type) and dash line shows the minority carriers (*p*–type). The major contribution comes from the B–2*p* (inter and intra cage) and Eu–4*f* bands. The Eu–4*f* state lies at 1.5 eV below Fermi level, indicating an existence of a clear band gap [58].

The antiferromagnetic ordering of the half filled 5*f* band produces a downward shift in the majority states at point X in the Brillouin zone, where the band crosses the Fermi surface and the majority carrier states overlap with both minority and majority carrier states as shown in Figure 4.2. Therefore, EuB_6 is classified as a semimetal according to band structure calculations.

However, angle resolved photoemission spectroscopy (APRES) [61] suggest the semiconducting picture of EuB_6 and found a band gap of 1 eV which weekend the idea of band overlap (Δ) as suggested by the band structure calculations. Furthermore, CaB_6 is also

expected to be a semimetal according to the LDA (local density approximation) calculations but GW [62] and weighted density approximation [63] found a gap of 1 eV which shows consistency with experimental results and makes the LDA calculations more questionable [81].

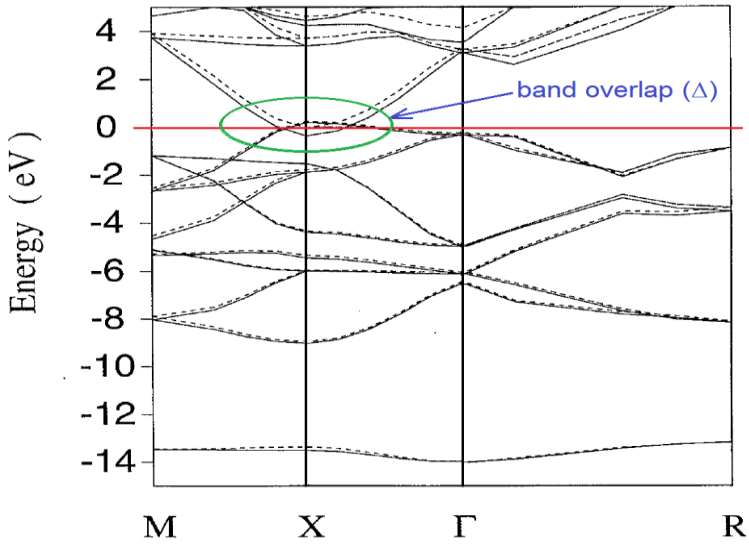

Figure 4.2. Band structure of EuB_6 as reported by S. Massidda et al [60]. Solid lines represent minority (n–type) and the dashed lines corresponds to majority carriers (p–type). The figure is taken and modified from -[60].

4.1.3. Effect of doping

The physical properties of EuB_6 can be tuned by means of doping or by introducing defects.

Doping of carbon at boron sites in $EuB_{6-x}C_x$ substitutes the boron atoms and behaves like a single electron donor. Since the radius of the carbon atom is smaller than that of the boron atom, the lattice parameters start to shrink with increasing carbon concentration. This leads to the suppression of the ferromagnetic state while antiferromagnetic ordering starts to increase with increasing carbon concentration [49, 50].

The electrical transport measurement on $EuB_{6-x}C_x$ shows an increase of conductivity with increasing carbon concentration which appears as a large shift of plasma edge towards higher frequencies as shown in Figure 4.3. The level of reflectivity increases for x = 0.8 % but start to drop down for the higher doping concentration, i.e. ≥ 1.45 %, which is consistent with the measured reflectivity data for higher pressures as shown in Figure 4.15 (b). The phonon mode gets weaken and screened out completely for the higher carbon concentration, i.e. ≥ 1.43 at. %.

The neutron diffraction experiments suggest the coexistence of ferromagnetic and a helimagnetic (spiral structure formed due to the antiferromagnetic ordering) phases in the $EuB_{6-x}C_x$ corresponding to the lower and higher doping values [51].

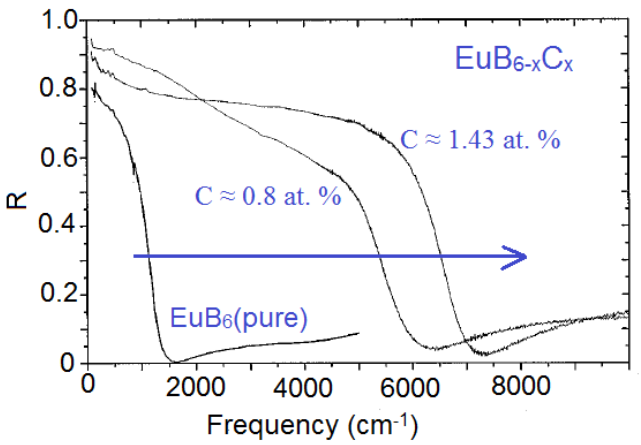

Figure 4.3. Reflectivity of $EuB_{6-x}C_x$ for various carbon concentrations at boron sites, as reported by H. Werheit et al [52]. The plasma edge shifts to higher frequencies with increasing carbon concentration. The figure is taken and modified from - [52].

Doping of alkaline earth Ca in $Eu_{1-x}Ca_xB_6$ shows the decrease of electrical conductivity with increasing Ca concentration, which leads to an insulating state. In optical measurement a large shift of plasma edge toward lower frequencies (see Figure 4.4) is observed while interband transition moves toward higher frequencies. This indicates that the band overlap at the X–point in the Brillouin zone decreases with increasing Ca concentration and approaches a finite insulating gap of ~ 0.25 eV. The phonon mode at 150 cm^{-1} gets stronger while the mode at 850 cm^{-1} screened out completely [52, 78].

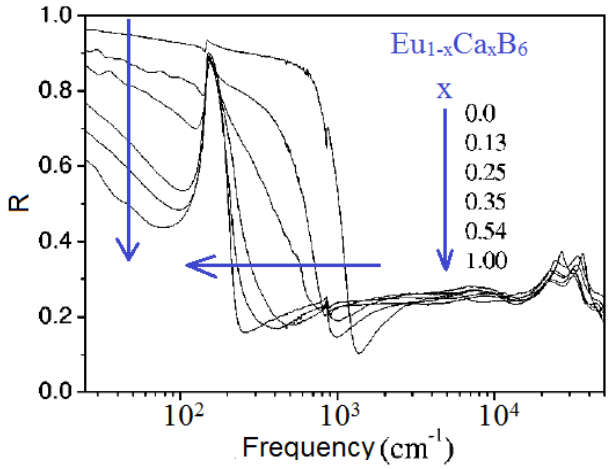

Figure 4.4. Infrared reflectivity of $Eu_{1-x}Ca_xB_6$ for various Ca concentrations at Eu sites, as reported by J. H. Kim et al [78]. EuB_6 at x = 0 and CaB_6 at x = 1. The plasma edge shift to lower frequencies and also reflectivity level decrease significantly below 1000 cm^{-1} with increasing Ca concentrations, as indicated with blue arrows.

Doping of rare earth (*RE*) La in $Eu_{1-x}La_xB_6$ shows contrasting results, i.e. for $x \leq 0.03$, the ferromagnetic transition temperature (T_c) is lowered and the conductivity increases rapidly below T_c. In contrary, at higher doping concentration, i.e. $0.05 \leq x \leq 0.2$, the ground state

changed to the frustrated magnetic insulating state which orders antiferromagnetically when the doping further increase to x = 0.3 [53, 54].

4.1.4. Electrical transport experiments

The electrical resistivity at zero frequency shows an anomaly around 15 K, due to the ferromagnetic ordering (see Figure 4.5 (a)) of EuB_6 as reported by J. C. Cooley et al [56]. The substantial drop in resistivity is due the interaction of itinerant carriers with the localized magnetic moment of Eu–4*f* [46- 48, 78].

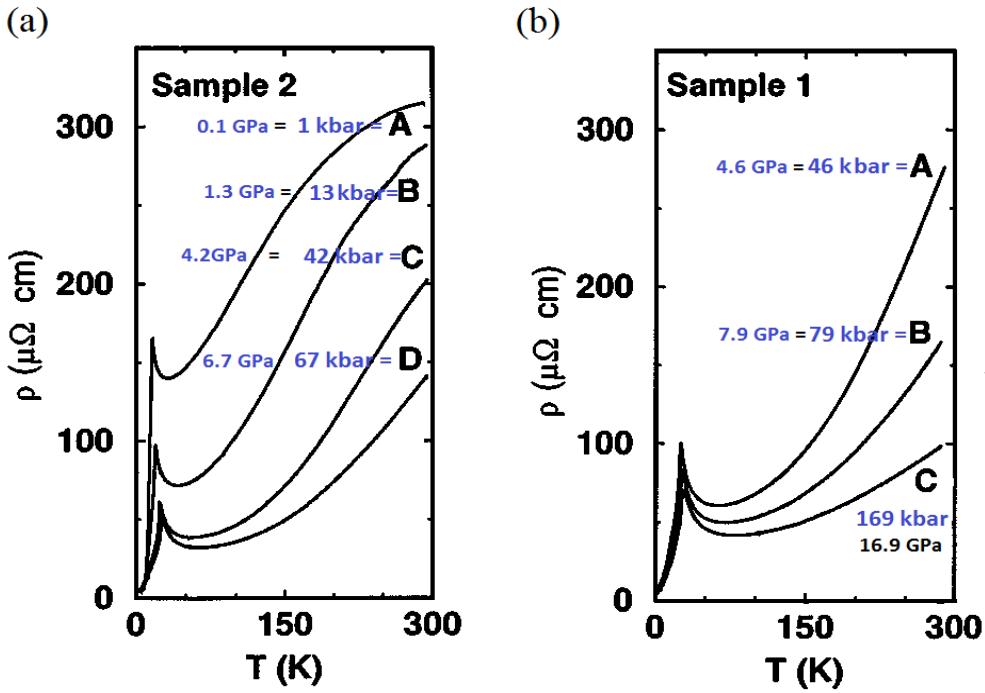

Figure 4.5. Electrical resistivity of EuB_6 measured at various pressures, as reported by J. C. Cooley et al [56]. (a) Sample–2 is used for low pressure, and (b) sample–1 is used for high pressure measurements. The figure is taken and modified from–[56].

Two samples are used to carry out the measurement by J. C. Cooley et al [56]. Sample–1 (Figure 4.5 (b)) is used for high pressure and sample–2 (Figure 4.5 (a)) for the low pressure measurements. The resistivity shows a decreasing trend when the pressure was increased and the sharp anomaly at T_c overlaps at higher pressure values as shown in Figure 4.5 (b).

The first order derivative of the resistivity curve gives the sharp two peaks feature, relating to the two ferromagnetic ordering temperatures. The two peaks are classified as an upper (T^+)

and a lower (T^-) resistive ordering temperatures which get broader and reduced its magnitude with increasing pressure. The authors [56] developed a pressure–temperature phase diagram by using these two transition temperatures as shown in Figure 4.6. It shows a steep increase in the transition temperatures up to 5 GPa, which becomes almost saturated with further increase in pressure.

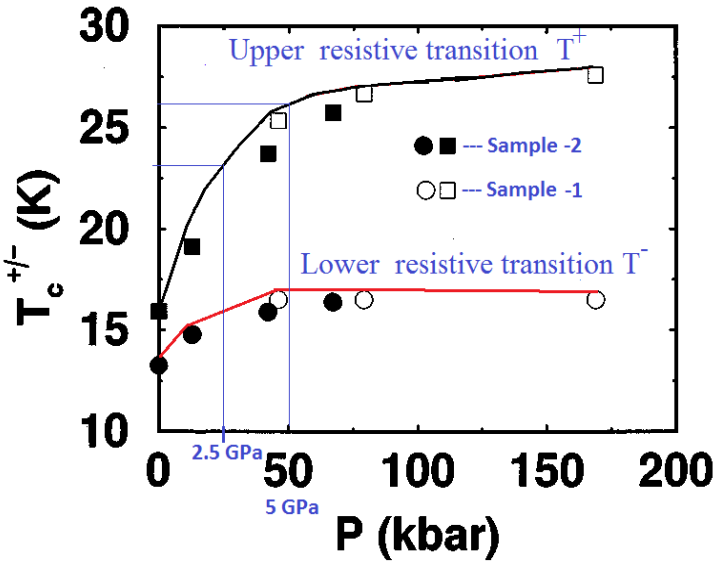

Figure 4.6. Phase diagram of EuB_6 drawn on the basis of upper (T^+, black curve) and lower resistive (T^-, red curve) AFM ordering temperatures. The T^+ transition is more pronounced in the lower pressure regime, i.e. below 5 GPa. The figure is taken and modified from–[56].

4.1.5. Infrared spectroscopy

The frequency–dependent reflectivity of EuB_6 is shown in Figure 4.7 for various temperatures as reported by L. Degiorgi et al [80]. The graph is extracted and digitalized from Figure 1 of reference–[80]. At 300 K, the reflectivity shows a steep decrease and approaches 15 % at 1300 cm^{-1}, which is interpreted as a plasma edge type behaviour of EuB_6. The corresponding frequency at the minimum of the reflectivity level can be considered as an unscreened plasma frequency [80].

At 100 K, the plasma edge shows small shift toward lower frequencies (red shift) as shown Figure 4.7. The reflectivity shows temperature independence above 2500 cm^{-1} at 300 K and 100 K, where the spectra lie on top of each other. However, at 12 K the plasma edge shows a drastic shift towards higher frequencies (blue shift), i.e. around 2000 cm^{-1}, which corresponds to the ferromagnetic ordering of EuB_6. Upon further cooling down to 6 K the plasma edge

shifts to 2600 cm^{-1}. Furthermore, the reflectivity at 12 K and 6 K show temperature independence above 5000 cm^{-1} [80].

Figure 4.8 shows the frequency–dependent behaviour of the phonon mode at 848 cm^{-1} which corresponds to the vibration in the boron cage. Its intensity increases as the temperature decreases, while at the onset of magnetic ordering, it starts to shift to the higher frequencies. The phonon mode at 145 cm^{-1} (see Figure 4.8 (a)) is due to the related motion between the Eu ion and the boron cage, which stays at the same frequency but with reduced oscillator strength.

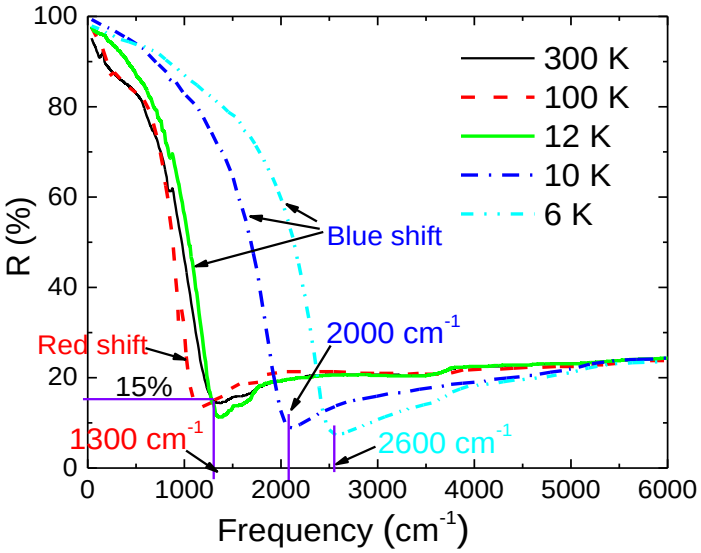

Figure 4.7. Reflectivity of EuB_6 at various temperatures as reported by L. Degiorgi et al [80].

The real part of the optical conductivity is shown in Figure 4.9 (a) which is extracted by J. H. Kim et al [79] by simultaneous fitting of reflectivity $R(\omega)$ and dielectric function using Kramers–Kronig constrained variational–fitting method [82]. It shows an increased metallization with decreasing temperature as represented by arrows. For extracting the plasma frequency, the real part of the optical conductivity was integrated up to the limit of ω_c = 0.33 eV as given by the expression; $S(\Omega) = 8\int_0^{\omega_c} \sigma_1(\omega)\, d\omega$, where the spectral weight of Drude component is proportional to the square of the plasma frequency. The calculated value of the plasma frequency by Kim et al [79] at room temperature is around 3300 cm^{-1}, which is higher than the value of 1750 cm^{-1} as reported by L. Degiorgi et al [80].

L. Degiorgi et al [80] use only reflectivity data and the Lorentz–Drude model for extracting the plasma frequency (ω_p) as a function of temperature, which is shown in Figure 4.9 (b). The plasma frequency shows a smooth increase until 15 K and start to increase steeply below 14 K, which is related to the second magnetic transition. For temperatures below 8 K, the

plasma frequencies reach to almost constant values. The authors also reported a substantial decrease in scattering rate at these magnetic transitions and attributed them to the reduced spin flip scattering [80].

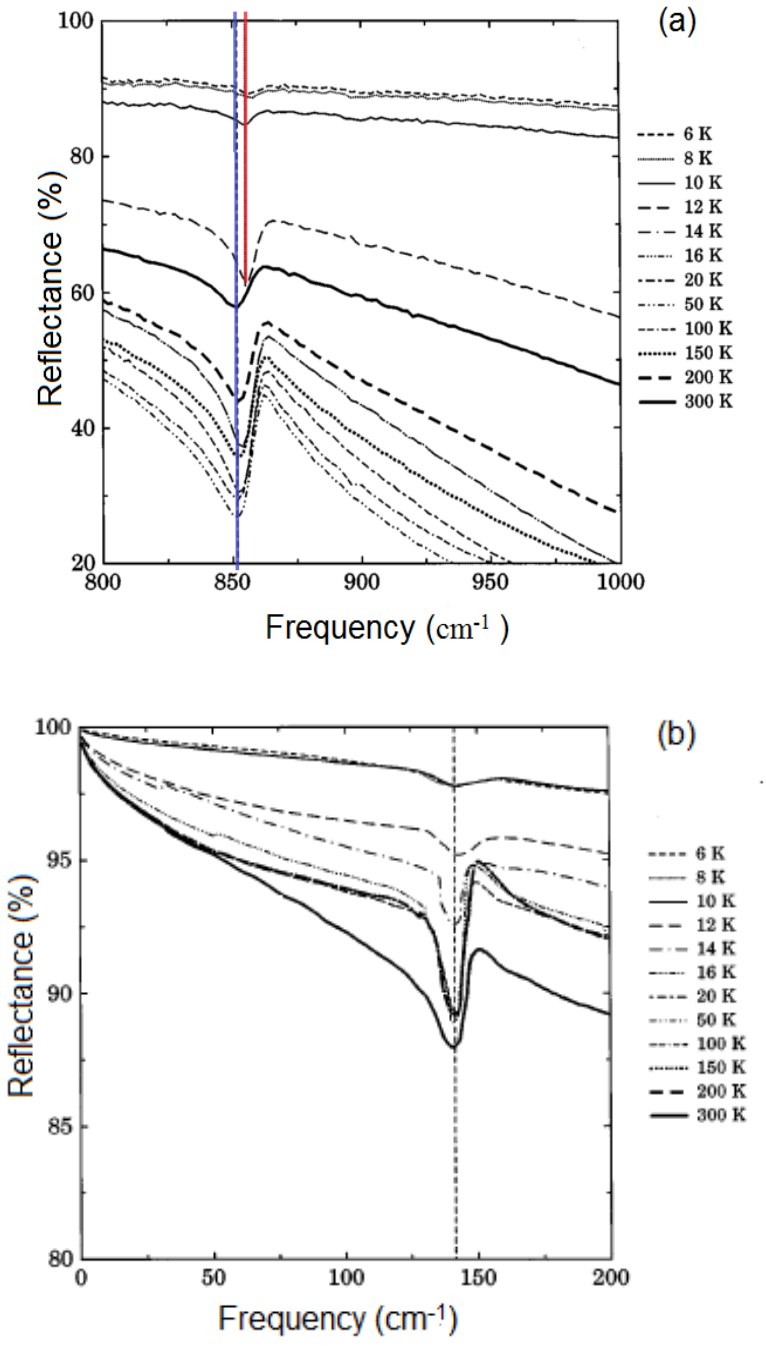

Figure 4.8. Temperature–dependent behaviour of phonon modes for EuB_6 as reported by L. Degiorgi et al [80]. (a) Phonon mode at 850 cm^{-1} [80]. Phonon mode at 145 cm^{-1}. The figures are adopted and modified from-[80].

Since the onset of the magnetic transition appears as a substantial increase in the plasma frequency, either the charge carrier concentration is increased or the effective mass of the charge carriers is reduced due to the interaction with magnetic moments. Y. Okimoto et al [83] shows that the square of the plasma frequency is quantitatively related to the square of the magnetization and they attribute it to moment polarization in the mean field approximation.

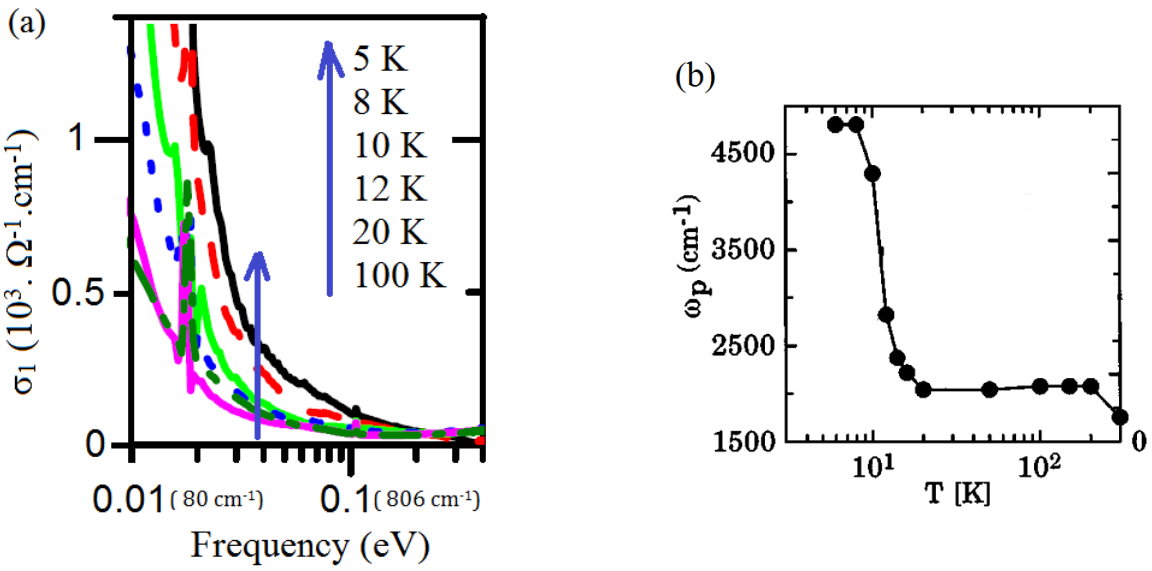

Figure 4.9. (a) Real part of the optical conductivity for EuB_6 at various temperatures and ambient pressure as reported by J. H. Kim et al [79]. (b) Temperature–dependent behaviour of the plasma frequency for EuB_6 as reported by L. Degiorgi et al [80]. The figures are taken and modified from-[80].

The infrared measurements under pressure for the EuB_6 were carried so far rarely but according to the theoretical calculations reported by Kunes et al [81] and Kim et al [79], there is a large blue shift expected in the plasma edge when high pressure will be applied. The blue shift is expected in both the paramagnetic and ferromagnetic states, while the magnetic blue shift is expected to be decreased with increasing pressures as explained in section 4.2.4. Therefore, high–pressure infrared experiments were carried out in the present research work in order to understand the electronics properties of EuB_6.

4.2. Experimental results and discussion for EuB_6

In this part of the thesis, the effect of high–pressure (0–7.7 GPa) was studied on the plasma edge by measuring the near–normal incident reflectivity for the single crystal of EuB_6 at various temperature (300–5 K). The experimental results and discussions will be presented in this section.

4.2.1. Pressure cycles

Figure 4.10 shows the infrared reflectivity of EuB_6 at 0.1 GPa for various measured temperatures. The high frequency part, i.e. above 3000 cm^{-1} for all spectra lies exactly on the top of each other, indicating no dependence on pressure or temperature. The plasma edge (see section 4.1.5 for explanation) drastically shifts to higher frequencies (blue shift) at 12 K and 5 K, which corresponds to the ferromagnetic ordering of EuB_6.

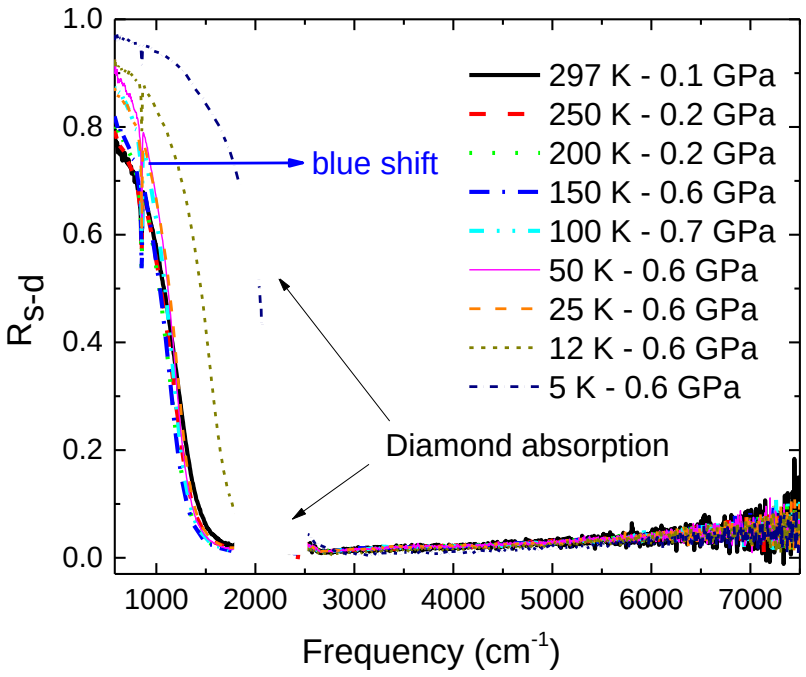

Figure 4.10. Pressure cycle–1, shows the infrared reflectivity (R_{s-d}) of EuB_6 at various temperatures, where the diamond multi–phonon absorption around 2000 cm^{-1} is cut from the spectra. The starting pressure at 297 K was 0.1 GPa. The large blue shift of the plasma edge is observed at 12 K and 5 K due to the ferromagnetic ordering.

In Figure 4.11, the magnification of Figure 4.10 is shown in the low frequency regime, where the red shift of the plasma edge is clearly obvious at 250 K, 200 K and 150 K, which turns out as a blue shift below 150 K. In fact, the blue shift is small even at 25 K compare to the shift of the spectra at 12 K and 5 K which clearly differentiate the paramagnetic and ferromagnetic states of EuB_6.

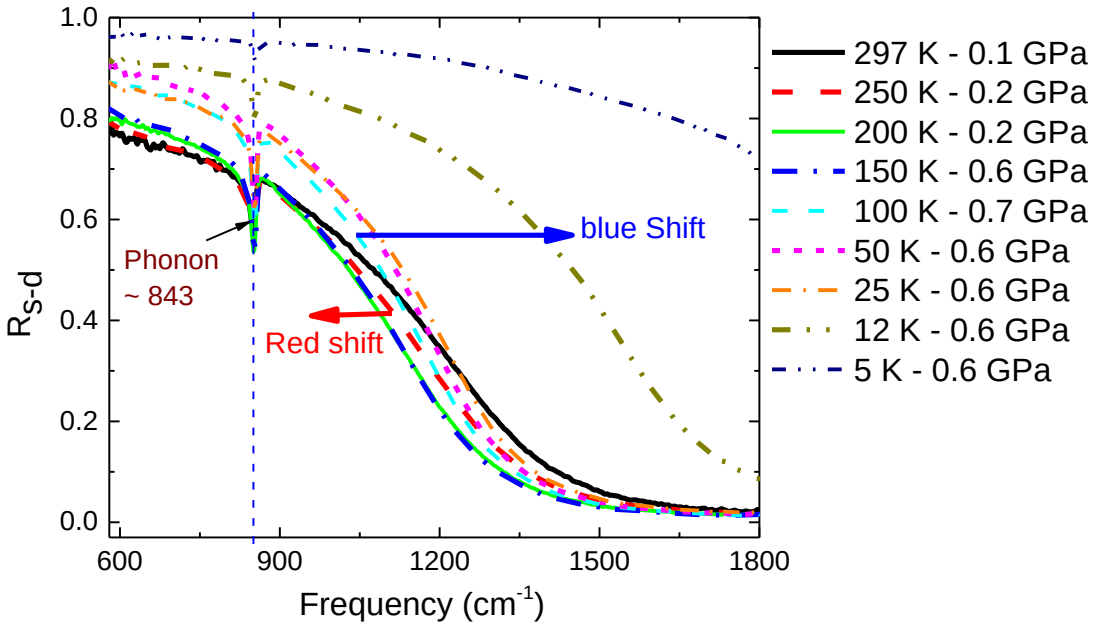

Figure 4.11. Magnification of Figure 4.10 in the low frequency regime, where the temperature dependent of reflectivity (R_{s-d}) is clearly obvious. Starting from room temperature, the spectra show red shift with lowering temperature up to 150 K while further decrease in temperature, increase the reflectivity level and exhibit blue shift.

Figure 4.12 shows the temperature–dependent behaviour of the phonon mode at 843 cm^{-1} for the starting pressure of 0.1 GPa, which shows a shift toward higher frequencies with decreasing temperature. The total frequency shift from 297 K to 5 K is around 10 cm^{-1}. The oscillator strength of the phonon mode increases at 200 K and 100 K which starts to decrease for temperatures ≤ 25 K. The cycle–1 shows a remarkable consistency with the temperature–dependent measurements as reported by L. Degiorgi et al [80] at ambient pressure. The extracted peak position of the phonon mode (see Figure 4.22) from the Lorentz–Drude fits is presented in the section 4.2.3.

As the pressure was increased to 0.5 GPa, the blue shift was started for temperatures ≤ 150 K while the red shift exists at 200 K (see Figure 0.5 in appendix) and is completely suppressed

with further increase in pressure. In addition, the blue shift of the plasma edge in the paramagnetic phase was increased considerably due to the increased pressure as compare to the first cycle (see Figure 4.11).

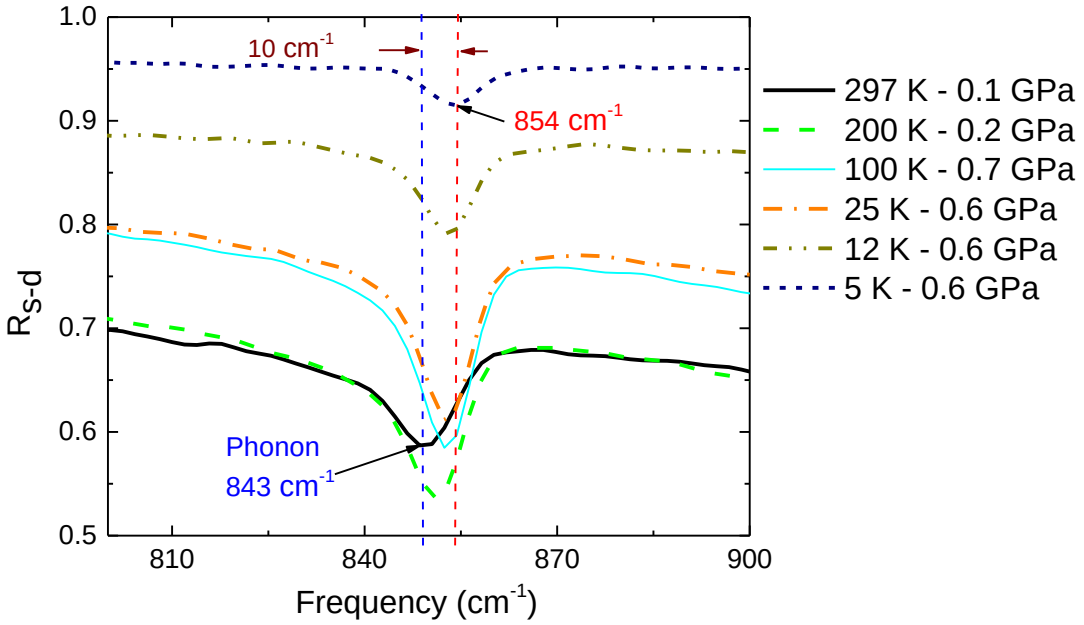

Figure 4.12. Temperature–dependent behaviour of the phonon mode at 843 cm^{-1} of EuB_6 at starting pressure of 0.1 GPa at room temperature. The peak position shifts to higher frequencies and the oscillator strength decreases with decreasing temperature.

In Figure 4.13 the infrared reflectivity at 2.9 GPa is shown for various temperatures, which were measured in pressure cycle–5. The pressure was increased to 5.4 GPa at 5 K due to the pressure jump inside the cell as described in section 2.2.6. The situation will become clear when the spectra will be discussed for the constant temperatures at various pressures as presented in section 4.2.2. The blue shift of the plasma edge in paramagnetic phase approaches to higher values of around 3000 cm^{-1}. The high frequency parts, i.e. above 4500 cm^{-1} show no dependence on pressure or temperature.

Figure 4.13 (b) shows the infrared reflectivity at 4.0 GPa for EuB_6 as measured in pressure cycle–7. The pressure was increased to 7 GPa at 150 K, which was further increased to 7.7 GPa at 5 K. It is obvious that the shift of the plasma edge reaches a saturation limit, i.e. at 5000 cm^{-1}. The high frequency part, i.e. above 6000 cm^{-1} shows no pressure or temperature dependence, while the phonon mode at 848 cm^{-1} is completely screened out for all measured temperatures.

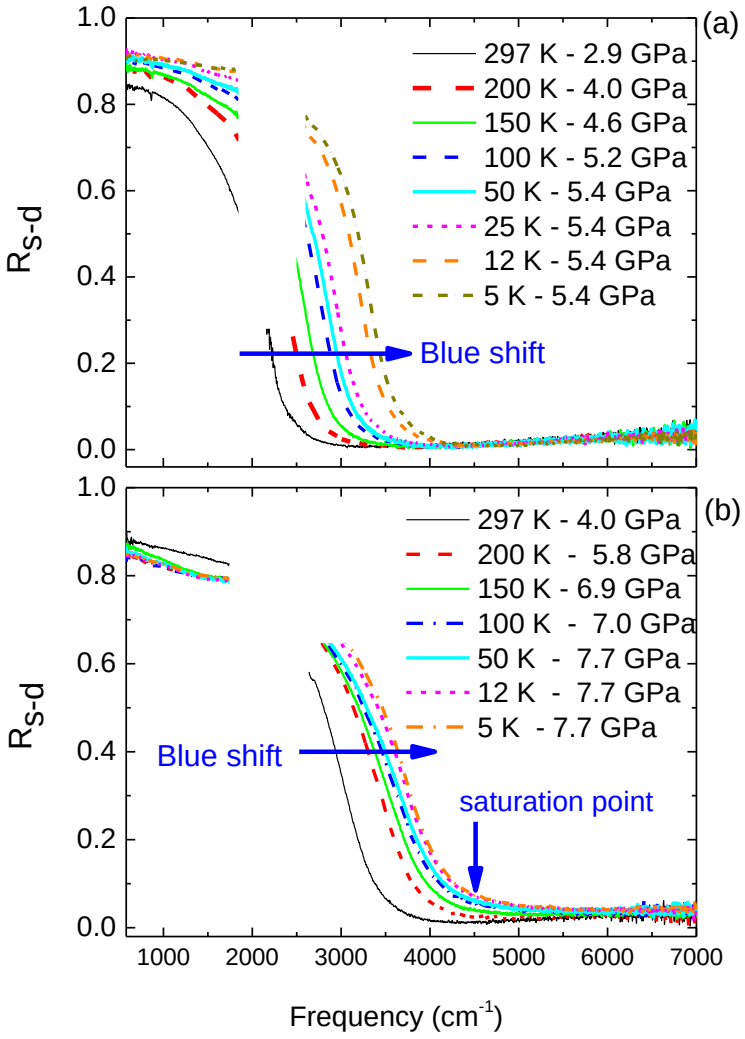

Figure 4.13. Infrared reflectivity (R_{s-d}) of EuB_6 at different temperatures and various pressures. The diamond multi–phonon absorption around 2000 cm^{-1} is cut from the spectra. (a) Pressure cycle–5, where the starting pressure at 297 K was 2.9 GPa, which jumped to 5.4 GPa at 5 K. (b) Pressure cycle–7, with the starting pressure of 4.0 GPa, where the blue shift in plasma edge reached to it saturation limit for all low temperatures, i.e. around 4500 cm^{-1}.

To check the reversibility**,** two releasing pressure cycles were measured, one at 1.0 GPa (Figure 4.14 (a)) and another at 0.4 GPa (Figure 4.14 (b)). The highest pressure from the seventh cycle was 7.7 GPa at 10 K. The pressure was released slowly in small steps, in order to avoid any leakage in the gasket. The reflectivity ≥ 3500 cm^{-1} lies on top of each other indicating no pressure or temperature dependence.

For the first releasing cycle at 1.0 GPa, the reversibility in frequency position of the plasma edge is smaller at 12 K compared to the spectra at 297 K as shown in Figure 4.14 (a). The red shift is completely suppressed (see Figure 0.7 (a) in appendix), where the plasma edge shows a clear shift towards higher frequencies at 250 K and 200 K. The phonon mode is recovered at 853 cm^{-1} compared to its initial position at 855 cm^{-1} for 200 K.

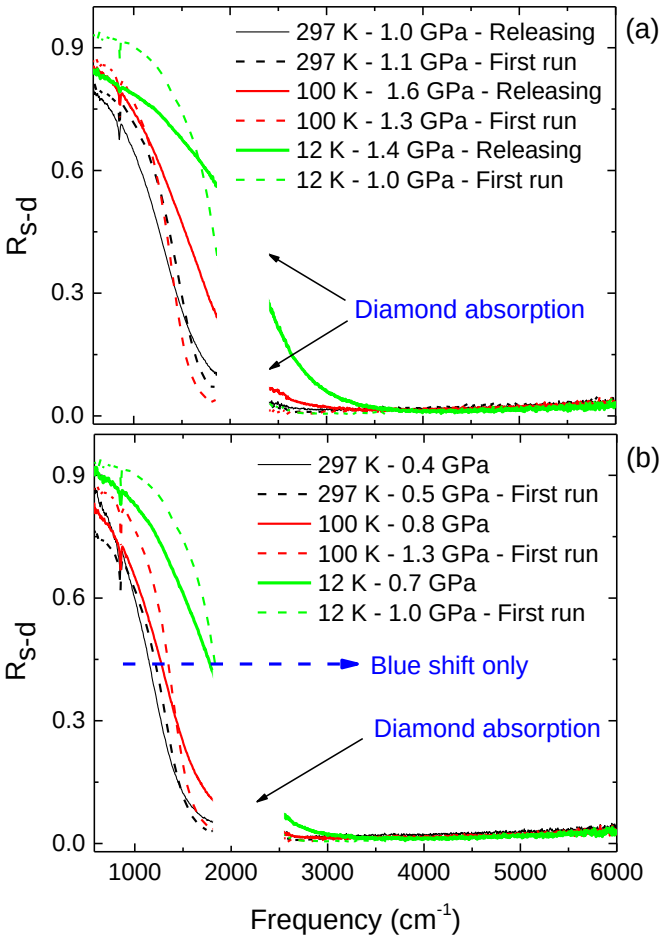

Figure 4.14. Releasing pressure cycles for EuB_6, shows the infrared reflectivity at 297 K, 100 K and 12 K. The spectra from the first run are shown with dashed lines. The diamond multi–phonon absorption around 2000 cm^{-1} is cut from the spectra. (a) First releasing cycle at 1.0 GPa. (b) Second releasing cycle at 0.4 GPa.

For the second releasing cycle at 0.4 GPa, the reversibility of the plasma edge frequency position at 12 K is increased (see Figure 4.14 (b)) compare to the first releasing cycle (see Figure 4.14). However, the red shift of plasma edge is not observed and the spectrum at 250 K shows a clear shift toward higher frequencies (see Figure 0.7 (b) in appendix). The

intensity of the phonon mode increases and is recovered at 852 cm^{-1} instead of 853 cm^{-1} at 150 K.

4.2.2. Temperature cycles

The spectra at each temperature with various pressures are plotted and presented in the following section in order to observe the effect of pressure at each temperature.

Figure 4.15 (a), shows the reflectivity of EuB_6 at 297 K under various measured pressures. The plasma edge shows a drastic shift toward higher frequencies with increasing pressure.

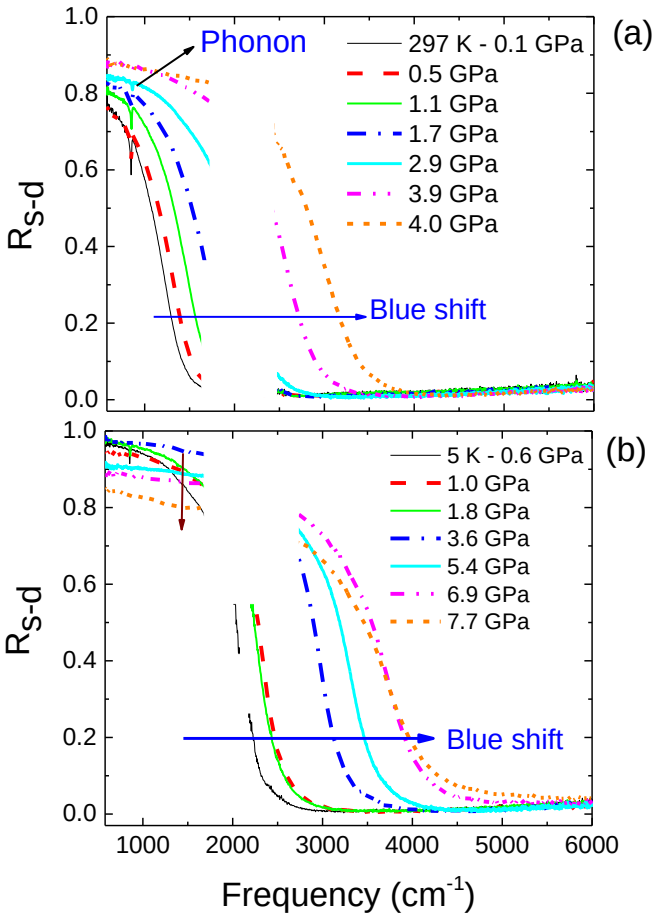

Figure 4.15. Reflectivity (R_{s-d}) of EuB_6 at (a) 297 K and (b) 5 K, for various measured pressures. The diamond multi-phonon absorption around 2000 cm^{-1} is cut from the spectra.

In Figure 4.15 (b) the reflectivity of EuB_6 is shown at 5 K, which belongs to the ferromagnetic phase of EuB_6. Due to the ferromagnetic ordering the plasma edge is already at

higher frequency position, i.e. 2500 cm^{-1} at 0.6 GPa, which starts to shift to higher frequencies with increasing pressure and reaches to it saturation limit of 5000 cm^{-1} at 7.7 GPa. The reflectivity level decreases slightly below 3000 cm^{-1}, for pressures ≥ 3.6 GPa. The behaviour is similar to the effect of carbon doping (Figure 4.3) on EuB_6 as explained in section 4.1.3.

4.2.3. Analysis and interpretations

The Lorentz–Drude model was used to fit the measured LTHP spectra. The data above 7,000–50,000cm^{-1} was extracted from J. H. Kim et al [78] and merged with the measured data, as shown in Figure 4.16 (a). One Drude term and six harmonic oscillators were used to fit the spectra at 297 K and 0.1 GPa. To fit the higher pressures at 297 K, only the Drude term, *D1* and harmonic oscillators, *L1* and *L2* were manipulated, while the high frequency components were kept constant.

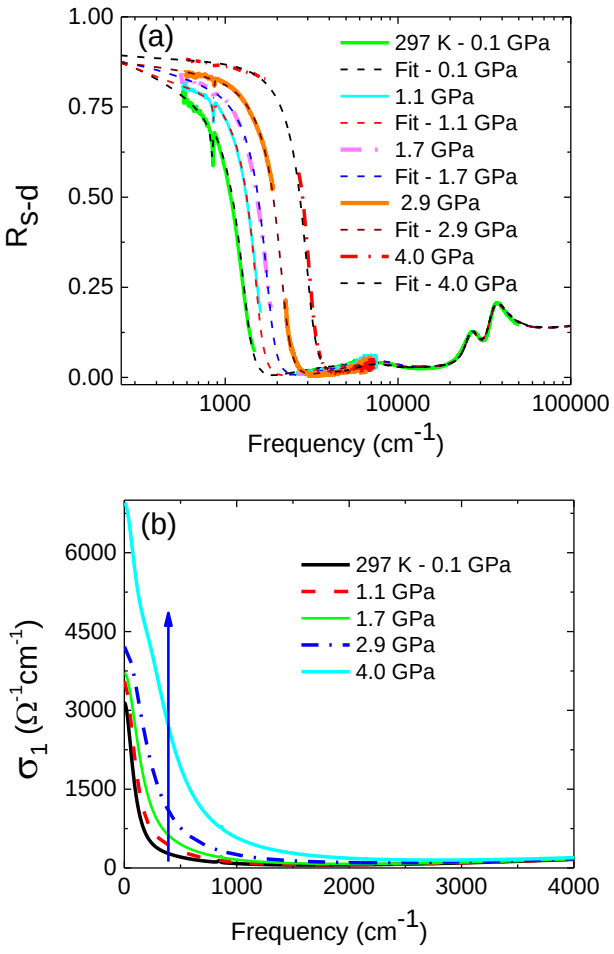

Figure 4.16. (a) Reflectivity of EuB_6 at 297 K for various measured pressures, along with the fitting curves shown with dashed lines. (b) Extracted real part of the optical conductivity at 297 K for various measured pressures

The extracted real part of the optical conductivity at 297 K for various pressures is shown in Figure 4.16 (b) which shows an increased metallic character of the material with increasing pressure. The pressure dependence of the fitting components at 0.1 GPa, 2.9 GPa and 4.0 GPa are shown in Figure 4.17, which shows a substantial increase in the spectral weight of the Drude component with increasing pressure. The phonon mode (*L2*) is visible at low pressures (see Figure 4.17 (a and b)) but completely screened out at 4 GPa (see Figure 4.17 (c)).

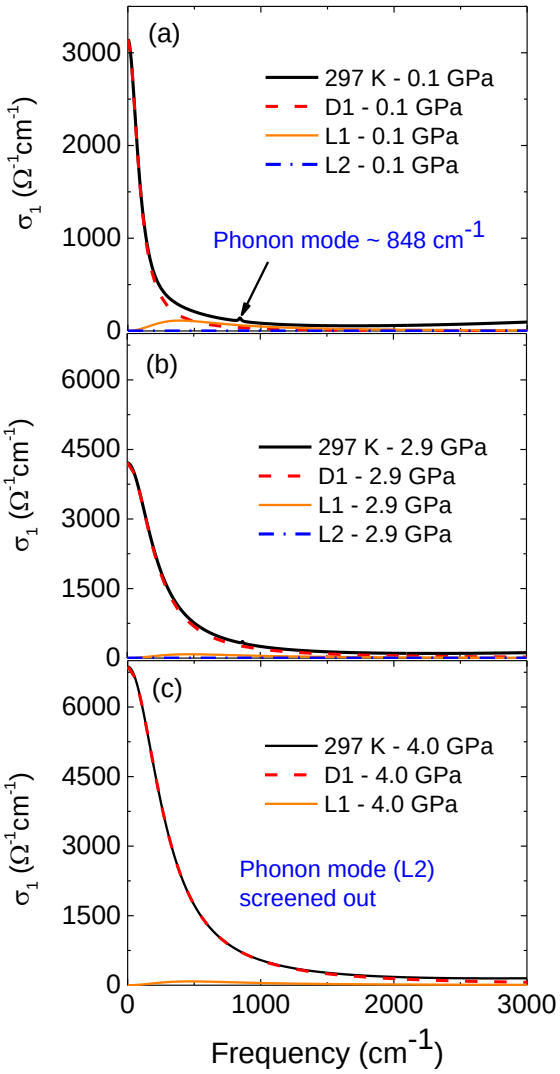

Figure 4.17. Real part of the optical conductivity at 297 for EuB_6 at various pressures along with the fitting contributions. D1 is the Drude term and L1, L2 are harmonic oscillators. L2 represents the sharp phonon mode at 848 cm^{-1}. (a) At 0.1 GPa, (b) 2.9 GPa and (c) 4.0 GPa.

Three different methods were used to calculate the plasma frequencies. In method–1, the plasma frequency was calculated from the spectral weight of the Drude component (*D1*) which was obtained from the Lorentz–Drude fits as explained in sections 2.4 and 3.3.3. The calculated values of plasma frequencies are plotted in Figure 4.20 (a).

In Figure 4.18, the method–2 for calculation of the plasma frequency is illustrated, where the first order derivative of the fitted curves of reflectivity are shown at various pressures. The

minima of the peak position are taken as plasma frequencies. Meanwhile, it is obvious that the intensity of the peak decreases with increasing pressure.

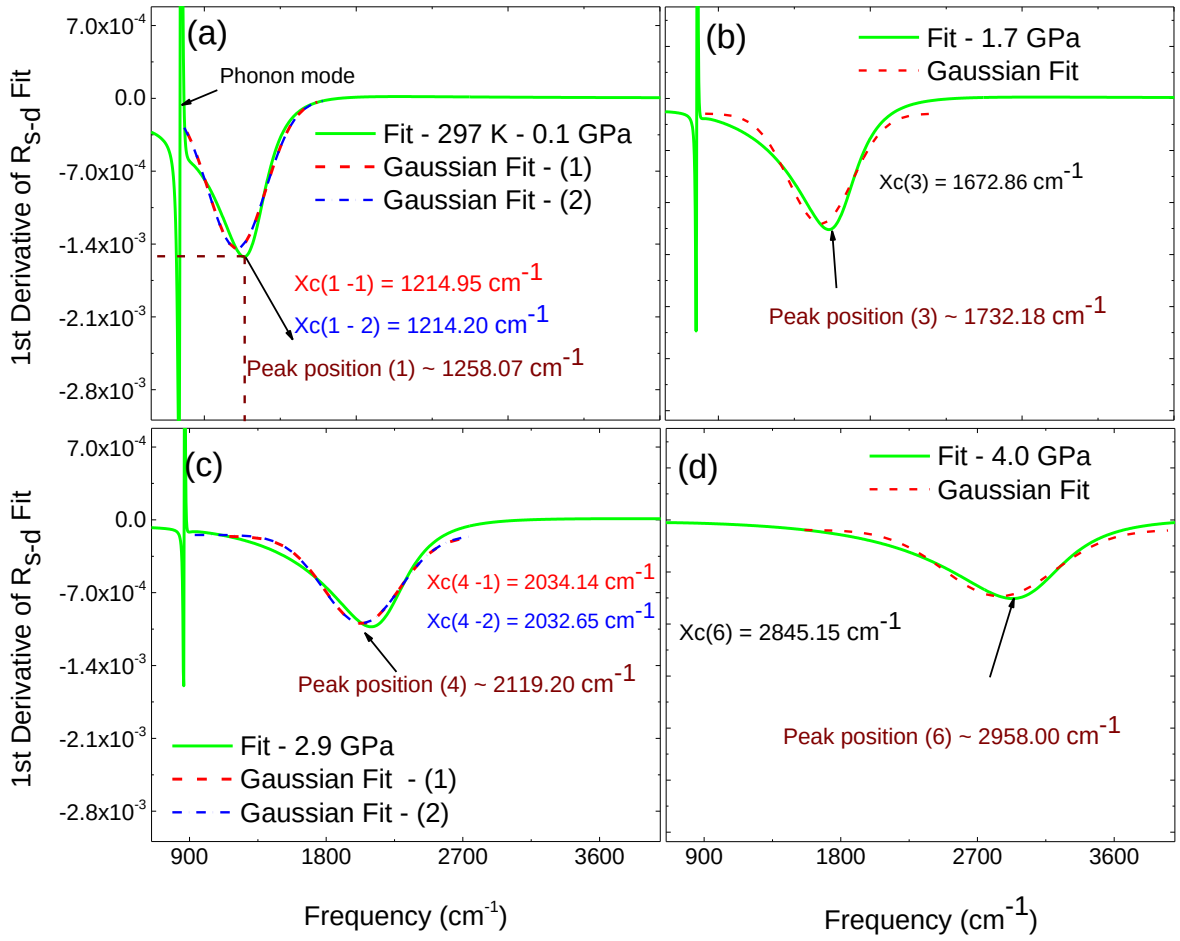

Figure 4.18. Quantitative extraction of the plasma edge at 297 K, for EuB_6 by taking the first order derivative of the fitting curves as explained in method–2. The minima of the peak were taken as the plasma frequency. The Gaussian model was also fitted to the peak. The central frequency (Xc) of the Gaussian was taken as a plasma frequency. The peak intensity gets smaller and broader with increasing pressure. The error bar due to the interval limits is within few wave numbers, i.e. ~ 2 cm^{-1}. (a) At 0.1 GPa, the minimum of the peak position of the first order derivative is 2119.20 cm^{-1}. The two fitted Gaussians are represented by red and blue dashed lines, with central frequencies of Xc(1-1) ~ 1214.95 cm^{-1} and Xc(1-2) ~ 1214.20 cm^{-1}. (b) At 1.7 GPa (c) At 2.9 GPa. (d) At 4.0 GPa.

In addition, a Gaussian model was also fitted to the first order derivative and the central frequency (*Xc*) of the Gaussian fit was taken as a plasma frequency (see Figure 4.18). In fact,

the centre frequency (*Xc*) of Gaussian can be affected by the selection of interval limits, as well as a mismatch in peak fitting. The error bar was within a few wavenumbers for the calculated values of the plasma frequencies: i.e. *X(1–1), X(1–2)* and *X(4–1), X(4–2)* as shown in Figure 4.18 (a and c). The calculated plasma frequencies are plotted in Figure 4.20 (b) where both values, i.e. from the minima of the peak position and from the Gaussian fit show almost similar values and trend.

In method–3, the $\mathcal{E}_1$ (dielectric function) was extracted from the Lorentz–Drude fit, and the zero–crossing of $\mathcal{E}_1$ was taken as a plasma frequency as illustrated in Figure 4.19. The value of the plasma frequency calculated from ε_1 (zero–crossing) was based on an approximate formula, i.e. $\mathcal{E}_1 = 1 - \frac{\omega^2}{\omega_p^2}$, only if $\omega >> \omega_p$ which appears as position sensitive to the plasma edge, when calculated at 100 K and 5 K. The extracted values are plotted in Figure 4.20 (c).

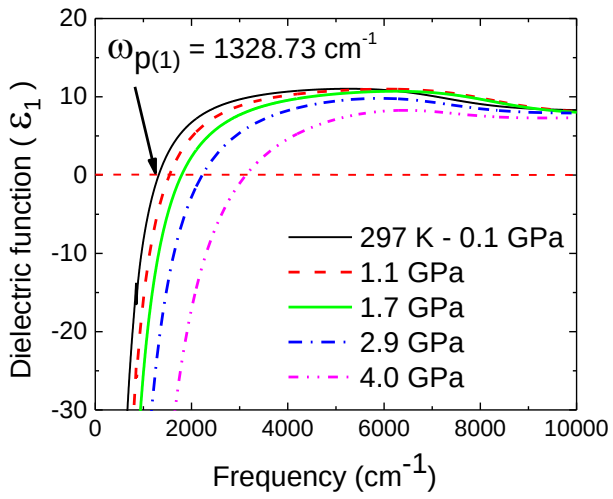

Figure 4.19. Real part of the dielectric function ($\mathcal{E}_1$) for EuB_6 at 297 K for various measured pressures. The zero–crossing was taken as a plasma frequency, as explained in method–3.

The plasma frequency calculated from the spectral weight of the Drude component (see Figure 4.20 (a)) is 1702.66 cm^{-1} at "297 K - 0.1 GPa". The value is consistent with the value reported by L. Degiorgi et al [80] under ambient conditions, i.e. 1750 cm^{-1}. In fact, Kim et al [79, 78] reported higher values of plasma frequency in the paramagnetic state, i.e. 3300 cm^{-1}, but they extracted it by simultaneous fitting of reflectivity and dielectric function.

In order to fit the pressure–dependent data at 100 K and 5 K, the fitting model of 297 K was used. The high frequency contributions, i.e. ≥ 7,000 cm^{-1} were kept constant throughout the fitting process. The plasma frequencies were calculated by using three different methods and plotted in Figure 4.20.

Figure 4.20 (a) shows the plasma frequencies as a function of pressure; calculated from the spectral weight of Drude component (*D1*), where the plasma frequencies shows fast increasing trend below 3.5 GPa. The trend becomes smaller above 3.5 GPa at 297 K and 100 K, while at 5 K the plasma frequency starts to decrease slightly above 5.5 GPa. The effect was observed as a drop in reflectivity level at 5 K for pressures ≥ 5.4 GPa (see Figure 4.15 (b)) which appears as a decrease in spectral weight of the Drude component and it is similar to the behaviour of carbon doped $EuB_{6-x}B_x$ for the higher doping concentrations as explained in section 4.1.3.

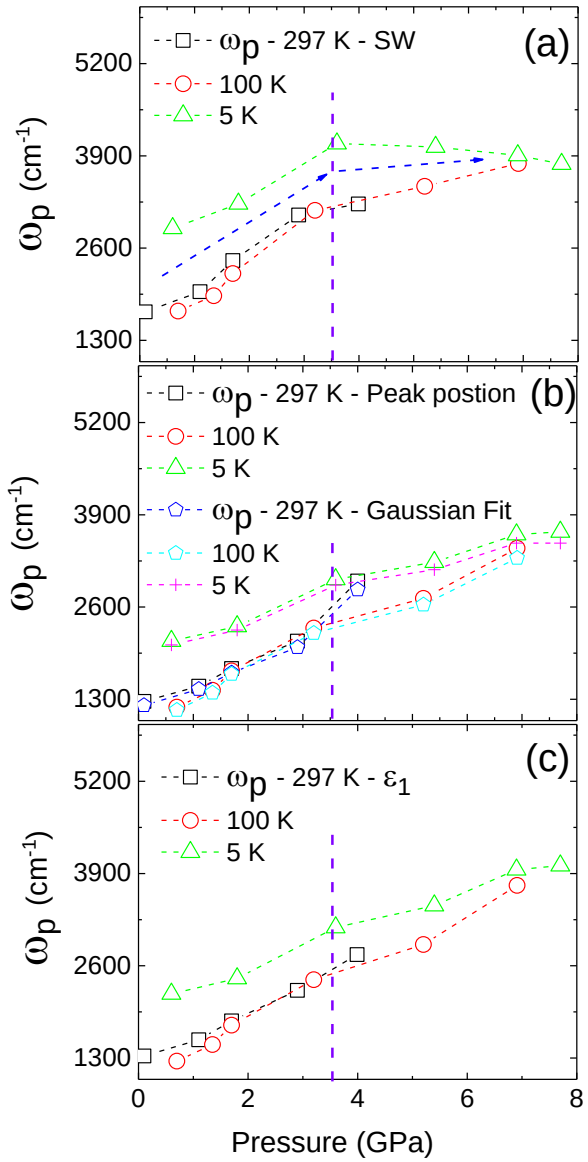

Figure 4.20. Plasma frequencies for EuB_6 as a function of pressure, at 297 K, 100 K and 5 K calculated by using three different methods. (a) Method–1, by using spectral weight of the Drude component. (b) Method–2, where the square symbols represent the plasma frequencies calculated by taking the minima of peak position. The star symbols represent the plasma frequencies calculated by fitting the Gaussian to the peak. (c) Method–3, where the zero–crossing of the ε_1 was taken as a plasma frequency.

Figure 4.20 (b) shows the plasma frequencies as a function of pressure calculated by method–2, where both values are shown, i.e. minima of the peak position and the centre frequency of Gaussian fits. Since the method–2, is position sensitive to the plasma edge

therefore, a decreasing trend in plasma frequency at 5 K for pressures ≥ 5.5 GPa cannot be observed. Similarly, the effect cannot be observed in Figure 4.20 (c) where the pressure–dependent plasma frequencies calculated from method–3, are shown.

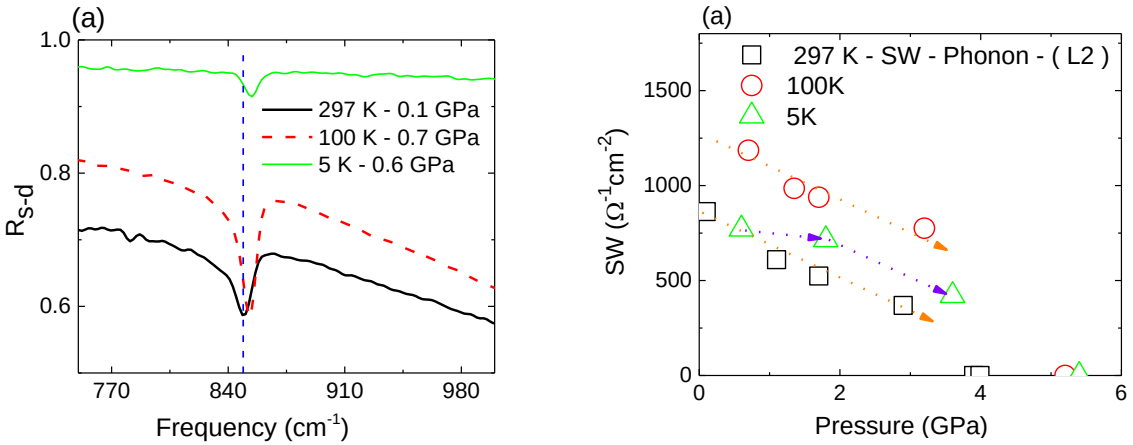

Figure 4.21. (a) Temperature–dependent behaviour of phonon mode (L2) for EuB_6 at lowest measured pressure. (b) Pressure–dependent spectral weight of L2, calculated from the Lorentz–Drude fit at 297 K, 100 K and 5 K.

The behaviour of the phonon mode at 850 cm^{-1} as a function of temperature is shown in Figure 4.21 (a). The mode shows strengthening when cooled down from 297 K to 100 K while it becomes weaker at 5 K. A similar effect was observed in the spectral weight plot as shown in Figure 4.21 (b). Moreover, the mode (*L2*) shows hardening with application of pressure and completely screened out above 3.5 GPa as shown in Figure 4.22. The behaviour is consistent with the earlier temperature–dependent reflectivity measurement as reported by L. Degiorgi et al [80].

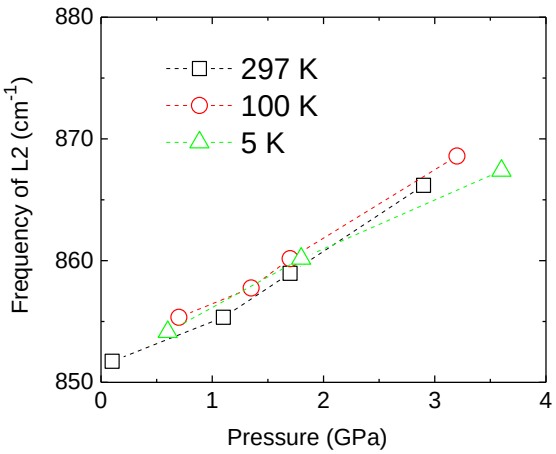

Figure 4.22. Pressure–dependence of the peak position of phonon mode (L2) at 297 K, 100 K and 5 K. The mode hardens with increasing pressure and cannot observe above 3.5 GPa.

4.2.4. Discussion

Two kinds of blue shifts are expected in the plasma frequency (ω_p) for EuB_6, one is due to pressure and the second is due to the magnetic ordering with temperature. The magnetic blue shift can be quantified, by taking the ratio of plasma frequencies (ω_p) in ferromagnetic (FM) to paramagnetic (PM) states, i.e. $\omega_{p,\ FM}$ / $\omega_{p,\ PM}$. The plasma frequency above magnetic transition temperature (T_c), i.e. 100 K can be taken as $\omega_{p,\ PM}$, and the plasma frequency in ferromagnetic saturation, i.e. 5 K can be taken as $\omega_{p,\ FM}$. It is predicted theoretically, that both $\omega_{p,\ FM}$ and $\omega_{p,\ PM}$ will increase with application of pressure but the magnetic blue shift (the ratio of $\omega_{p,\ FM}$/ $\omega_{p,\ PM}$) will diminish with increasing pressure [79, 81].

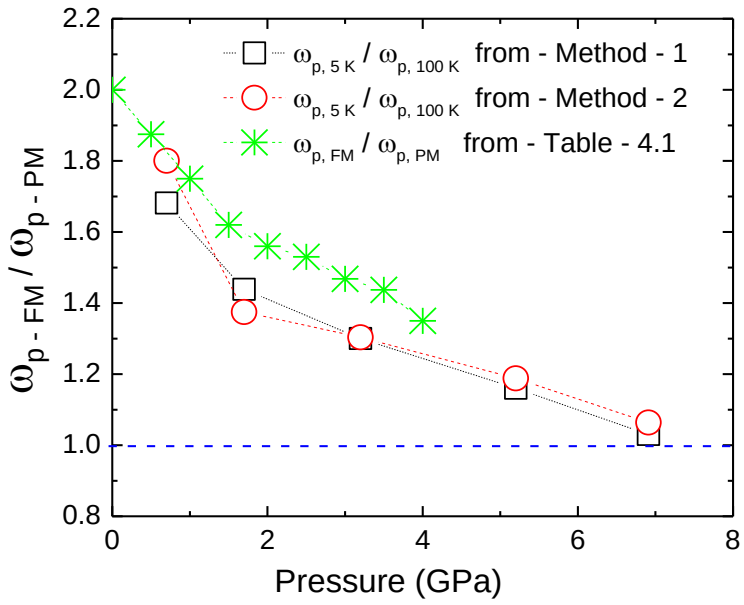

Figure 4.23. Calculated ratio of plasma frequencies in ferromagnetic to paramagnetic states, i.e. ($\omega_{p,\ 5\ K}$) / ($\omega_{p,\ 100\ K}$) for EuB_6 calculated by method–1 (black squares) and method–2 (red circles). The extracted ratio of ($\omega_{p,\ FM}$) / ($\omega_{p,\ PM}$) from Table–4.1 is plotted in the same graph with the green colour.

In order to quantify the above mentioned phenomena, the ratios of plasma frequencies at 5 K, $\omega_{p,\ 5\ K}$, and at 100 K, $\omega_{p,\ 100\ K}$, were calculated for method–1 and method–2 and plotted in Figure 4.23. The calculated $\omega_{p,\ 5\ K}$ / $\omega_{p,\ 100\ K}$ ratio at 0.7 GPa was 1.6 (method–1) and 1.8 (method–2). From the data by L. Degiorgi et al [80] the $\omega_{p,\ FM}$ / $\omega_{p,\ PM}$ ratio is 2.25, while Kim et al [79] reported a ratio of 2.1 from their temperature dependent measurements [79, 81].

Kunes et al [81] performed LDA+U (Local density approximation) calculation for EuB_6, where they presented, valance band (VB)/conduction (CB) overlaps (Δ) (see section 4.1.2) as a function of unit cell volume, as shown in Figure 4.24. These calculations were used by Kim et al [79] in order to fit their $\omega_{p,\,FM} / \omega_{p,\,AFM}$ ratio with VB/CB overlap (Δ) as illustrated in Figure 4.25. Since it is known that LDA overestimates the absolute values of band overlaps, the values were shifted by a factor of 0.35 eV to match the experimental and theoretical results.

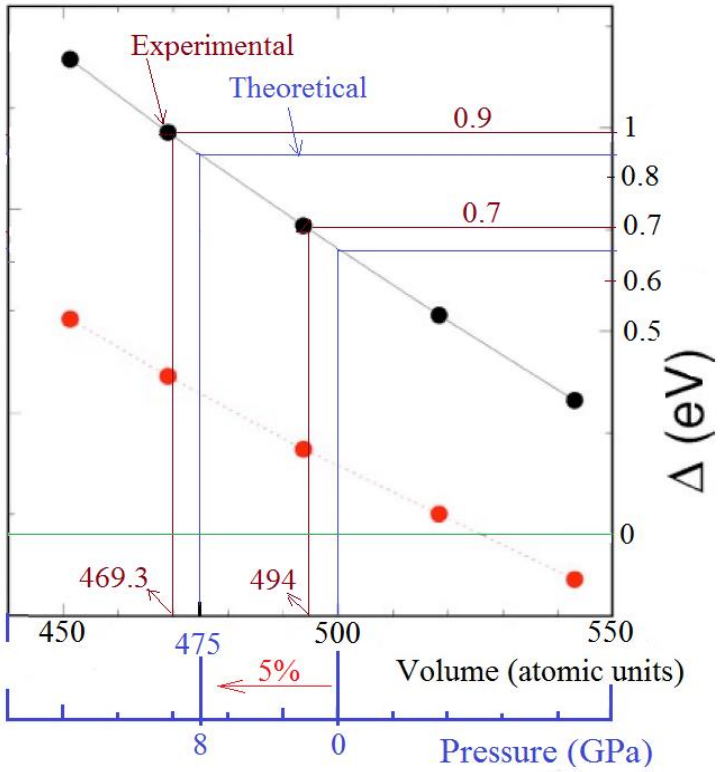

Figure 4.24. Valance band (VB)/conduction (CB) overlap (Δ) as a function of unit cell volume and pressure as reported by J. Kunes et al [81]. The black curve shows the spin–up and red curve shows the spin–down carrier contributions. Theoretical value of unit cell volume is 500 a.u, while the experimental value at ambient conditions is 494 a.u. The figure is adopted and modified from the reference - [81].

Figure 4.24 shows the VB/CB overlap (Δ) as function of unit cell volume, where the experimental and theoretical volumes for EuB_6 are shown. The horizontal axis is translated into pressure units by assuming the bulk modulus (*B*) of 160 GPa and pressure up to 8 GPa, which gives the decrease in unit cell volume by 5 %, i.e. 8 / 160 = 0.05. Thus, the value of the

experimental band overlap (Δ) for the spin–up majority carriers per GPa can be calculated as ≈ (*V* at 494 a.u) – (*V* at 469.3 a.u) ≈ 0.9 – 0.7 ≈ 0.2 eV / 8 GPa ≈ 0.02 eV / GPa.

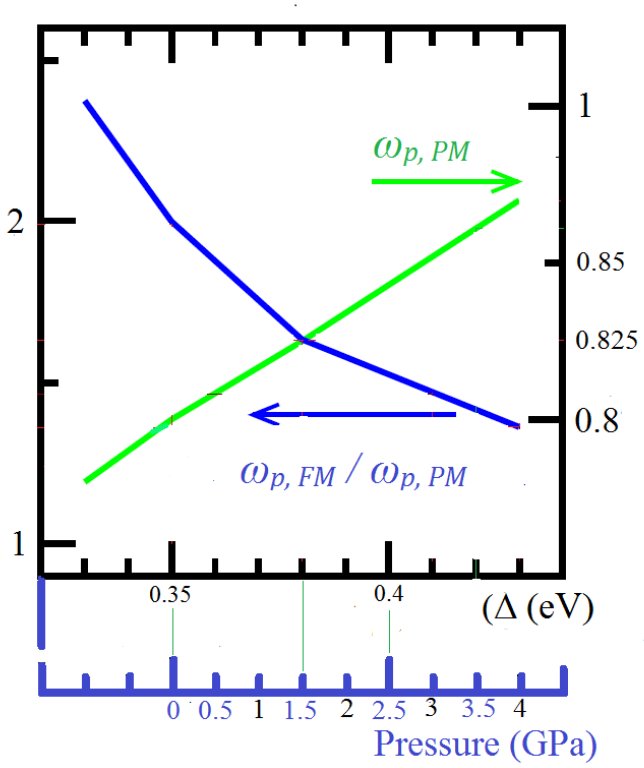

Figure 4.25. Theoretical values of $\omega_{p,\,FM}/\omega_{p,\,PM}$ ratio and $\omega_{p,\,FM}$ as a function of valance band (VB)/conduction band (CB) overlap (Δ) and pressure, as reported by J. H. Kim [79] et al. The figure is adopted and modified from the reference - [79].

The above information is used to transform the horizontal axis of Figure 4.25 into pressure units. The value of VB/CB overlap (Δ) at 0.35 eV is set equal to 0 GPa and presented in the form of Table 4.1. The $\omega_{p,\,FM}$ / $\omega_{p,\,PM}$ ratio from Table 4.1, is plotted (green stars) in Figure 4.23, along with experimentally calculated $\omega_{p,\,5K}$ / $\omega_{p,\,100K}$ ratio from the LTHP data. It shows a slightly sublinear behaviour below 2.5 GPa and becomes almost linear above 3.0 GPa, which is a remarkable consistency with the theoretical calculations as reported by Kunes et al [81] and Kim et al [79].

The effect of pressure is only approximated by shifting of the bands. In fact, it would be the most dominant effect on the band structure of EuB_6, if only plasma frequency will be considered. Indeed, high pressure also affects the other parameters, such as bands broadening or increased exchange splitting, which were not taken into account in the above mentioned studies [79, 81].

Table 4.1. Extracted parameters from calculations by Kunes et al [81] and Kim et al [79], for VB/CB overlap (Δ), $\omega_{p,FM}$ and $\omega_{p,FM} / \omega_{p,PM}$ ratio for ten different pressures.

S. No.	Pressure (GPa)	Δ (eV)	$\omega_{p,PM}$ (eV)	$\omega_{p,FM}$ (eV)	$\omega_{p,FM} / \omega_{p,PM}$ ratio (eV)
1	0	0.35	0.4	0.8	2
2	0.5	0.36	0.433	0.81	1.875
3	1	0.37	0.467	0.818	1.75
4	1.5	0.38	0.509	0.825	1.62
5	2.0	0.39	0.532	0.831	1.56
6	2.5	0.4	0.57	0.88	1.53
7	3	0.41	0.585	0.859	1.468
8	3.5	0.4	0.604	0.868	1.437
9	4	0.43	0.70	0.94	1.35
10	5	0.45	-	-	-

4.3. Summary

In this chapter the infrared properties of EuB_6 were studies under high–pressure and low–temperatures. The red shift of the plasma edge was observed at 0.1 GPa and 0.5 GPa for temperatures ≥ 200 K which turns into a blue shift for pressures ≥ 1 GPa. In addition, a drastic blue shift in the plasma edge at 12 K and 5 K for pressures ≤ 1 GPa was also observed, which is consistent with the earlier temperature–dependent results as reported by L. Degiorgi et al [80] at ambient pressure.

The calculated plasma frequency at room temperature and 0.1 GPa is 1702.66 cm^{-1}, which is consistent with the L. Degiorgi et al [80] calculations at room temperature and ambient

pressure. The plasma frequency was increased substantially with application of high pressure; i.e. at 297 K, the value increased to 3221.75 cm^{-1} at 4 GPa, and at 100 K, it was increased to 3792.19 cm^{-1} at 6.9 GPa. This confirmed the phenomena of a large blue shift of the plasma frequency due to application of high pressure in the paramagnetic phase.

At 5 K, the plasma frequency was already at higher values, i.e. 2879.34 cm^{-1} due to ferromagnetic ordering, which was increased to 3784.90 cm^{-1} at 7.7 GPa. This confirms the phenomena of a large blue shift in the plasma frequency due to the application of high pressure in the ferromagnetic state.

The ratio of the plasma frequencies for ferromagnetic to the paramagnetic states were calculated at 100 K and 5 K. The calculated $\omega_{p,\,5K} / \omega_{p,\,100K}$ ratio for EuB_6 was found to be 1.68 to 1.80 at 0.7 GPa, which was decreased to 1.03 at 7 GPa. This shows that the magnetic blue shift is diminishing with increasing pressure, which is a remarkable agreement with the earlier calculations done by Kunes et al [81] and Kim et al [79].

5. Conclusions and perspectives

The electrodynamics of the spin density wave (SDW) state for the parent $SrFe_2As_2$ and doped $SrCo_{1.9}Fe_{0.1}As_2$ pnictides were studied by high–pressure infrared spectroscopy at low temperatures. The measurements were carried out in the lab and also tried with synchrotron radiation source at ANKA.

The pressure–temperature phase diagram was drawn for $SrFe_2As_2$ on the basis of the measured LTHP reflectivity data. The pressure of 4 GPa was required at 10 K to suppress the SDW state while at 200 K, a smaller pressure of 1.7 GPa was enough for suppression of SDW state. This shows that the SDW state is more robust at low temperature with respect to the structural deformation caused by the pressure.

The reversibility of the SDW state was not observed at 200 K and 180 K, while it recovered with smaller intensity for temperatures ≤ 150 K. This confirms the weak first order [115] nature of the phase transitions in $SrFe_2As_2$ compounds.

The pressure–dependent kinetic energy ratios (K_{exp} / K_{band}) were calculated at 300 K, 200 K, 100 K and 10 K. The calculated pressure–dependent K_{exp} / K_{band} ratio for $SrFe_2As_2$ at "10 K - 1.4 GPa", was found to be 0.1, which was increased to 0.7 at 5.5 GPa. This indicates the presence of strong electronic correlations at 10 K, which are suppressed at 5.5 GPa and the material exhibits a conventional metallic response.

The cobalt doped $SrFe_{1.9}Co_{0.1}As_2$ pnictide was measured under high pressure and low temperatures. The pressure–temperature phase diagram was drawn on the basis of measured LTHP data. The SDW state suppressed completely at around 1.3 GPa, which shows that $SrFe_{1.9}Co_{0.1}As_2$ lie at the border line of SDW (under doped) and suppressed SDW (over doped) states.

The K_{opt} / K_{band} ratio for $SrFe_{1.9}Co_{0.1}As_2$ pnictide was found to be 0.6 at "10 K - 0.7 GPa", which was increased to 0.7 at 1.1 GPa. The ratio was consistent with calculated K_{opt} / K_{band} ratio for the $SrFe_2As_2$ at 5 GPa. This confirms the phenomena that the small substitution of iron with cobalt leads to the suppression of structural and magnetic transitions and hence, smaller amount of pressure is required to suppress the weak SDW ordering [89, 91-93].

The infrared properties of EuB_6 were studied under high pressure and low temperatures. The small red shift in plasma edge was successfully probed out for temperatures ≥ 200 K (paramagnetic state) which turns into a blue shift for pressures ≥ 1 GPa. In addition, a large blue shift was also observed in ferromagnetic state, i.e. at 12 K and 5 K, which is in good agreement with the results as reported by L. Degiorgi et al [80] at ambient pressure.

The calculated plasma frequency by using the Lorentz–Drude model is 1702.66 cm^{-1} at "297 K - 0.1 GPa", which is consistent with the calculations reported by L. Degiorgi et al [80] at ambient conditions. The plasma frequency was increased to 3221.75 cm^{-1} at 4 GPa which confirmed the phenomena of blue shift in the paramagnetic state due to application of high pressure. The effect is similar to the behaviour of the carbon doped $EuB_{6-x}C_x$ as reported by H. Werheit et al [52], where a small substitution of the carbon at boron sites, leads to the drastic shift of plasma edge towards higher frequencies.

In the ferromagnetic state, i.e. at 5 K, the plasma frequency was increased from 2879.34 cm^{-1} to 3784.90 cm^{-1} at 7.7 GPa. This shows that the application of high pressure leads to the increased metallicity of EuB_6 in both the paramagnetic and ferromagnetic states which can be attributed, either to the increased carrier concentration or reduction in the effective mass of the charge carriers, that results in an increased VB/CB overlap (Δ) at point–X of the Brillouin zone [45, 79, 81].

The calculated $\omega_{p,\,5K} / \omega_{p,\,100K}$ ratio for EuB_6 was found to be 1.68 to 1.80 at 0.7 GPa and decreased to 1.03 at 7 GPa. This shows that the magnetic blue shift in the plasma frequency is diminishing with increasing pressure, which is a remarkable consistency with the earlier calculations done by Kunes et al [81] and Kim et al [79].

As a future prospective, it would be interesting to perform the low temperature and high pressure infrared spectroscopy for cobalt doped $CaFe_2As_2$ and $EuFe_2As_2$ pnictides in the SDW gap regime. In addition, it would be interesting to study the effect of high pressure on the shift of plasma edge for $Eu_{1-x}CaB_6$ at doping concentrations x = 0.1, 0.3 and 1.0.

0. Appendices

0.1. Measuring at Synchrotron Source

The far infrared range was tried for $SrFe_2As_2$ with the "ANKA Synchrotron source", at Karlsruhe Institute of Technology (KIT). The synchrotron beam was interfaced with the Bruker IFS66v spectrometer and LTHP setup as illustrated in Figure 0.1.

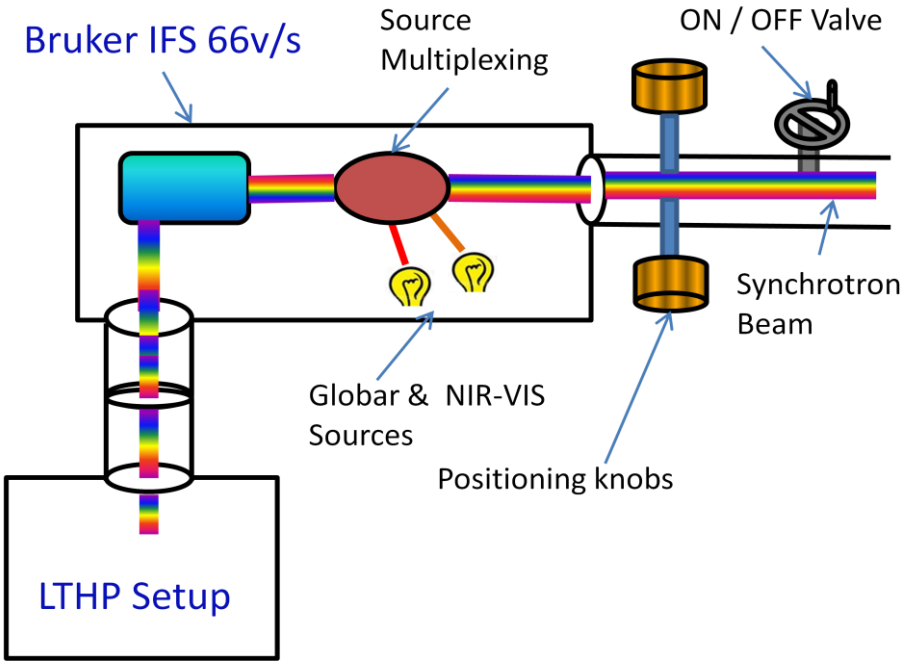

Figure 0.1. Interface scheme for the LTHP setup and ANKA Synchrotron source at Karlsruhe Institute of Technology (KIT).

The synchrotron beam was coupled directly without any optical window to the Bruker spectrometer. The multiplexing system of the Bruker spectrometer was used for switching between different sources. The alignment of the LTHP setup was optimized with the close synchrotron valve. Once the alignment was finished the machines were evacuated and the valve was opened.

A sufficient amount of loss in signal strength was observed after opening the source valve but nothing could be touched inside the LTHP setup. The fine alignment of the beam was done with the positioning knobs of the synchrotron source as shown in Figure 0.1.

The DAC was filled with $SrFe_2As_2$ in the home laboratory and the quality of filling was checked with the Bruker IFS66v spectrometer. The measured test spectrum in the mid infrared range for the filled DAC is shown in Figure 0.2 (b). Figure 0.2 (a) is an illustration drawing of the filled DAC with various measured positions at the surface of sample. The size of the hole was around 300 µm. The material was cooled down in order to observe the SDW gap. Two pressure cycles for the eight sets of temperatures were measured. The spectra are shown in Figure 0.3.

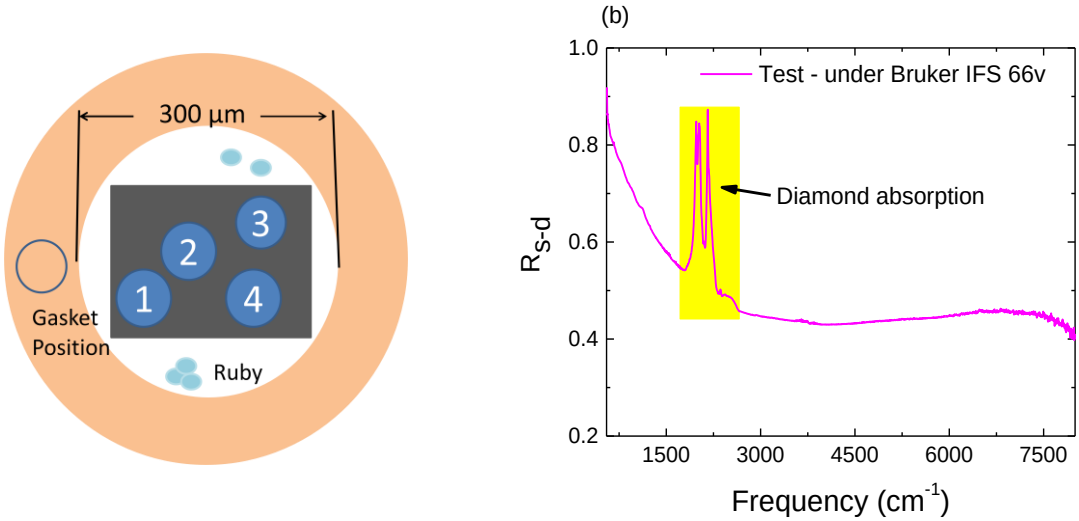

Figure 0.2. (a) An illustration drawing of the filled DAC with $SrFe_2As_2$. Blue circles represent ruby balls, and numbers in the circle shows the various measured positions at the sample's surface. (b) Test measurement of the filled DAC measured under the Bruker IFS66v spectrometer. It shows reflectivity of $SrFe_2As_2$ at 296 K in the mid infrared range.

The measurement range was from 200 cm^{-1} to 700 cm^{-1}. The seven sets of temperatures, i.e. 300 K, 220 K, 180 K, 150 K, 100 K, 50 K, and 10 K were measured. The material was cooled down at a slow cooling rate of 0.44 K / minute.

The reference and sample spectra including background were measured for each temperature. The starting pressure for the first cycle (Figure 0.3 (a)) was 0.4 GPa. For the second cycle (see Figure 0.3 (b)) the pressure was increased to 1.6 GPa. The spectra had bending down problem below 400 cm^{-1} for all measured temperatures under the same set of conditions. The

different measurement techniques were tried but the spectra were not improved more than the results as shown in Figure 0.3.

Since there was a problem in the spectra for both cycles and the spectral feature were not reproducible, the synchrotron source was switched off and the test measurements were done with Globar source in the mid infrared range at various positions for the same DAC filling. The overall reflectivity of the spectra was lowered by 40 % compared to the test spectrum shown in Figure 0.2 (b).

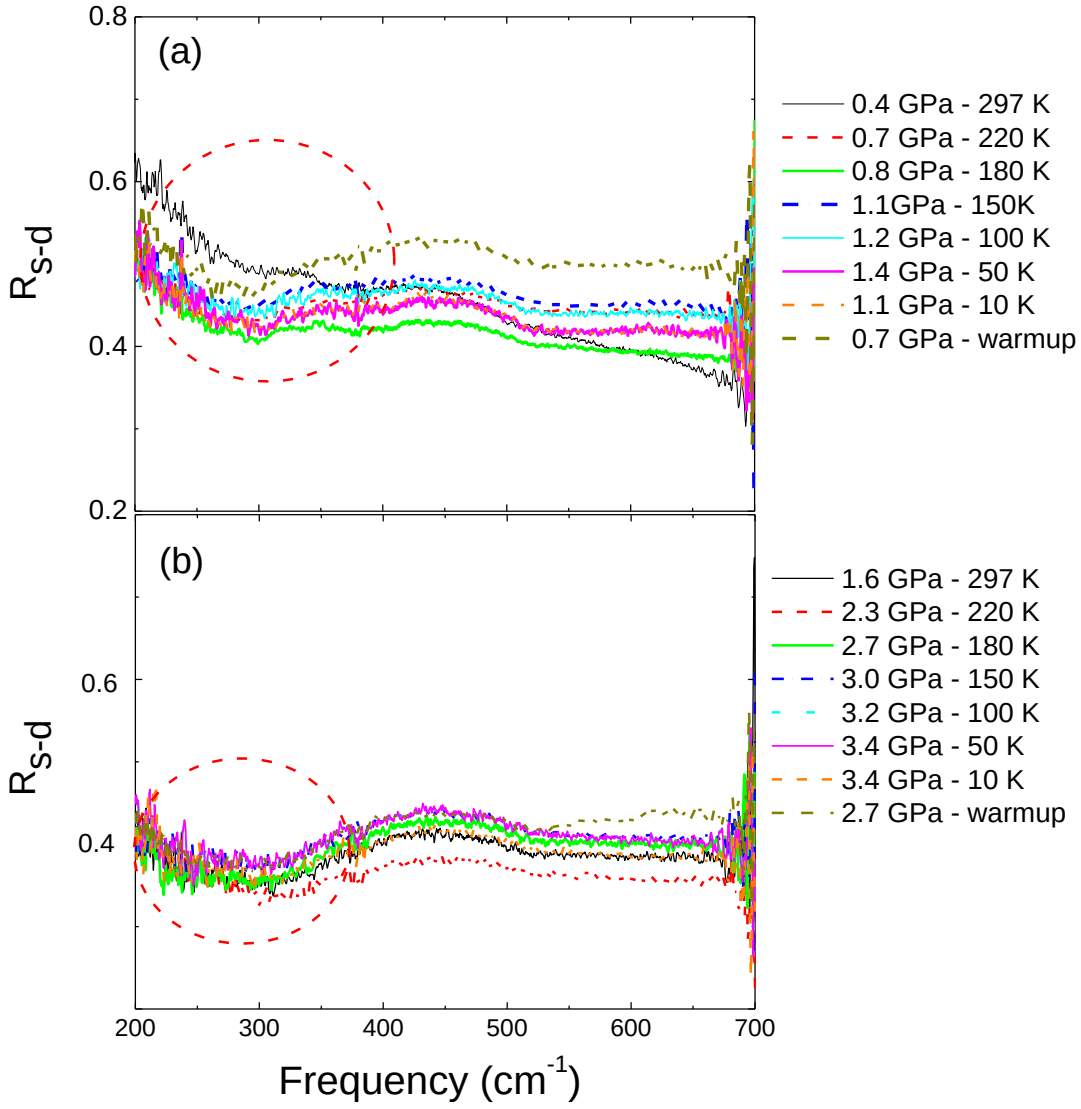

Figure 0.3. Reflectivity (R_{s-d}) of $SrFe_2As_2$ in the far infrared range measured at the synchrotron source. (a) First cycle with the starting pressure of 0.4 GPa. (b) Second cycle with the starting pressure of 1.6 GPa.

For the second beam time in ANKA, the LTHP setup was aligned first in the home laboratory with a standard sample having some prominent features at room temperature. The alignment and measurements were successfully carried out in the home laboratory for $SrFe_2As_2$ as shown in section 3.3.1. The scheme for interfacing LTHP setup was modified for the Synchrotron source at ANKA and shown in Figure 0.4.

The vacuum of the LTHP setup and the synchrotron source was separated with the insertion of an optical window. This gave the flexibility of aligning the LTHP setup directly with the synchrotron source. To keep the alignment unchanged as done for the Vertex–80 spectrometer, a coupling box was used which was designed and developed by A. A. Hadithy in our group. The coupling box consists of two planes mirrors which control the projection angle of the incident beam entering in the LTHP setup. The detectors mirrors are only optimized in order to maximize the signal strength.

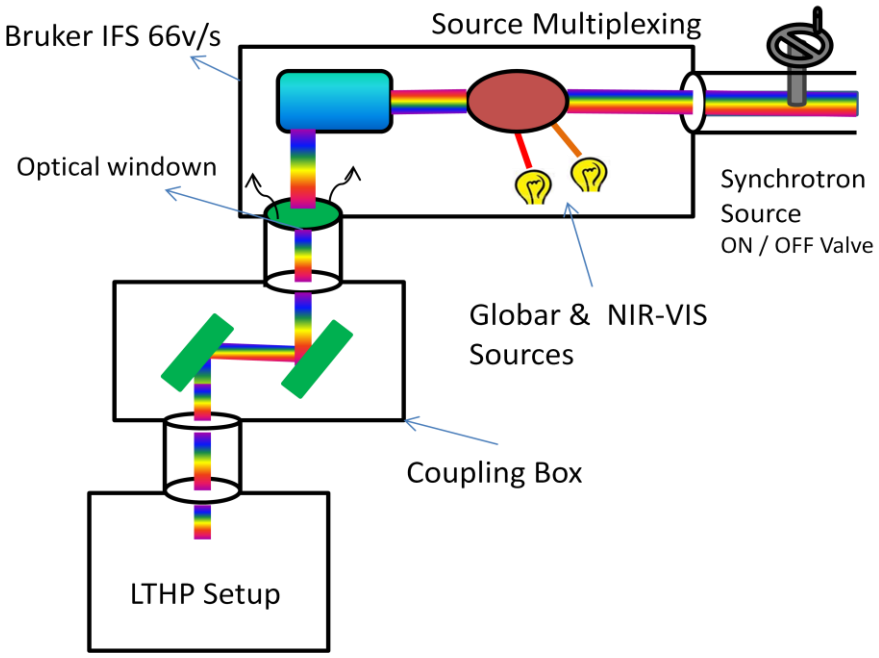

Figure 0.4. Modified alignment scheme for the synchrotron source at ANKA. The LTHP setup is interfaced through the coupling box and an optical window.

The easyLab cell was filled with the standard known sample of magnetide (Fe_2O_3) which has prominent features at room temperature. The quality of filling was checked with Bruker IFS66v spectrometer. The DAC filling is used as a reference to align and check the quality of alignment.

Since the measurement for the filled DAC was not right, free standing measurements were carried out for the bulk sample (Fe_2O_3) inside the LTHP setup. The bigger sample size was mounted at the test stage. The alignment of the LTHP setup was optimized in order to get the right spectra for a bulk sample (Fe_2O_3) at room temperature. Once the alignment was optimized, the test measurements were performed for the same DAC filling (Fe_2O_3) in order to find a recipe for the measurement.

The test spectra were reasonable but the signal–to–noise ratio was very high which indicates that the alignment was not optimized according to the synchrotron source. Furthermore, the signal strength changes considerably with respect to the injection current. For example, the counts were 600 at aperture 1.5 mm, for the injection current of 78.5 mA. The counts were increased to ~ 700 when the new injection was started with the current of 170 mA. Therefore, the signal to noise ratio was not stable throughout the measurements.

0.2. Plots for EuB_6

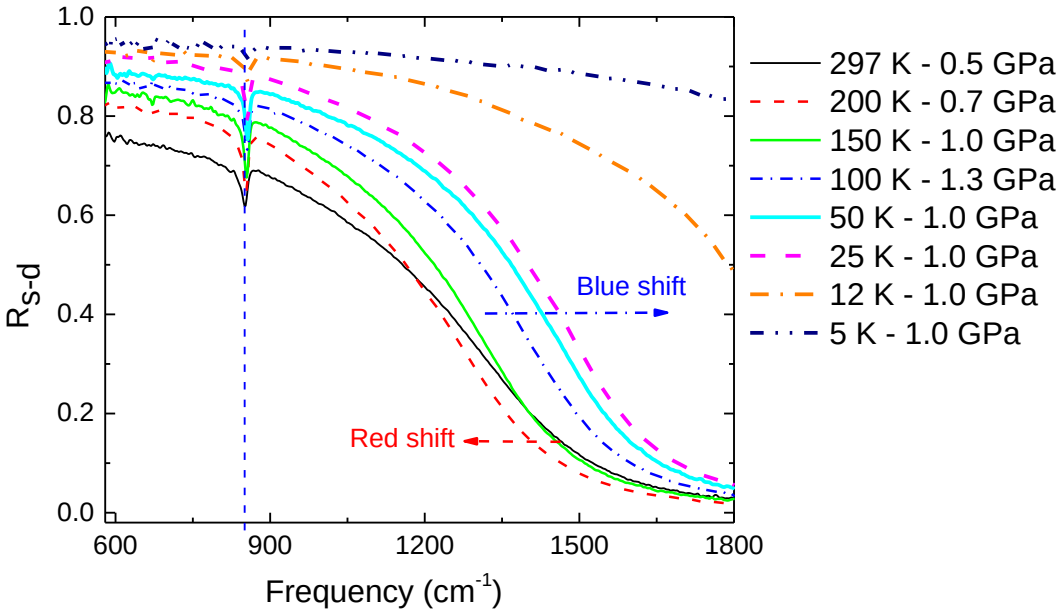

Figure 0.5. Pressure cycle–2, shows the reflectivity ($R_{s\text{-}d}$) of EuB_6 at 0.5 GPa in the low frequency regime, where the red shift exists at 200 K and 150 K.

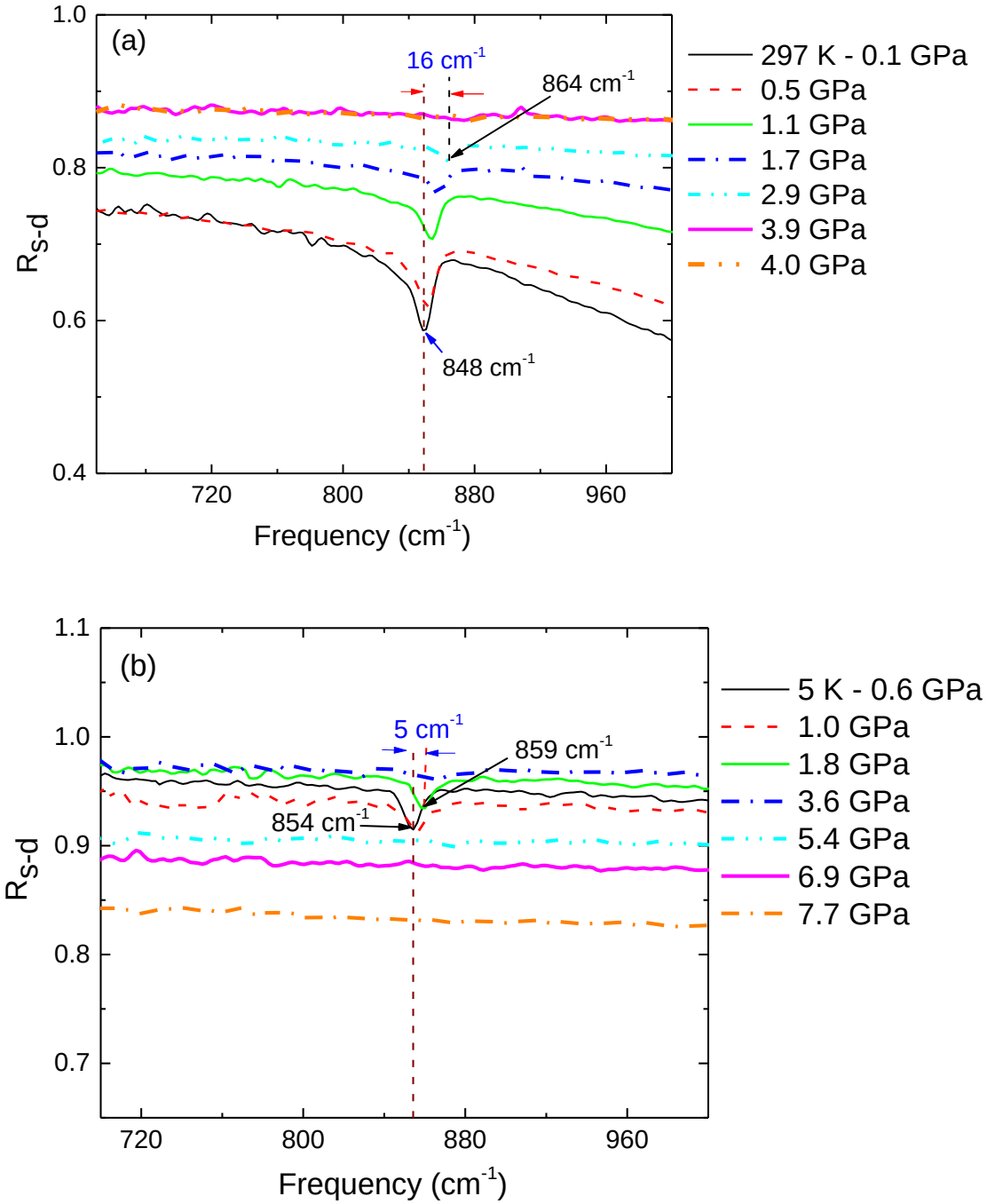

Figure 0.6. Pressure–dependent behaviour of the phonon mode for EuB_6 at (a) 297 K and (b) 5 K.

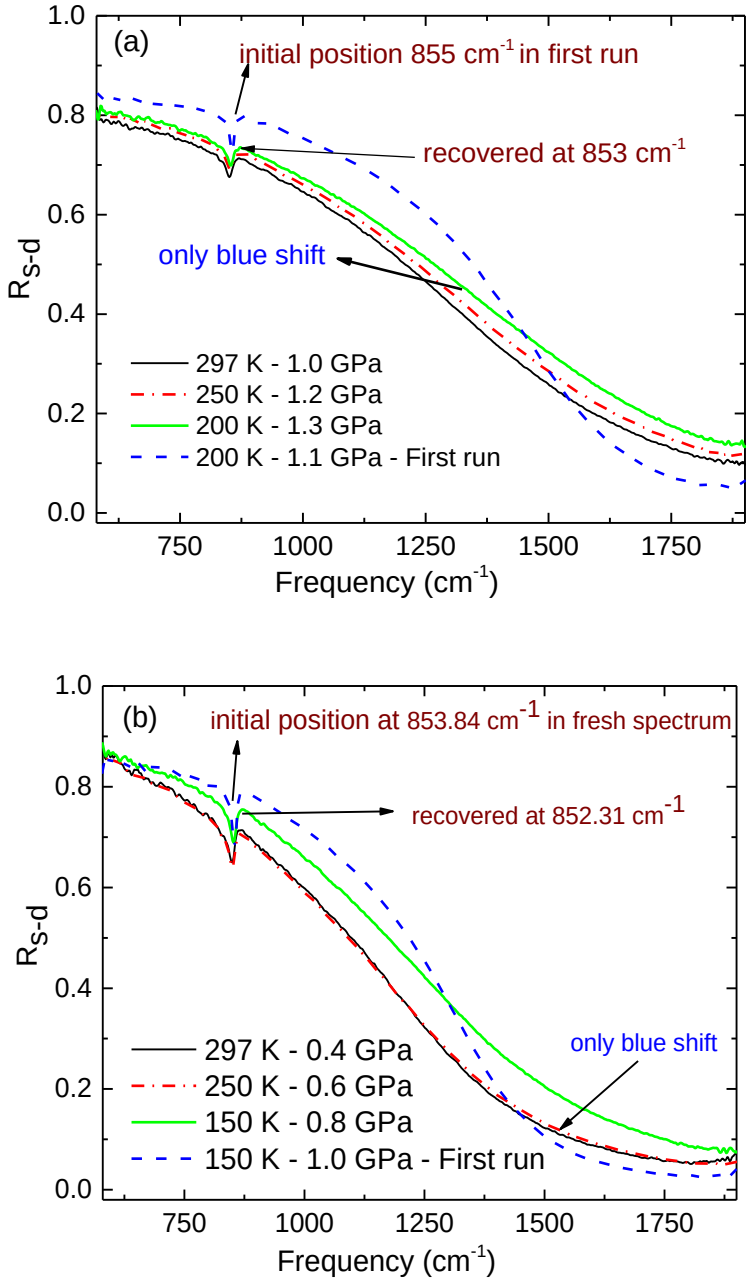

Figure 0.7. Enlarged view of the releasing cycles for EuB_6 at 297 K, 100 K and 12 K in the low frequency range. The spectra from the first run are shown with dashed lines. (a) First releasing cycle at 1.0 GPa. (b) Second releasing cycle at 0.4 GPa.

Bibliography

1. C. C. Homes, M. Reedik, D. A. Cradles, T. Timusk, Appl. Optics 32, 2976 (1993).
2. C. F. Miclea, M. Nicklas, H. S. Jeevan, D. Kasinathan, Z. Hossain, H. Rosner, P. Gegenwart, C. Geibel, and F. Steglich, Phys. Rev. B 79, 212509 (2009).
3. T. Osakabe, and K. Kakurai, J. Appl. Phys. 47, 6544 (2008).
4. A. S. Sefat, R. Jin, M. A. McGuire, B. C. Sales, D. J. Singh, and D. Mandrus. Phys. Rev. Lett. 101, 117004 (2008).
5. M. Rotter, M. Tegel, D. Johrendt, I. Schellenberg, W. Hermes, and R. Pottgen, Phys. Rev. B 78, 020503 (2008).
6. W. B. Holzapfel, and N. S. Isaacs, *High Pressure Techniques in Chemistry and Physics*, (Oxford University Press, UK, 1997).
7. R. Kingslake, and R. B. Johnson, *Lenses Design Fundamental*, (SPIE Press, USA, 2010).
8. F. Wooten, *Optical Properties of Solids*, (Academic Press, New York, USA, 1972).
9. H. Kuzmany, *Solid state spectroscopy*, Second edition (Springer, New York, USA, 2009).
10. M. J. Reidl, *Optical Design Fundamentals for Infrared Systems*, (SPIE, Washington, USA, 2001).
11. V. Saptari, *Fourier Transforms Spectroscopy Instrumentation Engineering*, (SPIE Press, Washington, USA, 2004).
12. M. Fox, *Optical Properties of Solids*, (Oxford University Press, New York, USA, 2001).
13. M. Gerloch, and E. C. Constable, *Transition Metal Chemistry, The Valence Shell in D–Block Chemistry*, (VCH Verlagsgeschaft mbH, Weinheim, Germany, 1994).
14. V. Y. Irkhin, and Y. P. Irkhin, *Electronic structure, correlation effects and physical properties of d and f–transition metals and their compounds*, (Cambridge international science publishing, Cambridge, UK, 2007).
15. A. Marouchkine, *Room–Temperature Superconductivity*, (Cambridge internal science publishing, Cambridge, UK, 2004).
16. A. Schillings, M. Cantoni, J. D. Guo, and H. R. Ott, Nature 363, 56–58 (1993).

17. A. H. Wilson, Proc. Roy. Soc. A 133, 458 (1931).
18. H. K. Onnes, Leiden Commun. 120 b, 122 c, 124 c (1911).
19. T. Sato, K. Nakayama, Y. Sekiba, P. Richard, Y. -M. Xu, S. Souma, T. Takahashi, G. F. Chen, J. L. Luo, N. L. Wang, and H. Ding, Phys. Rev. Lett. 103, 047002 (2009).
20. A. Jayaraman, Rev. Sci. Instrum. 57, 1013 (1986).
21. S. Klotz, J. C. Chervin, P. Munsch, and G. Le. Marchand, J. Phys. D: Appl. Phys. 42, 075413 (2009).
22. M. Rotter, M. Tegel, and D. Johrendt, Phys. Rev. Lett. 101, 107006 (2008).
23. I. R. Shein, and A. L. Ivanovskii, J. Struct. Chem. 50, 3, 552-555, (2009).
24. G. S. Girolami, J. Chem. Educ. 86, 10, 1200 (2009).
25. N. G. Connelly, Ture Damhus, R. M. Hartshorn, and A. T. Hutton, IUPAC Recommendations 27, No. 6, section IR–3.5 (2005).
26. C. Day, Phys. Today 61, 5, 11-12 (2008).
27. J. -T. Han, J. -S. Zhou, J. -G. Cheng, and J. B. Goodenough, J. Am. Chem. Soc. 132, 3, 908–909 (2010).
28. P. L. Alireza, Y. T. Chris Ko, J. Gillett, C. M. Petrone, J. M. Cole, G. G. Lonzarich, and S. E. Sebastianet, J. Phys.: Condens. Matter 21, 012208 (2009).
29. K. Matsubayashi, K. Ohgushi, A. Yamada, K. Munakata, T. Matsumoto, and Y. Uwatoko, J. Phys. Soc. Jpn. 78, 7, 073706 (2009).
30. H. Kotegawa, T. Kawazoe, H. Sugawara, K. Murata, and H. Tou, J. Phys. Soc. Jpn. 78, 8, 083702 (2009).
31. J. H. Chu, J. G. Analytis, C. Kucharczyk, and I. R. Fisher, Phys. Rev. B 79, 014506 (2009).
32. G. L. Sun, D. L. Sun, M. Konuma, P. Popovich, A. Boris, J. B. Peng, K. -Y. Choi, P. Lemmens, and C. T. Lin, J. of Supercond. and Novel Magn. 24, 1773 (2011).
33. G. A. Sawatzky, I. S. Elfimov, J. Van den Brink, J. Zaanen, EPL, 86, 1, 17006 (2009).
34. H. Li, W. Tian, J. L. Zarestky, A. Kreyssig, N. Ni, S. L. B. Ko, P. C. Canfield, A. I. Goldman, R. J. McQueeney, and D. Vaknin, Phys. Rev. B 80, 054407 (2009).
35. J. W. Lynn, and P. Dai, Physica C 469, 469–476 (2009).
36. X. Xia, D. Qian, L. Wray, D. Hsieh, G. F. Chen, J. L. Luo, N. L. Wang, and M. Z. Hasan, Phys. Rev. Lett. 103, 037002 (2009).
37. G. Grüner, Rev. Mod. Phys. 66, 1, (1994).

38. L. Degiorgi, M. Dressel, A. Schwartz, B. Alavi, and G. Grüner, Phys. Rev. Lett. 76, 3838 (1996).
39. V. Vescoli, L. Degiorgi, M. Dressel, A. Schwartz, W. Henderson, B. Alavi, G. Grüne, J. Brinckmann, and A. Virosztek, Phys. Rev. B 60, 8019 (1999).
40. H. Hiramatsu, T. Katase, T. Kamiya, M. Hirano, and H. Hosono, Phys. Rev. B 80, 052501 (2009).
41. A. J. Arko, G. Crabtree, J. B. Ketterson, F. M. Müller, P. F. Walch, L. R. Windmiller, Z. Fisk, R.F. Hoyt, A. C. Mota, and R. Viswanathan, Int. Quantum Chem. Quantum Bio1. Symp. 9, 569 (1975).
42. G. Travaglini, and P. Wachter, Phys. Rev. B 29, 893 (1984).
43. S. Süllow, I. Prasad, M. C. Aronson, S. Bogdanovich, J. L. Sarrao, and Z. Fisk, Phys. Rev. B 62, 11626 (2000).
44. C. N. Guy, S. V. Molnar, J. Etourneau, Z. Fisk, Solid State Commun. 33, 1055 (1980).
45. S. Massidda, A. Continenza, T. M. de Pascale, and R. Monnier, Z. Phys. Rev. B 102, 83 (1997).
46. S. A. Wolf, D. D. Awschalom, R. A. Buhrman, J. M. Daughton, S. von Mohlnar, M. L. Roukes, A. Y. Chtchelkanova, and D. M. Treger, Science 294, 1488 (2001).
47. H. J. Tromp, P. van Gelderen, P. J. Kelly, G. Brocks, and P. A. Bobbertet, Phys. Rev. Lett. 87, 016401 (2001).
48. D. P. Young, D. Hall, M. E. Torelli, Z. Fisk, J. L. Sarrao, J. D. Thompson, H. R. Ott, S. B. Oseroff, R. G. Goodrich, and R. Zysler, Nature 397, 412 (1999).
49. M. Kasaya, J. M. Tarascon, J. Etourneau, and P. Hagenmuller, Materials Research Bulletin 13, 751-756 (1978).
50. S. von Molnar, J. M. Tarascon, and J. Etourneau, J. Appl. Phys 52, 2158-2160 (1981).
51. J. M. Tarascon, J. L. Soubeyroux, J. Etourneau, and R. Georges, Solid State Commun. 37, 133-137 (1981).
52. H. Werheit, T. Au, R. Schmechel, Y. B. Paderno, and E. S. Konovalova, J. of Solid State Chem. 154, 87–92 (2000).
53. U. Yu, and B. I. Min, Phys. Rev. Lett. 94, 117202 (2005).
54. J. S. Rhyee, J. Y, Kim, and B. K, Cho, J. Appl. Phys. 97, 10901 (2005).
55. K. Schmitt, C. Stückl, H. Ripplinger, and B. Albert, Solid State Sciences 3, 321–327 (2001).
56. J. C. Cooley, and M. C. Aronson, Phys. Rev. B 56, 221 (1997).

57. T. Lundström, B. Lönnberg, and B. Törmä , Pysica Scripta. 26, (1982).

58. L. Bai, and N. Ma, Physica B 405, 4634–4637 (2010).

59. M. Kreissl, and W. Nolting, Phys. Rev. B 72, 245117 (2005).

60. S. Massidda, A. Continenza, T. M. de Pascale, and R. Monnier, Phys. Rev. B 102, 83–89 (1997).

61. J. D. Denlinger, J. A. Clack, J. W. Allen, G.-H. Gweon, D. M. Poirier, C. G. Olson, J. L. Sarrao, A. D. Bianchi, and Z. Fisk, Phys. Rev. Lett. 89, 157601 (2002).

62. W. Ku, and A. G. Eguiluz, Phys. Rev. Lett. 89, 126401 (2002).

63. Z. Wu, D. J. Singh, and R. E. Cohen, Phys. Rev. B 69, 193105 (2004).

64. R. A. Forman, G. J. Piermarini1, J. D. Barnett, and S. Block, Science 21, 176, 4032, 284–285 (1972).

65. J. D. Barnett, S. Block, and G. Piermarini, Rev. Sci. Instrum. 44, 1 (1973).

66. K. Syassen, and I. Loa, private communication.

67. K. Thirunavukkuarasu, PhD thesis, Augsburg University, April 2009.

68. Silicon Bolometer instruction manual. Bolometer Systems. www.irlabs.com.

69. Company manual of “CryoDAC Mega” easyLab cell.

70. Cryostat Insert, from CryoVac KONTI cryostat with the mounted Diamond Anvil Cell.

71. A. Pashkin, Low–temperature and high–pressure microscope manual, (unpublished).

72. P. Erdös, IBM research laboratory Zurich, Switzerland Feb 2, 1959.

73. K. Syassen, Schwarzschild Optics, ANKA Notes, appendix E.

74. Bruker instructions and operation manuals for Models: IFS66v and Vertex–80.

75. J. D. Denlinger, F. Wang, J. W. Allen, H. –H. Lee, Z. Fisk, B. Delley, and R. Monnier, APS Meeting Bulletin, 2007 Paper No. A7.00003 (unpublished).

76. W. Ku, and A. G. Eguiluz, Phys. Rev. Lett. 89, 126401 (2002).

77. Z. Wu, D. J. Singh, and R. E. Cohen, Phys. Rev. B. 69, 193105 (2004).

78. J. H. Kim, Y. Lee, C. C. Homes, J. -S, Rhyee, B. K. Cho, S. -J. Oh and E. J. Choi, Phys. Rev. B 71, 075105 (2005).

79. J. H. Kim, Y. J, Kim, J. Kunes, B. K. Cho, and E. J. Choi, Phys. Phys. Rev. B 78, 165120 (2008).

80. L. Degiorgi, E. Felder, H. R Ott, J. L. Sarrao, and Z. Fisk, Phys. Rev. Lett. 79, 25 (1997).
81. J. Kunes, and W. E Pickett, Phys. Rev. B 69, 165111 (2004).
82. A. B. Kuzmenko, Rev. Sci. Instrum. 76, 083108 (2005).
83. Y. Okimoto, T. Katsufuji, T. Ishikawa, A. Urushibara, T. Arima, and Y. Tokuraet, Phys. Rev. Lett. 75, 109 (1995).
84. T. Kamiya, H. Hiramatsu, T. Katase, M. Hirano, and H. Hosono, Material Science and Engineering, B 173, 244-247 (2010).
85. R. Hoffmann, and C. Zheng, J. Phys. Chem. 89, 4175-4181 (1985).
86. D. Johrendt, and R. Pöttgen, Physica C 469, 332-339 (2009).
87. Z. Ban, and M. Sikirica, Acta Cryst. 18, 594 (1965).
88. I. R. Shein, and A.L. Ivanovskii, J. Struct. Chem. 50, 3, 552-555, (2009).
89. A. Leithe–Jasper, W. Schnelle, C. Geibel, and H. Rosner, Phys. Rev. Lett. 101, 207004 (2008).
90. G. F. Chen, Z. Li, G. Li, W. Z. Hu, J. Dong, X. D. Zhang, P. Zheng, N. L. Wang, and J. L. Luo, Chin, Phys. Lett. 25, 3403 (2008).
91. C. Krellner, N. C. Canales, A. Jesche, H. Rosner, A. Ormeci, and C. Geibel, Phys. Rev. B 78, 100504 (2008).
92. A. Jesche, N. Caroca-Canales, H. Rosner, H. Bormann, A. Ormeci, D. Kasinathan, H. H. Klaus, H. Luetken, R. Khasanov, A. Amato, A. Hoser, K. Kaneko, C. Krellner, and C. Geibel, Phys. Rev. B 78, 180504(R) (2010).
93. S. Lebegue, Phys. Rev. B. 75, 035110 (2007).
94. G. Xu, W. Ming, Y. Yao, X. Dai, S. -C Zhang, and Z. Fang, Eur. Phys. Lett. 82, 67002 (2008).
95. P. Blaha, WIEN2K–10.1, (release 14.01.2011).
96. K. Kirshenbaum, S. R. Saha, T. Drye, and J. Paglione, Phys. Rev. B 82, 144518 (2010).
97. N. Kumar, S. Chi, Y. Chen, K. G. Rana, A. K. Nigam, Thamizhavel, W. Ratchliff, S. K. Dhar, and J. W. Lynn, Phys. Rev. B 80, 144524 (2009).
98. S. R. Saha, N. P. Butch, K. Kirshenbaum, and J. Paglione, Phys. Rev. B 79, 224519 (2009).
99. S. Jiang, H. Xing, G. Xuan, C. Wang, Z. Ren, C. Feng, J. Dai, Z. Xu, and G. Cao, J. Phys., Condens. Matter 21, 382203 (2009).

100. V. Zinth, and D. Jhorendt, EPL 98, 57010 (2012).
101. F. Han, X. Zhu, P. Cheng, B. Shen, and H. -H. Wen, Phys. Rev. B 80, 024506 (2009).
102. I. I. Mazin, D. J. Singh, M. D. Johannes, and M. H. Du, Phys. Rev. Lett. 101, 057003 (2008).
103. K. Kurosk, S. Onari, R. Arita, H. Usui1, Y. Tanaka, H. Kontani, and H. Aoki, Phys. Rev. Lett. 101, 087004 (2008).
104. F. Wang, H. Zhai, Y. Ran, A. Vishwanath, and D. -H. Lee, Phys. Rev. Lett. 102, 047005 (2009).
105. X. Zhu, F. H. P. Cheng, B. Shen, H. -H. Wen, Phys. Rev. B 80, 024506 (2009).
106. P. C. Canfield, S. L. Bud'ko, Ni Ni, J. Q. Yan, and A. Kracher, Phys. Rev. B 80, 060501 (R) (2009).
107. J. -H. Chu, J. G. Analytis, C. Kucharczyk, and I. R. Fisher, Phys. Rev. B 79, 014506 (2009).
108. L. J. Li, Y. K. Luo, Q. B. Wang, H. Chen, Z. Ren, Q. Tao, Y. K. Li, X. Lin, M. He, Z. W. Zhu, G. G. Cao, and Z. A. Xu, New J. Phys. 11, 025008 , 8pp (2009).
109. G. Cao, S. Jiang, X. Lin, C. Wang, Y. Li, Z. Ren, Q. Tao, C. Feng, J. Dai, Z. Xu, and F. -C. Zhang, Phys. Rev. B 79, 174505 (2009).
110. Q. Han, Y. Chen, and Z. D. Wang, EPL, 82, 37007 (2008).
111. D. K. Pratt, W. Tian, A. Kreyssig, J. L. Zarestky, S. Nandi, N. Ni, S. L. Bud'ko, P. C. Canfield, A. I. Goldman, and R. J. McQueeney, Phys. Rev. Lett. 103, 087001 (2009).
112. N. Ni, M. E. Tillman, J. -Q. Yan, A. Kracher, S. T. Hannahs, S. L. Bud'ko, and P. C. Canfield, Phys. Rev. B 78, 214515 (2008).
113. W. Schnelle, A. Leithe-Jasper, R. Gumeniuk, U. Burkhardt, D. Kasinathan, and H. Rosner, Phys. Rev. B 79, 214516 (2009).
114. E. D. Bauer, F. Ronning, B. L. Scott, and J. D. Thompson, Phys. Rev. B 78, 172504 (2008).
115. Y. Z. Zhang, H. C. Kandpal, I. Opahle, H. O. Jeschke, and R. Valentí, Phys. Rev. B 80, 094530 (2009).
116. D. K. Pratt, Y. Zhao, S. A. J. Kimber, A. Hiess, D. N. Argyriou, C. Broholm, A. Kreyssig, S. Nandi, S. L. Bud'ko, N. Ni, P. C. Canfield, R. J. McQueeney, and A. I. Goldman, Phys. Rev. B 79, 060510 (R) (2009).
117. A. I. Goldman, D. N. Argyriou, B. Ouladdiaf, T. Chatterji, A. Kreyssig, S. Nandi, N. Ni, S. L. Bud'ko, P. C. Canfield, and R. J. McQueeney, Phys. Rev. B 78, 100506(R) (2008).

118. M. Kumar, M. Nicklas, A. Jesche, N. C. Canales, M. Schmitt, M. Hanfland, D. Kasinathan, U. Schwarz, H. Rosner, and C. Geibel, Phys. Rev. B 78, 184516 (2008).
119. H. Kotegawa, H. Sugawara, and H. Toua, J. Phys. Soc. Jpn. 78, 013709 (2008).
120. S. A. J. Kimber, A. Kreyssig, Y. -Z. Zhang, H. O. Jeschke, R. Valentí, F. Yokaichiya, E. Colombier, J. Yan, T. C. Hansen, T. Chatterji, R. J. McQueeney, P. C. Canfield, A. I. Goldman, and D. N. Argyriou, Nature Mater. 8, 471 (2009).
121. E. Colombier, S. L. Bud'ko, N. Ni, and P. C. Canfield, Phys. Rev. B 79, 224518 (2009).
122. D. J. Singh, and M. H. Du, Phys. Rev. Lett. 100, 237003 (2008).
123. J. Zhao, D. -X. Yao, S. Li, T. Hong, Y. Chen, S. Chang, W. Ratcliff, J. W. Lynn, H. A. Mook, G. F. Chen, J. L. Luo, N. L. Wang, E. W. Carlson, J. Hu, and P. Dai1, Phys. Rev. Lett. 101, 167203 (2008).
124. R. Car, and M. Parrinello, Phys. Rev. Lett. 55, 2471 (1985).
125. P. E. Blöchl, Phys. Rev. B 50, 17953 (1994).
126. M. Parrinello, and A. Rahman, Phys. Rev. Lett. 45, 1196 (1980).
127. Y. -Z. Zhang, H. O. Jeschke, and Roser Valentí, Phys. Rev. Lett. 101, 136406 (2008).
128. I. Opahle, H. C. Kandpal, Y. Zhang, C. Gros, and R. Valentí, Phys. Rev. B 79, 024509 (2009).
129. T. C. Kobayashi, H. Hidaka, H. Kotegawa, K. Fujiwara, M. Eremets, Rev. Sci. Instrum. 78, 023909 (2007).
130. N. Tateiwa, and Yoshinori Haga, J. Phys., Conference Series 215, 012178 (2010).
131. C. D. Cruz, Q. Huang, J. W. Lynn, J. Li, W. Ratcliff , J. L. Zarestky, H. A. Mook, G. F. Chen, J. L. Luo, N. L. Wang, and Pengcheng Dai, Nature 453, 899–902, (2008).
132. J. Zhao, W. Ratcliff, J. W. Lynn, G. F. Chen, J. L. Luo, N. L. Wang, J. Hu, and P. Dai, Phys. Rev. B 78, 140504 (R) (2008).
133. J. Orenstein, Schrieffer, 299–309, 10/10 (2006).
134. N. W. Ashcroft, and N. D. Mermin, *Solid State Physics*, (Cengage Learning publisher, Franklin Lakes, NJ, USA, 1976).
135. W. Z. Hu, J. Dong, G. Li, Z. Li, P. Zheng, G. F. Chen, J. L. Luo, and N. L. Wang, Phys. Rev. Lett. 101, 257005 (2008).
136. J. Dong, H. J. Zhang, G. Xu, Z. Li, G. Li, W. Z. Hu, D. Wu, G. F. Chen, X. Dai, L. Luo, Z. Fang, and N. L. Wang, EPL 83, 3, 27006 (2008).
137. C. de la Cruz, Q. Huang, J. W. Lynn, J. Li, W. R. Li, J. L. Zarestky, H. A. Mook, G. F. Chen, J. L. Luo, N. L. Wang, and P. Dai, Nature 453, 899 (2008).
138. M. A. Lind, and J. L. Stanford, Phys. Rev. Lett. 39A, 1, (1972).

139. G. Li, W. Z. Hu, J. Dong, Z. Li, P. Zheng, G. F. Chen, J. L. Luo, and N. L. Wang, Phys. Rev. Lett. 101, 107004 (2008).
140. F. Ma, Z. -Y. Lu, and T. Xiang, Front. Phys. China, 5(2), 150 (2010).
141. L. X. Yang, Y. Zhang, H. W. Ou, J. F. Zhao, D. W. Shen, B. Zhou, J. Wei, F. Chen, M. Xu, C. He, Y. Chen, Z. D. Wang, X. F. Wang, T. Wu, G. Wu, X. H. Chen, M. Arita, K. Shimada, M. Taniguchi, Z. Y. Lu, T. Xiang, and D. L. Feng, Phys. Rev. Lett. 102, 107002 (2009).
142. S. J. Moon, J. H. Shin, D. Parker, W. S. Choi, I. I. Mazin, Y. S. Lee, J. Y. Kim, N. H. Sung, B. K. Cho, S. H. Kim, J. S. Kim, K. H. Kim, and T. W. Noh, Phys. Rev. B 81, 205114 (2010).
143. F. Pfuner, J. G. Analytis, J. -H. Cheu, I. R. Fisher and L. Degiorgi, Eur. Phys. J. B 67, 513 (2009).
144. S. E. Sebastian, J. Gillett, N. Harrison, P. H. C. Lau, D. J. Singh, C. H. Mielke, and G. G. Lonzarich, J. Phys., Condens. Matter 20, 422203 (2008).
145. L. Fang, H. Luo, P. Cheng, Z. Wang, Y. Jia, G. Mu, B. Shen, I. I. Mazin, L. Shan, C. Ren, and H. -H. Wen, Phys. Rev. B. 80, 140508 (R) (2009).
146. D. Hsieh, Y. Xia, L. Wray, D. Qian, K. Gomes, A. Yazdani, G. Chen, J. L. Luo, N. L. Wang, and M. Z. Hasan, 12 Dec 2008, [cond-mat.supr.con] arXiv:0812.2289. Submitted to Nature (2009), (unpublished).
147. D. J. Singh, Phys. Rev. B. 78, 094511 (2008).
148. F. Ma, Z. -Y. Lu, and T. Xiang, Phys. Rev. B. 78, 224517 (2008).
149. I. I. Mazin, D. J Singh, M. D. Johannes, and M. H. Du, Phys. Rev. Lett. 101, 057003 (2008).
150. H. S. Jeevan, Z. Hossain, D. Kasinathan, H. Rosner, C. Geibele, and P. Gegenwart, Phys. Rev. B 78, 052502 (2008).
151. C. F. Miclea, M. Nicklas, H. S. Jeevan, D. Kasinathan, Z. Hossain, H. Rosner, P. Gegenwart, C. Geibel, and F. Steglich, Phys. Rev. B 79, 212509 (2009).
152. S. Jiang, Y. Luo, Z. Ren, Z. Zhu, C. Wang, X. Xu, Q. Tao, G. Cao, and Z. Xu , New J. Phys. 11, 025007 (2009).
153. T. Shimojima, K. Ishizaka, Y. Ishida, N. Katayama, K. Ohgushi, T. Kiss, M. Okawa, T. Togashi, X. -Y. Wang, C. -T. Chen, S. Watanabe, R. Kadota, T. Oguchi, A. Chainani, and S. Shin, Phys. Rev. Lett. 104, 057002 (2010).
154. D. Wu, N. Barišić, P. Kallina, A. Faridian, B. Gorshunov, N. Drichko, L. J. Li, X. Lin, G. H. Cao, Z. A. Xu, N. L. Wang, and M. Dressel, Phys. Rev. B 81, 100512(R) (2010).

155. M. A Lind, and J. L. Stanford, Physics letters 39, 1, 5–6, (1972).
156. M. M. Qazilbash, J. J. Hamlin, R. E. Baumbach, Lijun Zhang, D. J. Singh, M. B. Maple, and D. N. Basov, Nature Phys. 5, 647 (2009).
157. P. Dore, A. Nucara, D. Cannavò, G. D. Marzi, P. Calvani, A. Marcelli, R. S. Sussmann, A. J. Whitehead, C. N. Dodge, A. J. Krehan, and H. J. Peters, Appl. Optics 37, 24, 5731-5736 (1998).
158. J. S. Plaskett, and P. N. Schatz, J. Chem. Phys. 38, 612 (1963).
159. G. F. Chen, Z. Li, J. Dong, G. Li, W. Z. Hu, X. D. Zhang, X. H. Song, P. Zheng, N. L. Wang, and J. L. Luo, Phys. Rev. B 78, 224512 (2008).
160. D. J. Padilla, PhD thesis, San Diego State University, fall 2012.
161. J. Dong, H. J. Zhang, G. Xu, Z. Li, G. Li, W. Z. Hu, D. Wu, G. F. Chen, X. Dai, J. L. Luo, Z. Fang, and N. L. Wang, EPL 83, 2, 27006 (2008).
162. A. J Millis, A. Zimmers, R. P. S. M. Lobo, N. Bontemps, and C. C. Homes, Phys. Rev. B 72, 224517 (2005).
163. Q. Si, Nature Phys. 5, 629–630, (2009).
164. D. L. Cruz, Q. Huang, J. W. Lynn, Jiying Li, W. Ratcliff, J. L. Zarestky, H. A. Mook, G. F. Chen, C. J. L. Luo, N. L. Wang, and P. Dai, Nature 453, 8999–902 (2008).
165. J. J. Hamlin, R. E. Baumbach, D. A. Zocco, T. A. Sayles, and M. B. Mapleet, J. Phys. Condens. Matter 20, 365220 (2008).
166. J. P. Carlo, Y. J. Uemura, T. Goko, G. J. MacDougall, J. A. Rodriguez, W. Yu, G. M. Luke, P. Dai, N. Shannon, S. Miyasaka, S. Suzuki, S. Tajima, G.F. Chen, W. Z. Hu, J. L. Luo, and N. L. Wang, Phys. Rev. Lett. 102, 087001 (2009).
167. D. J. Singh, and M. -H. Du, Phys. Rev. Lett. 100, 237003 (2008).
168. Q. Si, J. H. Shim, and G. Kotliar, Phys. Rev. Lett. 100, 226402 (2008).
169. A. Leithe–Jasper, W. Schnelle, C. Geibel, and H. Rosner, Phys. Rev. Lett. 101, 207004 (2008).
170. A. Lucarelli, A. Dusza, F. Pfuner, P Lerch, J. G. Analytis, J. -H. Chu, I. R. Fisher, and L. Degiorgi, New J. Phys. 12, 073036 (2010).
171. C. Lester, J. -H. Chu, J. G. Analytis, S. C. Capelli, A. S. Erickson, C. L. Condron, M. F. Toney, I. R. Fisher, and S. M. Hayden, Phys. Rev. B 80, 229901 (2009).
172. J. -H Chu, J. G. Analytis, C. Kucharczyk, and I. R. Fisher, Phys. Rev. B 79, 014506 (2009).
173. D. N. Basov, and Timusk, Rev. Mod. Phys. 77, 721 (2005).

174. H. Okamura, K. Shoji, K. Miyatai, H. Sugawara, T. Moriwak, and Y. Ikemoto, J. Phys. Soc. Jpn, 82, 074720, July 2013.
175. H. Okamura, J. Phys., Conference Series 359, 012013 (2012).
176. L. Baldassarre, A. Perucchi, P. Postorino, S. Lupi, C. Marini, L. Malavasi, J. Jiang, J. D. Weiss, E. E. Hellstrom, I. Pallecchi, and P. Dore, Phys. Rev. B 85, 174522 (2012).
177. K. Ahilan, F. L. Ning, T. Imai, A. S. Sefat, M. A. McGuire, B. C. Sales, and D. Mandrus, Phys. Rev. B 79, 214520 (2009).
178. J. Zhao, Q. Huang, Q. Huang, C. de la Cruz, S. Li, J.W. Lynn, Y. Chen, M. A. Green, G. F. Chen, G. Li, Z. Li, J. L. Luo, N. L. Wang, and P. Dai, Nature Mater. 7, 953 (2008).
179. G. Profeta (unpublished).
180. N. Ni. A. Thaler, J. Q. Yan, A. Kracher, E. Colombier, S. L. Budko, P. C. Canfield, and S. T. Hannahs, Phys. Rev. B 82, 024519 (2010).
181. A. Sacchetti, E. Arcangeletti, A. Perucchi, L. Baldassarre, P. Postorino, S. Lupi, N. Ru, I. R. Fisher, and L. Degiorgi, Phys. Rev. Lett. 98, 026401 (2007).
182. L. Benfatto, E. Cappelluti, and C. Castellanie, Phys. Rev. B 80, 214522 (2009).
183. L. Ortenzi, E. Cappelluti1, L. Benfatto, and L. Pietronero1, Phys. Rev. Lett. 103, 046404 (2009).
184. J. G. Bednorz, and K. A. Müller, Phys. Rev. B 64, 189 (1986).
185. Y. Kamihara, T. Watanabe, M. Hirano, and H. Hosono, J. Am. Chem. Soc. 130, 3296 (2008).

List of patents and publications

- **Patent of "Power Protection Unit"** in Patent and Design Office Pakistan.
  Patent No. PCPPK-S/1275/92-93/P & D-17-06-93-4,000. Application No. 478/2003.
  Abid Karim, Khalid Saleem, Mohammad Yaqub, S.M. Saeed.

- **An investigation in thermal behaviour of therparker coal.**
  Mahmood Iqbal, Tehzeeb Akhtar, Abid Karim, Farooq A. Khan.
  Journal of Chemical Society of Pakistan. Jour.Chem.soc.Pak. Vol. 28, No. 2, 519-524 (2006).

- **Studies on three excess properties of binary liquid mixture of 1-butylamine with some Alcohols at two different temperatures.**
  S. Shakeel Ahmad, Mohmmad Yaqub and Abid Karim.
  PK ISSN 002-2941; CODEN JNSMAC. Vol. 46, No.1 & 2 (April & October 2006) PP 21-32.

Acknowledgements

I would like to thanks my organization PCSIR laboratories for sponsoring and supporting my Master leading to PhD studies under its industrial linkage program.

I would like to offer my sincerest thanks to Prof. Dr. Christine Kuntscher, for her continual supervision of my Master and Doctoral project and her direct hands on involvement in the experimental work, which has helped me to accomplish such an extremely challenging project.

I would like to pay my sincerest thanks to Prof. Dr. Alois Loidl (EP–V) for his kindness and reviewing of my thesis. Sincerest and deepest thanks for Dr. Joachim Deisenhofer (EP–V) for his valuable suggestions and precious time which he spent with me to improve my thesis.

I would like to pay my sincerest thanks to Dr. Alexeji Pashkin (University of Konstanz, Germany), for his continual help and valuable suggestions. Many thanks for Dr. Jan Kunes (University of Prague, Czech Republic) for his kind help regarding theoretical aspect of EuB_6 data.

I was lucky enough to have friends and colleagues in my group, and enjoyed the friendly research environment. Indeed, I am going to miss most of them for their kind help: Sindhu John Louis, Ahmed Abouelsayed, Kaneez Rabia, Ali Al–Hadithy, Estaline Amitha Francis, Jihaan Ebad Allah, Armin Hüber and Anis Badawi. I would really be pleased if I could have another chance to work with them.

I would like to thank all technical and administrative staff of the EP–II chair for their kind support and help during my research. A special thank for Mrs. Beate Spörhase for her technical assistance and to Mr. Spörhase (EP – I) for his generous help and suggestions.

Since I lived quite long in Augsburg, Germany, therefore, I made many friends, well wishers and notruf friends. It is hard to write up their names, but I would like thanks to all of them.

There are few great parents in the world, and mine are one of them, and my siblings. I really thank for their continual encouragement and support to keep me, on track on the long way of Master leading to PhD auto bahn.